UNIVERSITY OF SOUTHAMPTON

FACULTY OF PHYSICAL AND APPLIED SCIENCES

Physics

Imaging of Plasmonic Nanoparticles for Biomedical Applications

by

Natasha Fairbairn

Thesis for the degree of Doctor of Philosophy

May 2013

UNIVERSITY OF SOUTHAMPTON

ABSTRACT

FACULTY OF PHYSICAL AND APPLIED SCIENCES
Physics

Doctor of Philosophy

IMAGING OF PLASMONIC NANOPARTICLES FOR BIOMEDICAL APPLICATIONS

by Natasha Fairbairn

Plasmonic nanoparticles show potential for numerous different biomedical applications, including diagnostic applications such as targeted labelling and therapeutic applications such as drug delivery and therapeutic hyperthermia. In order to support the development of these applications, imaging techniques are required for imaging and characterising nanoparticles both in isolation and in the cellular environment.

The work presented in this thesis relates to the use and development of two different optical techniques for imaging and measuring the localised surface plasmon resonance of plasmonic nanoparticles, both for isolated particles and for particles in a cellular environment.

The two techniques that have been used in this project are hyperspectral darkfield microscopy and spatial modulation microscopy.

Hyperspectral darkfield microscopy is a darkfield technique in which a supercontinuum light source and an acousto-optic tuneable filter are used to collect darkfield images which include spectral information. This technique has been used to measure the spectra of single nanoparticles of different shapes and sizes, and nanoparticle clusters. The results of some of these measurements have also been correlated with finite element method simulations and transmission electron microscope images.

The hyperspectral darkfield technique has also been used to image cells that have been incubated with nanoparticles, demonstrating that this technique may also be used to measure the spectra of nanoparticle clusters on a cellular background.

Spatial modulation microscopy is based on fast modulation of the position of a nanoparticle in the focus of an optical beam. This modulation results in a variation in transmitted intensity, which can be detected with very high sensitivity using a lock-in amplifier. Since, for biological imaging applications it is desirable to be able to image, for example whole cells in real time, a fast scanning version of this technique has been implemented, which increases the applicability of the technique to imaging of nanoparticles in cells.

Contents

Declaration of Authorship

I, Natasha Fairbairn , declare that the thesis entitled *Imaging of Plasmonic Nanoparticles for Biomedical Applications* and the work presented in the thesis are both my own, and have been generated by me as the result of my own original research. I confirm that:

- this work was done wholly or mainly while in candidature for a research degree at this University;
- where any part of this thesis has previously been submitted for a degree or any other qualification at this University or any other institution, this has been clearly stated;
- where I have consulted the published work of others, this is always clearly attributed;
- where I have quoted from the work of others, the source is always given. With the exception of such quotations, this thesis is entirely my own work;
- I have acknowledged all main sources of help;
- where the thesis is based on work done by myself jointly with others, I have made clear exactly what was done by others and what I have contributed myself.

Signed:.....

Date:.....

Publications

Parts of this work have been drawn from the following publications:

Fairbairn, N; Light, R A; Fernandes, R; Kanaras, A G; Elliot, T J; Somekh, M G; Pitter, M C; Muskens, O L. *Spatial Modulation Microscopy for Real-Time Imaging of Plasmonic Nanoparticles and Cells* Opt. Lett. **2012** *37, 15* p3015-3017.

Fairbairn, N; Christofidou, A; Kanaras, A G; Newman, T A; Muskens, O L. *Hyperspectral Darkfield Microscopy of Single Hollow Gold Nanoparticles for Biomedical Applications* Phys. Chem. Chem. Phys. **2013** *15* p4163-4168.

Fairbairn, N; Fernandes, R; Carter, R; Elliott, T J; Kanaras, A G; Muskens, O L. *Single-nanoparticle detection and spectroscopy in cells using a hyperspectral darkfield imaging technique* Proc. SPIE 8595 **2013** 859501.

Acknowledgements

I would like to thank the following people for their contributions to this work; Otto Muskens, Martina Abb, Agathi Christofidou, Roger Light, Oded Rabin, Anton Page and the rest of the team at the biomedical imaging unit at Southampton General Hospital, Zondy Webber, Gareth Savage, Paul Kinsey and the rest of the electronics and mechanical workshop technicians, Rute Fernandes, Tom Strudley, Hannah Warren, Marcel Fowler, Tom Haskins, Rachel Carter, Antonios Kanaras, Tim Elliot, Tracey Newman, Mike Somekh, Mark Pitter and Hugh Hopper. All nanoantenna samples imaged in this project have been fabricated by Martina Abb and colloidal nanoparticles have been fabricated by Rute Fernandes and Agathi Christofidou.

Glossary of Biological Terms

Cell Culture	Cells grown under controlled conditions outside of their natural environment.
Cell line	A cell culture developed from a single cell and therefore consisting of cells with a uniform genetic makeup.
DC 2.4	A dendritic cell line.
Dendritic cell	A type of white blood cell that forms part of the immune response in mammals.
Endocytosis	A process by which a cell may uptake material.
Endosome	A bubble that forms around material uptaken by a cell by endocytosis.
Enzyme	A biological catalyst.
Fibroblast	A connective tissue cell responsible for synthesising collagen and the extracellular matrix.
L929	A fibroblast cell line.
Moviol	A cell mounting medium.
Neuroblast	A type of brain cell. A precursor of neurons in embryonic development.
Paraformaldehyde	A chemical used to preserve biological samples.
PBS	Phosphate buffered saline, a buffer solution which maintains a constant pH.
Peptide	A short chain of amino acids.
SHSY-5Y	A neuroblast cell line.

Chapter 1

Introduction

1.1 Overview

Metal nanoparticles, and in particular gold nanoparticles, have held much interest in recent years for exploitation in a range of biological applications [1; 2; 3]. For example nanoparticles are being found to be useful in diagnosis applications involving imaging and sensing techniques [4; 5], and in therapeutic applications such as therapeutic hyperthermia for treating cancer [6]. From a chemistry perspective, gold nanoparticles are of particular interest in due to their chemical stability, biocompatibility, and the large amount of chemical functionalisations available. Gold nanoparticles can be functionalised with biological molecules via thiols, which allows for drug delivery applications and targeted labelling [7; 8]. Gold is an unreactive metal so toxicity of gold nanoparticles is expected to be low, particularly in comparison to, for example quantum dots [9]. However, the toxicity of gold nanoparticles is not yet fully known, and more research needs to be done in this area to assess the possible risks associated with using gold nanoparticles in the human body [10; 11]. Another reason that metal nanoparticles have so much potential for these applications is due to the interesting optical properties which they exhibit.

Metal nanoparticles absorb and/or scatter light strongly at a particular wavelength due to a resonance known as the localized surface plasmon resonance or LSPR. The wavelength at which the LSPR occurs depends on the size and shape of the nanoparticle as well as on its dielectric properties and on the surrounding environment. Controlling the morphology of the nanoparticle therefore allows control over the LSPR wavelength. This tuneability means that nanoparticles can be created to have a resonance within the 'biological near-IR window'; the part of the spectrum where light is not absorbed by biological tissue.

The focus of this project is on biomedical imaging involving plasmonic nanoparticles, and in particular gold nanoparticles. Current common methods used for imaging of

colliodal gold nanoparticles in cells are fluorescence imaging and transmission electron microscopy. However, each of these methods has its disadvantages. The disadvantage of fluorescence based microscopy techniques is that the typical dye-molecules used as labels undergo photobleaching. On the other hand, transmission electron microscopy (TEM) requires lengthy sample preparation since the samples must be in the form of thin slices. For this reason, TEM is difficult to perform on live cell samples [12]. In section 1.4 several other alternative techniques for imaging plasmonic nanoparticles will be discussed.

Two alternative optical microscopy methods, which use the LSPR signal and are capable of detecting single gold nanoparticles, have been used in this project. These imaging methods have been further developed for use in biological applications over the course of the project.

The reason for the interest in developing systems for nanoparticle imaging and characterisation, and in particular for imaging the interactions of nanoparticles with biological cells is explained in more detail in the following section.

1.2 Applications of Nanoparticles

Nanoparticles have wide ranging applications in a variety of areas, due to their physical properties. One example of an application that exploits the optical properties of nanoparticles includes sunscreen, in which titanium dioxide or zinc oxide nanoparticles are used in order to protect the skin from harmful UV rays, whilst being transparent to visible wavelengths [14]. An example of a potential application of plasmonic nanoparticles is in solar cells in which scattering of light from nanoparticles could increase the effective path length of the light in thin film solar cells, thereby increasing absorption of light in these solar cells [15; 16].

Nanoparticles also have useful catalytic properties due to their high surface area to volume ratio and therefore an important chemical application of metal nanoparticles is as catalysts [17].

Below several of the emerging applications of nanoparticles in healthcare and diagnostics will be discussed.

1.2.1 Biomedical Applications of Nanoparticles

The work in this project has been undertaken with an emphasis on biomedical applications of nanoparticles and in particular the focus has been on developing imaging techniques which could be used to understand more about the interactions between nanoparticles and cells. The reason for choosing to focus on imaging of nanoparticles

for biomedical applications is due to the numerous biomedical applications in which nanoparticles are already used. The development of such applications may be aided by improvements in the imaging systems used to study them. Some examples of the potential applications of nanoparticles in biology and medicine will be briefly explained below in order to put the work undertaken here into a broader context.

Whilst nanoparticles used in biological applications include polymer nanoparticles [18], quantum dots [19], magnetic particles [20; 21] and metallic nanoparticles, metallic nanoparticles, and in particular gold nanoparticles are of particular interest for this project so applications for which gold nanoparticles are particularly suited are set out below.

Drug Delivery

A potential area in which nanoparticles may be of interest is in targeted drug delivery applications. It is desirable to achieve targeted drug delivery in many instances as this can enable a lower total dose of a drug to be administered as the drug can be sent directly to the targeted area of the body, rather than being spread throughout the body. An example of the requirement for targeted drug delivery can be seen in cancer therapy [22], where currently, a patient undergoing chemotherapy needs to be given a high dose of chemotherapy drugs which have strong negative side effects and are often carcinogenic themselves. If a more targeted drug delivery system is used it would be possible to send the chemotherapy drugs directly to the cancer site, rather than dosing the whole body, which should result in a decrease in side effects experienced by patients.

Drugs can be carried by nanoparticles either by attaching them to the surface of the nanoparticle (known as functionalisation) or by encapsulating the drugs inside a hollow nanoparticle [23]. In addition, other biological molecules can be attached to the surface of the nanoparticle which are designed to attach to specific receptors within the body for targeting. This functionalisation also enables the use of nanoparticles as targeted labelling agents. In one study [24], for example, anti-epidermal growth factor receptor (anti-EGFR) monoclonal antibodies were attached to the surface of gold nanorods. Malignant epithelial cells have many more epidermal growth factor receptors on their surface than non malignant epithilial cells. Therefore when malignant and non malignant varieties of these cells were incubated with the functionalised nanorods, the nanorods had a much higher affinity to bind to the malignant cells. The type of molecules used to coat the nanoparticles can also allow control over whether the nanoparticle attaches to receptors on the outside of a cell membrane or is taken up by the cell.

Another property of nanoparticles which is useful for drug delivery is their potential to cross the blood-brain barrier. The capiliaries in the brain have particularly tight junctions, in order to separate the blood and the brain extracellular fluid, that do not exist in other parts of the circulatory system. Therefore, delivering drugs to the brain is especially challenging. Nanoparticles have the potential to carry out multiple specific functions in a pre-determined sequence, which may be useful for crossing the blood brain

barrier. For example, funtionalised nanoparticles can be designed to be taken up by cells which are able to cross the blood brain barrier, releasing the drugs they are carrying when they reach the required area of the brain [25; 26].

Therapeutic Hyperthermia

Metal nanoparticles may also be used for therapeutic hyperthermia, also known as photothermal therapy [27]. The process behind photothermal therapy can be explained as follows. Metal nanoparticles are first attached to, or uptaken by the cells of interest, through previously discussed methods. The cells are then illuminated with laser light at the LSPR wavelength of the nanoparticles. The nanoparticles absorb light at the LSPR, which is converted to heat in the cell. This heating effect can be used to selectively destroy cells that have nanoparticle inside them or attached to them. Photothermal therapy is useful as a cancer therapy as it has been found that a lower laser power is required to kill cancer cells than normal cells, since cancer cells are more sensitive to changes in temperature [24]. Therefore, the laser power used can be chosen such that cancer cells exposed to that laser power will die whilst any normal cells that are also exposed will be able to recover.

Surface Enhanced Raman Spectroscopy Sensing

Another application of gold nanoparticles, which is often used for biological measurements, is surface enhanced Raman spectroscopy or SERS. Raman scattering is the process of inelastic scattering of light from a vibrational mode of a molecule. It has been found that the Raman scattered intensity is enhanced when the molecule of interest is situated in an area of intense electric field (known as hot spots) produced by plasmonic structures which are used as SERS substrates [28] [29].

The main application for SERS in biology is for detecting the presence of particular molecules using their vibrational spectrum as a molecular 'fingerprint'. This technique is useful for detecting molecules which may be indicators of a disease or condition, but may be present in low concentrations in a sample [30].

Diagnostic Tests

A further biomedical application in which plasmonic nanoparticles are used is the area of diagnostic testing. An example of this application is the plasmonic enzyme-linked immunoabsorbant assay (plasmonic ELISA). ELISA is a test for detecting biomarkers which works as follows. First the biomarker in question is deposited on a surface, which it adheres to due to charge interactions. Secondly, an unreactive protein is added to block any areas of the surface not covered by the biomarker. Thirdly, an antibody is added which has been specifically tailored to bind to the biomarker, but not to the unreactive proteins bound to the surface. Fourthly, a second antibody is added, which binds to the first antibody at one end and has an enzyme attached at the other end. Finally, a compound (the enzyme substrate) is added that will react with the enzyme

resulting in a colour change. The surface is washed in between each step to ensure that any molecules that are not chemically bound are washed away. Therefore the colour change gives an indication of the amount of the second antibody that has bound to the first antibody, that has bound to the respective antigen on the biomarker on the surface. That is, the test gives an indirect indication of the concentration of the biomarker on the substrate. [31]

Plasmonic ELISA uses the optical properties of plasmonic nanoparticles to increase the sensitivity of this test. In the plasmonic version, the reaction between the enzyme and the enzyme substrate takes place in a solution that includes precursor materials for forming gold nanoparticles and plays a role in the growth mechanism of gold nanoparticles in the solution, which decreases the availability of gold ions in the solution causing slow, uneven growth and producing aggregated particles. When the enzyme and the enzyme substrate are not present, the particles grow quickly and thus are spherical and separated. The optical properties of the aggregated particles cause the solution to look blue, indicating that the biomarker of interest is present, and the spherical particles cause the solution to look red, indicating a negative result. The colour of the solution (either blue or red) is easily seen by the naked eye. Plasmonic ELISA has been used to test for HIV and prostate cancer [32].

The Near-IR Window

For many biological applications that exploit the LSPR effect, there is a preference for using nanoparticles which have a resonance between 600 and 1400 nm wavelength. This preference is due to the fact that in this part of the visible - infrared spectrum, less light is absorbed by human tissue than at other wavelengths. Further into the infrared (above 1400 nm) there is strong absorption by water which is present in human tissue. At the visible/UV end of the spectrum, light is absorbed by the skin pigment melanin and by haemoglobin, which is responsible for the red colour of blood as it absorbs in the green/blue part of the spectrum. Using modern colloidal synthesis methods, it is possible to tune the sizes and shapes of nanoparticles such that their LSPR's fall in this window [33].

1.3 Theoretical Background

Many of the applications of metal nanoparticles in imaging, sensing and therapy described above rely on the localised surface plasmon resonance (LSPR) effect. This effect results in an enhancement of the absorption and scattering of light at a particular wavelength, depending on the dielectric properties of the nanoparticle and its surrounding environment. A brief introduction to the theory of localised surface plasmon resonance is presented below.

The 'sea' of electrons in a metal can be thought of as a plasma or free electron gas. When an external electric field is incident on a metal, it exerts a force on the free electrons and they are displaced from their usual positions in the metal lattice.

The Drude model can be used to describe the behaviour of the free electrons. The Drude model assumes that the free electrons do not interact with ions in the lattice over long ranges. The reason these long range interactions can be ignored is because the free electrons screen the charge of the ions over long ranges. The The only interactions taken into account in this model are collisions of the free electrons, which can be with ions in the lattice or with other free electrons. These collisions have the effect of damping the movement of the electrons. The equation of motion describing the motion of the a free electron in a metal under an externally applied field E is given by

$$m_e\ddot{x} + m_e\gamma\dot{x} = -q_eE, \tag{1.1}$$

where m_e is the mass of the free electron, x is the displacement of the electron, q_e is the charge of an electron and E is an external electric field. The relaxation time τ of the electron, given by equation 1.2 depends on the damping factor γ which is due to collisions of the free electron with the metal lattice

$$\tau = \frac{1}{\gamma}. \tag{1.2}$$

Equation 1.1 describes a free electron in the metal. In order to describe a bound electron, an extra linear term must be added to the left side of equation 1.1 with the form $m{\omega_0}^2x$ this extra term is required in order to describe interband transitions - that is the process of an electron falling from the conduction band to the valence band and emitting light. However, for the purpose of describing plasmons it is sufficient to take into account just the free electrons.

For an oscillating electric field $E = E_0e^{-i\omega t}$ a solution of the equation of motion 1.1 is $x = x_0e^{-i\omega t}$ with the amplitude x_0 given by

$$x_0 = \frac{q_e}{m_e(\omega^2 + i\gamma\omega)}E_0. \tag{1.3}$$

The above model describes the response of a single electron in a metal which is displaced by an external electric field. The displacement of multiple electrons in a metal gives rise to a macroscopic polarisation $P = -nq_ex$ where n is the number density of electrons, q_e is the charge of an electron and x is the displacement of the electrons. In this case, P is therefore given by

$$P = -\frac{nq_e^2}{m_e(\omega^2 + i\gamma\omega)}E. \tag{1.4}$$

In order to find the dielectric function of the free electron gas, it is useful to write equation 1.4 in terms of the electric displacement D (which describes how the charges in a material react to an externally applied field) since $D = \epsilon_0 E + P$ and $D = \epsilon_0 \epsilon_w E$ where ϵ_0 is the permittivity of free space and ϵ_w is the dielectric function of the material

$$D = \epsilon_0(1 - \frac{nq_e^2}{\epsilon_0 m_e(\omega^2 + i\gamma\omega)})E. \tag{1.5}$$

Here, one can define the plasma frequency of the free electron gas as

$$\omega_p^2 = \frac{nq_e^2}{\epsilon_0 m_e}. \tag{1.6}$$

Combining equations 1.5 and 1.6 gives the dielectric function of the free electron gas, which is therefore

$$\epsilon_\omega = 1 - \frac{\omega_p^2}{\omega^2 + i\gamma\omega}. \tag{1.7}$$

The equations above describe the plasmonic behaviour of the free electrons in a bulk metal using the Drude model [34]. In this model, when $\omega \simeq \omega_p$ light is reflected from the metal surface, since the electrons follow the electric field. When $\omega \ll \omega_p$ absorption by the metal increases. When $\omega > \omega_p$ then the Drude model no longer gives a good description of the behavior of metals as interband transitions become important.

At the surface of a metal, the electron oscillation can couple to an incident photon which is known as a surface plasmon polariton (SPP). The SPP behaves differently to the bulk free electron gas case in that the plasmons propagate along the surface of the metal and decay rapidly below the surface, since the electric field decays evanescently as it penetrates below the surface of the metal.

Metal nanoparticles that are much smaller than the wavelength of light do not experience a spatially varying electric field over their volume, so much as a time-varying electric field which is constant over the whole particle. They also have a high surface area to volume ratio. These two differences, in comparison to the case of a bulk metal of infinite size with no surface, give rise to a localized surface plasmon resonance or LSPR, which has the effect of polarising the nanoparticle. Differently shaped nanoparticles can support different plasmon modes. For example, gold nanorods can support two plasmon modes, since they can be polarised in two different directions (along the long and short axis of the rod) (see figure 1.1).

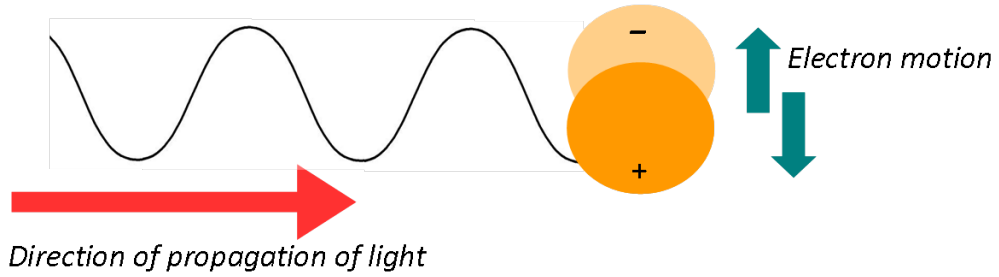

Figure 1.1: Localized surface plasmon resonance

For spherical metallic nanoparticles which are very small compared to the wavelength of light (about 10 nm diameter or less for visible light), the polarisability of the nanoparticle, α, is given by

$$\alpha = 4\pi a^3 \frac{\epsilon(\omega) - \epsilon_d}{\epsilon(\omega) + 2\epsilon_d}, \tag{1.8}$$

where a is the radius of the nanoparticle, $\epsilon(\omega)$ is the dielectric function of the metal and ϵ_d is the dielectric function of the material surrounding the nanoparticle [35]. It can be seen from equation 1.8 that the polarisability of the nanoparticle reaches a maximum when $|\epsilon(\omega) + 2\epsilon_d|$ is minimised. When the condition that $Re[\epsilon(\omega)] = -2\epsilon_d$ (known as the Fröhlich condition) is met, a localised surface plasmon resonance (LSPR) occurs. The maximum value of the polarisability is limited by the fact that $Im[\epsilon]$ is always non zero so $|\epsilon(\omega) + 2\epsilon_d|$ never approches zero.

The LSPR effect enhances the optical cross section of the particles, which enables detection of much smaller particles than would be possible if the particles were, for example dielectric scatterers, which enables the use of optical microscopy methods including darkfield and spatial modulation microscopy for detection of nanoparticles in biomedical imaging systems. These optical imaging systems rely on the strong scattering and absorption properties of nanoparticles. The scattering and absorption cross sections (C_s and C_a) for nanoparticles are given by

$$C_s = \frac{k^4}{6\pi} |\alpha|^2 \tag{1.9}$$

$$C_a = kIm[\alpha], \tag{1.10}$$

where k is the wavevector of the light incident on the nanoparticle and α is the polarisability of the nanoparticle [36]. For spheres it can be seen that absorption scales with a^3 and scattering scales with a^6. These equations show that absorption dominates for very small particles but scattering increases rapidly as particles increase in size. Spatial modulation microscopy detects the signal due to extinction (scattering plus absorption). Darkfield microscopy, by definition, only detects scattered light. Therefore, it becomes

more and more difficult to detect smaller and smaller particles using darkfield. Because of this limitation, in this project darkfield has been mainly used to image small particles in clusters and single particles larger than 50 nm diameter.

Larger nanoparticles do not see a spatially constant electric field over their volume so retardation effects become important. However, the quasi-static approach described above serves as a reasonable approximation for spherical nanoparticles with diameters up to approximately 100 nm. For larger particles, Mie theory gives a more accurate electrodynamic method for describing the LSPR. [37]

1.3.1 Introduction to Finite Element Method for Modelling Spectra of Gold Nanoparticles

In order to theoretically predict the localised surface plasmon resonance spectra of gold nanoparticles, in this project the finite element method was used. The finite element method (FEM) is a numerical technique which can be used to find approximate solutions to a set of partial differential equations that describe a particular system. For modelling the interactions between light and metallic nanoparticles, the equations used to describe the system are Maxwell's equations:

$$\nabla \cdot \vec{E} = \frac{\rho}{\epsilon_0} \tag{1.11}$$

$$\nabla \cdot \vec{B} = 0 \tag{1.12}$$

$$\nabla \times \vec{E} = -\frac{\partial \vec{B}}{\partial t} \tag{1.13}$$

$$\nabla \times \vec{B} = \mu_0 \epsilon_0 \frac{\partial \vec{E}}{\partial t} + \mu_0 \vec{J}; \tag{1.14}$$

where $\vec{E}$ is the electric field intensity, $\vec{B}$ is the magnetic field intensity ϵ_0 is the permittivity of free space μ_0 is the permeability of free space ρ is the total charge density and $\vec{J}$ is the total current density.

In FEM the problem of solving these equations is simplified by discretising the space which is being investigated into elements and then solving the equations for each discrete element. In this project, COMSOL Multiphysics (4.2) software was used to perform the FEM calculations. Hollow gold particles were modelled as explained in the next section.

1.3.2 Methodology

Firstly, three concentric spherical shells were built. The innermost spherical shell represented the gold nanoparticle. The outermost shell consisted of perfectly matched layers

(PML's) which are designed to absorb light reaching the edges of the model, so that light does not reflect off the edges. A third sphere was also placed in between the outer and inner spheres. This third sphere provided a surface over which parameters could be integrated in order to produce the theoretical spectra. Calculations were performed using both water and air as the material surrounding the gold nanoparticle, since in this project the nanoparticles have been used in solution or dried out in air. Comsol has built in data for the material properties of air and water which were utilised in the models shown in this project.

In order to include the plasmonic properties of the gold, the dielectric function of gold must be taken into account. This was achieved by using the data measured by Johnson and Christy [38], interpolating between the discrete values presented in the paper using a built in Comsol interpolation function, in order to produce a complete dielectric function for a range of frequencies as shown in figure 1.2.

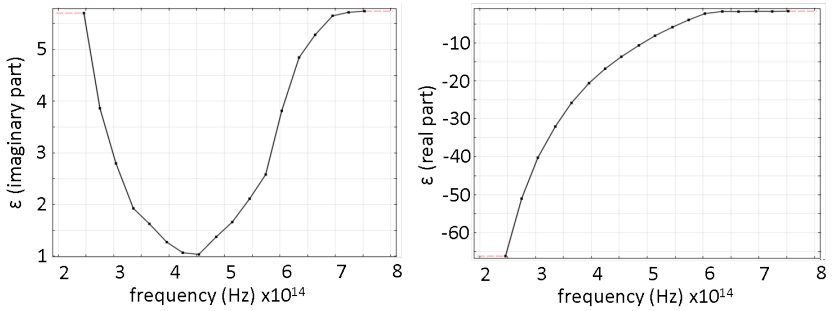

Figure 1.2: Plots of the real and imaginary parts of the dielectric function of gold using data measured by Johnson and Christy [38] with a linear interpolation between data points performed using Comsol

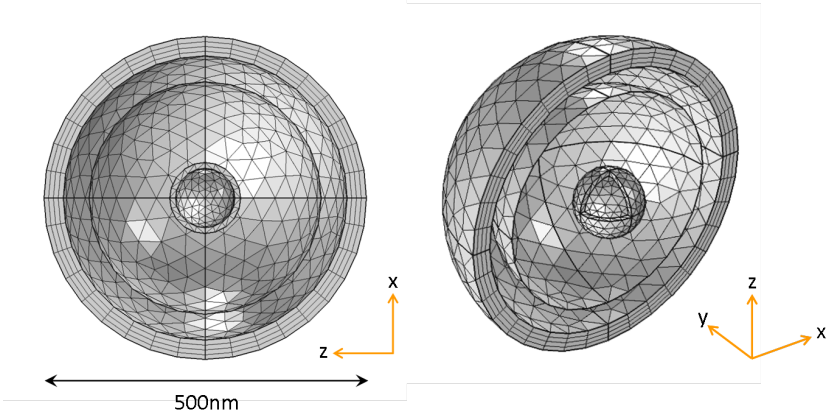

Figure 1.3: Figure showing the geometry of the model and the mesh used. The PML's are represented by the outermost shell which has a radius of 250 nm and a thickness of 30 nm. The second sphere is the integration sphere with a radius of 180 nm. The radius of the integration sphere was chosen to be small enough to minimise calculation time whilst being large enough to evaluate scattering in the far field. The innermost shell represents the hollow gold particle which has a radius of 55 nm and thickness of 9 nm.

In order to perform the FEM calculation, the geometry is divided up into discrete elements, that is a mesh is built as shown in figure 1.3. A free tetrahedral mesh was used for the most parts of each model with a free triangular mesh coating the inside surface of the PML's with a swept mesh to the outer surface of the PML's. The reason for choosing a swept mesh for the PML's was so that the light would have to pass through several absorbing layers, increasing the absorption efficiency of the PML's. In order to check that the mesh was fine enough for the model the basic calculation for a hollow gold particle in air was performed with the standard mesh size (element size 'normal' in Comsol 4.2) and with an extremely fine mesh and the results were found to be in agreement, demonstrating that the standard mesh size chosen for the calculations shown in this thesis was adequate.

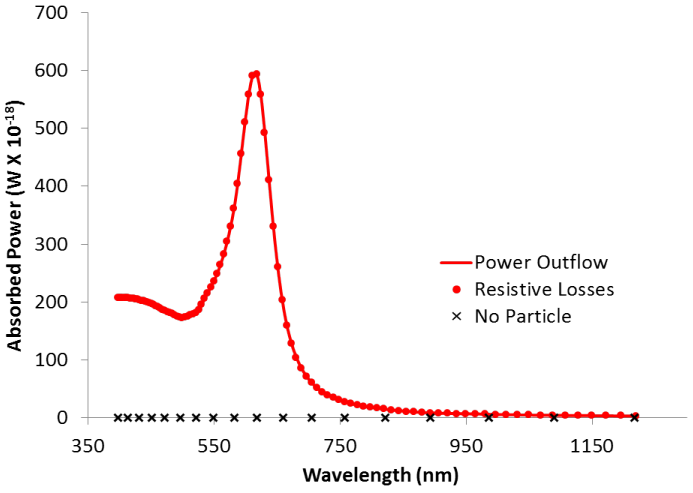

Figure 1.4: Total power absorbed by a hollow gold nanoparticle in air calculated using resistive losses and negative power outflow. The power absorbed when no nanoparticle is present is shown to be negligable.

The nanoparticle was excited with an electromagnetic plane wave travelling in the z direction and polarised in the y direction and the model was solved for the scattered field. The absorption cross section can be calculated by computing the resistive losses due to absorption in the nanoparticle [39]. The resistive losses can be calculated directly in Comsol.

Another equivalent way to calculate absorption is by integrating the normalised power outflow through a sphere surrounding the nanoparticle. The total power outflow through the integration sphere should be zero when no nanoparticle is present since the plane wave is flowing in and out of the sphere giving a net power outflow of zero. However, when the nanoparticle is present, some of the incident light is absorbed, giving a negative power outflow. Therefore the absorbed power is given by negative power outflow which is equivalent to the absorbed power calculated from the resistive losses as shown in figure 1.4. In order to calculate the negative power outflow with no nanoparticle present, the

material properties of the nanoparticle were adjusted to be identical to the surrounding material.

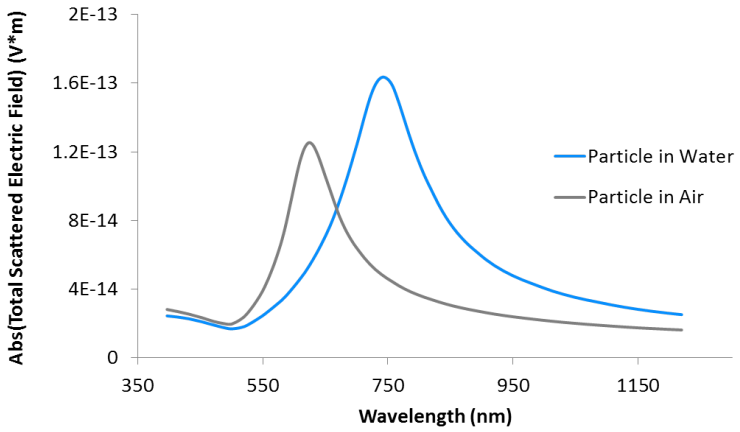

Figure 1.5: Absolute values of scattered electric field integrated over a spherical surface with a radius of 180 nm, for a hollow gold nanoparticle in air and water.

Since the hyperspectral darkfield method measures scattered light, in order to compare modelled spectra to the measured spectra it is better to model the scattering spectra of the particles rather than absorption. In order to calculate scattering spectra the same integration sphere was used as for calculating absorption but to calculate scattering, the value integrated over was the scattered electric field (known in Comsol 4.2a as the relative electric field). This integration gives real and imaginary parts of the scattered electric field so the absolute value $\sqrt{(Re^2) + (Im^2)}$ was used to produce the scattering spectra. The scattering spectra produced by this method are shown in units of Vm since the electric field is in units of V/m and the surface area of the integral sphere is in units of m^2. It is acceptable to use these arbitrary units since the hyperspectral darkfield system does not quantitatively measure the scattering cross section and therefore it is the position of the peak that is of interest rather than the height of the peak.

It can be seen from figure 1.5 that a change in the refractive index of the material surrounding the hollow gold particle causes a significant shift in the LSPR peak. If the resonance is measured in air or in solution, the LSPR will be found to be different, with a redshift of the LSPR peak occuring as the refractive index of the surrounding material is increased. The nanoparticle is in reality functionalised with molecules and this has not been taken into account in these simulations. The measurements of the scattering spectra performed in conjunction with TEM measurements were performed on a carbon coated, formvar grid, in air. In the models that have been built as direct comparisons with the spectra measured using the hyperspectral darkfield method, an average refractive index (1.2) of air (1.0) and formvar (1.4) has been used as an approximation of the refractive index of the surrounding material.

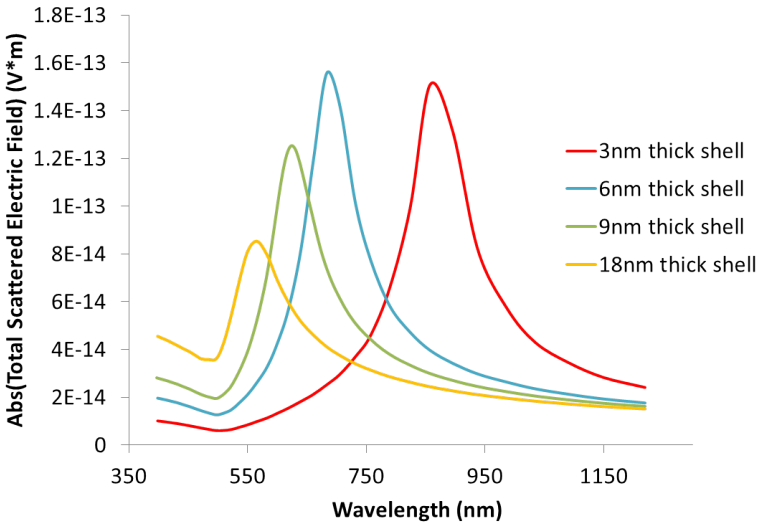

Figure 1.6: Scattering spectra of hollow gold nanoparticles with different shell thicknesses in air.

The thickness of the gold shell of the hollow gold particles can also have an effect on the spectrum with thicker shells causing a blue shift of the LSPR peak [40].Figure 1.6 shows models of hollow gold particles of the same size but with different shell thicknesses. A shift in the LSPR wavelength from 900 nm to 550 nm can be seen when the shell thickness is changed from 3 nm to 18 nm. A redshift in the LSPR peak is seen as the shell thickness is decreased.

1.4 Nanoparticle Imaging Systems - Current State of the Art

Nanoparticles, in general are of a size that falls below the diffraction limit of visible light, so detecting individual nanoparticles with light poses a challenge, as detection of nanoparticles with traditional brightfield microscopy is not possible.

However, there are many different methods for imaging nanoparticles which are able to overcome this problem [41]. In general, these techniques can be divided into near-field techniques, where the electric field is measured in the immediate vicinity of the nanoparticle, enabling measurement of the evanescent optical fields, and far-field techniques, which do not require measurements so close to the sample.

1.4.1 Near-field Imaging

An example of a near-field technique is a scanning near-field optical microscope (SNOM) which measures the evanescent optical fields from the sample by placing an aperture with

dimensions much smaller than the wavelength of light, nanometers from the surface of the sample [42]. Evanescent fields of metal nanoparticles are a result of the large scattering and absorption cross-sections that occur due to the LSPR. However, the disadvantage of using a near-field technique such as a SNOM is the extremely small working distance required and the extremely shallow depth of field available. Essentially, SNOM is therefore limited to studying surfaces. Long scan times can also be an issue when imaging large sample areas or producing high resolution images.

1.4.2 Imaging Techniques Based on Scattering and Absorption

Many far-field techniques for detection or imaging of metal nanoparticles make use of the fact that metal nanoparticles absorb and scatter light at the LSPR [43]. An advantage of using far-field techniques for biomedical imaging applications is that there is no direct interaction with the sample which may be important for imaging of biological samples.

One such technique that detects the light scattered by the nanoparticle is darkfield microscopy [44], which is one of the main techniques used for imaging nanoparticles in this project.

Other scattering based techniques for detecting single nanoparticles include the interferometric scattering (iScat) technique [45; 46] and differential interference contrast (DIC) microscopy [47].

Spatial modulation microscopy is a technique which can be used to image nanoparticles using a signal due to scattered or absorbed light.

Darkfield Microscopy

The principle of a darkfield microscope is that only light which has been scattered by the sample is sent to the detector and light which has not been scattered is not detected, as shown in figure 1.7.

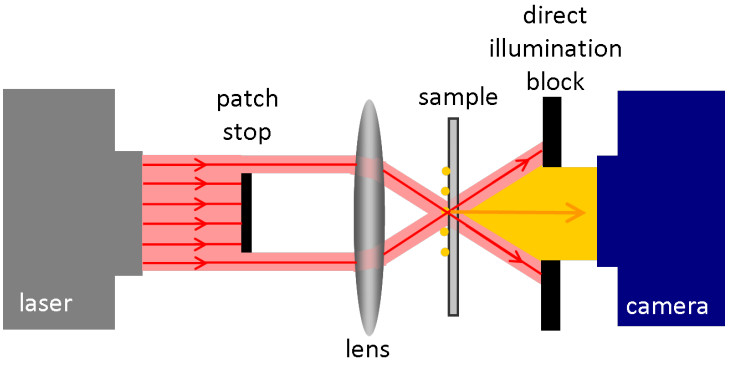

Figure 1.7: Diagram indicating the light path through a typical darkfield microscope.

The resulting image contains bright areas where the sample is strongly scattering and dark areas for areas on the sample where no scatterers are present. An advantage of darkfield microscopy is that it allows widefield imaging, meaning that an image can be collected simultaneously over a large area, as opposed to techniques that require scanning over many single point measurements, which can be time consuming. The time taken to record an image is particularly important for live cell imaging applications where real time imaging is required [48].

The main disadvantage of darkfield microscopy is that it detects only light which has been scattered from nanoparticles, which scales with the 6th power of the nanoparticle radius. Therefore the darkfield signal rapidly decreases with decreasing particle size, so it is difficult to see small nanoparticles in a darkfield microscope. In addition, because darkfield microscopy detects scattered light, it can be difficult to detect nanoparticles on a substrate that has impurities or small structures which may also scatter light [41].

Darkfield microscopy can be set up in transmission (as shown in figure 1.7) or in reflection. In a reflection darkfield microscope, the light reflected from the sample is blocked by the direct illumination block in the same way that light directly transmitted through the sample is blocked in the set up shown in figure 1.7.

Interference based detection

In some nanoparticle imaging systems light scattered from the sample may be mixed with another source of light to provide an amplification of the scattered light, for example light scattered from a sample may be mixed with light reflected from the sample.

In this situation, the total intensity of light collected by the detector therefore consists of light which has been reflected from the sample (I_{ref}), light which has been scattered from the sample (I_s) and a component which is the interference between the two (I_{int}). In I_{int} the scattered light from the nanoparticle is effectively amplified by the light reflected by the sample, since $I_{int} \propto E_{ref} E_s$ while $I_s \propto |E_s|^2$ which is a smaller term for weak E_s.

This effect of amplification of the scattering signal by mixing with another beam is a form of heterodyne detection [49] and the scattered light may be amplified by either mixing with light reflected from the sample, (such as in the iScat system [45; 46]) or by mixing with a reference beam (such as in a Mach-Zehnder interferometer [50]) .

Differential Interference Contrast Microscopy

Another technique which detects light scattered by the nanoparticle is differential interference contrast microscopy. This technique works by illuminating a sample with two different light paths which are orthogonally polarised as well as being slightly spatially offset from each other. After the sample, therefore, two brightfield images are present

which are polarised orthogonally and slightly offset from each other. The two different polarisations are then combined using a Nomarski / Wollaston prism.

The Nomarski/ Wollaston prism changes the two images from being orthogonally polarised to having the same polarisation. Once the two images have the same polarisation, they interfere with each other to produce the DIC image. The DIC image shows contrast between adjacent areas on the sample that have produced phase changes in the light as the light passing through those points has travelled along different path lengths. A higher level of contrast is seen when the difference in path lengths between two adjacent spots is more pronounced due to, for example, thickness or refractive index changes in the sample.

When DIC is used to image a nanoparticle, the spatial offset between the orthogonally polarised light paths means that one of the light beams interacts with the nanoparticle, while the other one acts as a reference beam. When the two polarisations are recombined, the reference beam therefore interferes with the forward scattered light from the nanoparticle. The amplitude and phase of the scattered light can be recovered from the measured signal, giving information about the optical properties of the nanoparticle [51]. DIC can also be used for detecting nanoparticles in cells as well as measuring individual nanoparticles, for example DIC has been used to detect gold nanoparticles inside HeLa cells [52].

Spatial Modulation Microscopy

Spatial modulation microscopy is another technique which has been used for measuring the optical properties of single nanoparticles [53; 54]. The principle behind this technique is that a nanoparticle is positioned in the focus of a laser beam and then the position of the nanoparticle is modulated relative to the laser beam. A modulating signal is therefore produced due to absorption and scattering of the laser light by the nanoparticle which can be recovered using lock-in techniques. The advantages of this technique are that it is quantitative, it is a far-field technique and it can detect either scattered or absorbed light, which means that it can be used to detect nanoparticles of a wide variety of sizes. In this respect, spatial modulation microscopy has an advantage over techniques such as darkfield, which are based on detecting scattered light, making it difficult to detect small nanoparticles for which absorption is the dominant LSPR mechanism. The disadvantage of spatial modulation microscopy is that it is inherently a point scanning technique, therefore it can be time consuming to image a large area of a sample. The theoretical principles behind the spatial modulation microscopy technique will be explained in detail in chapter 4.

1.4.3 Photothermal Techniques

After a nanoparticle has absorbed light due to the LSPR, almost all of the absorbed energy is converted into heat, causing a local change in refractive index. This effect is known as the photothermal effect. Some nanoparticle imaging techniques make use of signals produced due to this heating effect, such as the techniques described below. The main disadvantage for photothermal based techniques for biological imaging applications is that heating of the sample is required, which could cause unwanted effects or damage when imaging biological samples.

Photothermal DIC

The photothermal effect can be detected optically using a differential interference contrast (DIC) technique as the area directly surrounding the nanoparticle will heat up, but the area around the reference beam will not heat up, causing a phase difference between the two orthogonally polarised beams used in the DIC system. To improve noise rejection, the beam which is partially absorbed by the nanoparticle is modulated, causing a modulation in the phase difference between the two probing beams and therefore a modulation in the intensity of the detected light, which is the interference between these two probe beams [56].

Photothermal Heterodyne Imaging

Another technique which uses the photothermal effect to detect nanoparticles is photothermal heterodyne imaging (PHI). In this technique, instead of using a DIC based detection system, a single probe beam is used in addition to the heating beam. The heating beam is modulated in intensity causing a time modulated refractive index around the nanoparticle. An off-resonance probe beam is incident on the nanoparticle which produces a frequency shifted scattered field as it interacts with the varying refractive index, which is produced in the presence of a nanoparticle. The frequency shifted scattered field is interfered with the original probe beam. Since these two beams now have slightly different frequencies a beat frequency is produced when they are combined which is at the frequency of the modulation. Lock-in detection can then be used to recover the signal at the beat frequency [57].

Photothermal Optical Coherence Tomography

The photothermal effect is also used in photothermal optical coherence tomography (PT-OCT). Optical coherence tomography is an interferometric technique where a sample of interest is illuminated with a laser and photons that have been backscattered off subsurface features in the sample are collected, because it is an interferometric technique, the path length of the received photons can be calculated and any photons that have been scattered multiple times within the sample can be rejected [58]. This enables the low signal produced by single scattering events to be recovered. OCT has a higher resolution than other medical imaging systems such as ultrasound or MRI but as the photons cannot penetrate very far through biological tissue it can only be used for imaging up to a depth of 2mm. In PT-OCT a laser with a wavelength at the LSPR of nanoparticles used in the sample is modulated to give a modulating PT signal which gives rise to changes in optical path length. These changes are then detected using an OCT microscopy system [59]. PT-OCT has been used for imaging applications including imaging of gold nanorod uptake in lymph nodes [60], detection of macrophages in ex vivo rabbit arteries using nanoparticles comprised of an iron oxide core coated with gold [61] and for detection of gold nanoshells in human breast tissue [62].

Photoacoustic Imaging

Another method that can be used for imaging nanoparticles in cells is photoacoustic imaging [63] The principle behind this method is that laser induced heating of a sample causes expansion of the media that is being heated by the laser beam, and compression in the surrounding media. This effect produces an acoustic signal which is picked up by an ultrasonic transducer. Where plasmonic nanoparticles are present in the sample, an increased photoacoustic signal is seen when the nanoparticles are illuminated at their LSPR wavelength as they absorb light at this wavelength and heat up, which increases the photoacoustic signal. This technique has been used for in vivo imaging of mice with tumors, after injection of PEG coated gold nanorods [64]. Using different illumination wavelengths enables differentiation between the signal due to nanorods and that due to other absorbers in the tissue (mainly haemoglobin and oxyhaemoglobin).

1.4.4 Non-linear Techniques

The methods described above are examples of techniques where the signal is produced by the absorption or scattering of light due to the LSPR. Some nanoparticle characterisation techniques are based on non-linear processes induced by the nanoparticles. These techniques include two-photon excitation, third harmonic generation microscopy and the four-wave mixing technique.

Two-Photon Luminescence Based Detection

Luminescence in solids, including gold is produced by a three step process. Firstly, an electron-hole pair is excited. Secondly, the excited electron-hole pair relaxes to a lower energy state (usually by transfer of energy to vibrations of the lattice). Thirdly, the electron and hole recombine and produce a photon [65]. Two photon luminescence (TPL) occurs when two photons produce one electron hole pair in one event. The TPL signal is amplified by resonant coupling with localised surface plasmons and can therefore be used as a way of detecting gold nanoparticles [69]

Third Harmonic Generation

The polarisation density P (dipole moment per unit volume) of a dielectric in the presence of an electric field E can be expressed as a Taylor series. In the simplest case, where P is in the same direction as E, P is given by

$$P = \epsilon_0(\chi E + \frac{1}{2}\chi_2 E^2 + \frac{1}{6}\chi_3 E^3 + ...). \tag{1.15}$$

The first term in equation 1.15 is the same as the linear polarisation density and the higher order terms give the non-linear polarisation density.

When light of the form $E = E_0 sin\omega t$ is incident on the dielectric, the resulting electric polarisation is therefore

$$P = \epsilon_0 \chi E_0 \sin\omega t + \frac{\chi}{2E_0^2} 4(1 - \cos 2\omega t) + \frac{\chi_3 E_0^3}{24}(3\sin\omega t - \sin 3\omega t) + ... \quad (1.16)$$

The third term of equation 1.16 gives rise to a wave with a frequency of 3ω, which is the signal used in third harmonic generation detection [66].

The second harmonic generation signal is forbidden for a perfectly spherical particle much smaller than the wavelength of light, because in this case, symmetry means that reversing the direction of the electric field will simply reverse the direction of the polarisation. In order for this to be true, the second term of equation 1.16 has to vanish. Therfore, the second harmonic generation term is small for spherical metal nanoparticles, as it is caused by defects and facets and any other variations present in an imperfect sphere [67]

Four-Wave Mixing Based Imaging

Four-wave mixing is a non-linear process whereby three different frequencies of light combine to produce a fourth frequency. This effect occurs when three light waves are incident on a sample. That is, $E = E_1 \sin\omega_1 t + E_2 \sin\omega_2 t + E_3 \sin\omega_3 t$. The third order term in equation 1.15 contains E^3, which will give rise to a cross term $6E_1E_2E_3 \sin\omega_1 t \sin\omega_2 t \sin\omega_3 t$. This cross term cannot be expressed as functions of ω_1, ω_2 and ω_3 only as it also contains sum and difference terms $\pm\omega_1 \pm \omega_2 \pm \omega_3$ [66]. In the four-wave mixing technique, the LSPR of the nanoparticle is excited with two temporally coincident, interfering pulses P_1 and P_2. A third pulse P_3 is used to probe the excitation. The presence of a nanoparticle on the sample has the effect of changing the susceptibility χ of the sample, which will increase the intensity of the four-wave mixing signal. This technique has been used to detect nanoparticles as small as 5 nm in diameter that have been used to label the Golgi structures (cellular organelles responsible for processing macromolecules and sending them to other parts of the cell) of HepG2 cells (a liver cancer cell line)[68].

1.4.5 Other Nanoparticle Imaging techniques

The methods described so far are optical detection methods which do not require labeling the nanoparticle in order to enable detection. However, other methods for detecting and imaging metallic nanoparticles are also available. Two methods that are commonly used for biological studies of nanoparticles and cells, and which are therefore worth mentioning in relation to this project, are transmission electron microscopy and fluorescent labeling.

Transmission Electron Microscopy

Transmission electron microscopy (TEM) is an extremely high resolution imaging system that is useful for imaging nanoparticles in cells as the particular area in the cell where the nanoparticles are found can be easily identified. The size and shape of the nanoparticles can also be easily observed using this method, which is important when using samples of colloidal particles that are not necessarily uniform. The disadvantages of TEM are that it is an expensive method, requiring lengthy sample preparation and whilst imaging of live cells is possible, it is difficult to see the biological structure of the cells as the live cells cannot be stained in the same way as the sections of cells usually used for TEM [12].

Fluorescent labeling

Fluorescent dye molecules can be attached to the nanoparticles in order to enable detection [70]. Fluorescently labelled samples are often imaged with confocal microscopy. In confocal microscopy, the sample is illuminated with a point focus and a pinhole is used to eliminate any out of focus light from the sample. This technique increases the resolution and contrast possible in comparison with viewing fluorescent samples in a wide-field microscope set up. A disadvantage of using fluorescent labelling is that conjugating the dye molecules to the nanoparticles involves an extra step in the nanoparticle synthesis which is not necessary as the nanoparticles can be easily detected without the presence of the fluorophores using the techniques described previously. Another disadvantage of using fluorescent dyes is the problem of photobleaching. That is, the signal given out by fluorescent dyes becomes weaker the longer they are exposed to light at the fluorescence excitation wavelength. The absorption and scattering signal of metal nanoparticles due to the LSPR does not fade over time.

1.4.6 Discussion

There are many methods under development for the imaging of gold nanoparticles with a focus on biomedical applications. Each of these methods has specific advantages and disadvantages and in reality there is no one method which is ideally suited to all applications. Therefore, the development of different detection/characterisation methods for metal nanoparticles can be viewed as the development of a toolkit, of which the aim is that for any given application there should be a useful way of obtaining the required information from the system. The two nanoparticle imaging systems that have been focused on in this project, darkfield microscopy and spatial modulation microscopy, make up part of the nanoparticle characterisation toolkit.

The particular advantages of darkfield microscopy are that it is fast, low cost, there is no requirement to induce physical changes in the sample by, for example heating it or otherwise disrupting the sample through e.g. interaction with a SNOM tip. Also, a large area of the sample can be viewed in real time. These features make darkfield

microscopy suited to imaging of cells and nanoparticles. The main disadvantage is that it is completely scattering based, which means it is not suited to imaging very small nanoparticles.

The main advantages of SMM are that it can quantitatively detect the LSPR signal due to either scattering or absorption and can therefore be used to detect nanoparticles of sizes down to 5 nm. There is also no requirement to heat the sample or otherwise directly interact with it further than illuminating the nanoparticles at the LSPR wavelength and it is also relatively low cost in comparison with, for example electron microscopy techniques. The main disadvantage of SMM is that it is, by nature a slow, point by point measurement method.

1.5 Project Outline and Original Contribution

Chapters 2 and 3 of this thesis relate to darkfield microscopy. In darkfield microscopy, the sample is illuminated and only the light that has been scattered back from the sample is collected and sent to a CCD camera. The parts of the sample which scatter light more strongly therefore show up as bright areas on a dark background. This method enables the imaging of objects such as nanoparticles, which are too small to see in brightfield microscopy, but which may scatter strongly and can therefore be seen under darkfield illumination. Darkfield illumination has been used to detect the presence of gold nanoparticles in dendritic cells. three-dimensional maps have been built up of the cells in order to obtain more information about the position of the nanoparticles in the cells than can be obtained from a two-dimensional image.

A hyperspectral imaging system has also been developed, which uses the darkfield method to measure the optical spectra of single nanoparticles and clusters of nanoparticles. These spectra have been correlated with TEM images of the individual particles to demonstrate how the size and shape of individual particles and small clusters can affect their optical properties. The hyperspectral darkfield technique is different from other hyperspectral darkfield techniques available in that the sample is illuminated with low power light at different wavelengths rather than illuminating the sample with high power white light. There is a clear advantage to this hyperspectral darkfield system as high power laser irradiation can cause damage to delicate biological samples such as live cells so it is desirable to illuminate such samples with low power light.

The second microscopy method which has been developed in this project is the spatial modulation microscopy method (SMM), which is discussed in chapter 4. Spatial modulation microscopy has been used previously to detect and measure the spectra of single nanoparticles [13]. In this project, the first steps have been made in implementing a new detection scheme, that can image an area of 20×20 μm on a sample, therefore

simultaneously imaging multiple nanoparticles, which has possible applications in cell imaging including 3D imaging of cells.

In order to develop this fast scanning version of SMM, a CMOS line camera [71; 72] has been used which detects the signal in a line of pixels simultaneously as well as using a phase stepping technique which negates the need for using a lock-in amplifier in the set up.

Chapter 2

Nanoparticle Spectroscopy

2.1 Introduction

The work in this chapter relates to spectral measurements of plasmonic nanoparticles. Spectral measurements are important in the characterisation of plasmonic nanoparticles as the LSPR's of the nanoparticles produce peaks in their absorption and scattering spectra. Since the LSPR depends on the dielectric constant of the surrounding environment, shifts in spectral peaks indicate changes in the local environment. This property can therefore be exploited in sensing applications including biological sensing [73; 74]. The first step in the development of a system capable of measuring spectra of single particles, was to measure the bulk spectrum of a solution of nanoparticles. Measurements of the spectrum of a solution of nanorods using a supercontinuum light source and an acousto-optic tuneable filter (AOTF) are therefore presented first in this chapter. The method of using an AOTF and a supercontinuum source to perform a wavelength scan was then further extended to create a hyperspectral darkfield microscope capable of measuring the spectra of single metallic nanoparticles particles and small particle clusters.

Darkfield microscopy has previously been shown to be a powerful tool for imaging metallic nanoparticles and measuring their spectra [44]. The hyperspectral darkfield method presented in this chapter enables the simultaneous measurement of multiple nanoparticles on a sample, as opposed to other hyperspectral darkfield methods where scattered light is collected from one nanoparticle at a time and the spectrum is then measured with a spectrometer [75; 76]. Many current hyperspectral darkfield methods which simultaneously measure multiple nanoparticles at once, use broadband white light illumination and then filter out different spectral components before detection [77; 78]. While studies which use white light illumination and a spectrometer are extremely sensitive and can go down to single molecule sensitivity [79; 80], the broadband irradiation of nanoparticles can cause significant heating of the particles, which is unfavourable for in-vitro

studies of sensitive biological systems [81]. It is possible to use this method to analyse nanoparticles in biological systems [82], as is also demonstrated by commercially available hyperspectral darkfield systems [83]. However, the problem of heating of biological samples is a concern in this case.

In this chapter, the hyperspectral darkfield system has been used to measure spectra of a number of different nanoparticle samples. The hyperspectral darkfield method has been used to measure the longitudinal and transverse resonances of lithographic gold nanoantennas. The system has also been used to perform spectral measurements on smaller, colloidal nanoparticles. Spectra of hollow gold nanoparticles have been measured and correlated with transmission electron microscopy (TEM) measurements. Finite element modelling of hollow gold particles has been used in order to evaluate the experimentally measured spectra. The darkfield microscope has also been used to measure spectra of silver nanocube clusters, which have been used to support polarisation measurements in order to characterise their plasmonic response.

2.2 Measuring the Spectrum of a Solution of Metallic Nanoparticles

2.2.1 The Acousto-Optic Tuneable Filter

To perform spectral measurements, a range of different wavelengths of light must be available. One way to achieve an easily tuneable wavelength source is with the use of a supercontinuum laser and an acousto-optic tuneable filter (AOTF).

The acousto-optic tuneable filter can be used to select a particular frequency of light from the supercontinuum spectrum. Bragg diffration is used to achieve this effect. Bragg diffraction occurs when light is incident on a crystal, and the wavelength λ at which it occurs depends on the angle of incidence of the light θ and the lattice spacing of the crystal d, through the relation $2d\sin\theta = n\lambda$, where n is a whole number, as illustrated in figure 2.1. Constructive interference occurs for the wavelength of light which fulfils this condition, which can be used to filter a particular wavelength of light out of broadband white light.

In the acousto-optic tuneable filter, a radio frequency piezo electric transducer creates acoustic waves in a crystal. The density changes created by the acoustic wave consist of periodic planes of different refractive indexes. This is equivalent to an effective crystal lattice, as incident light will be scattered when it comes into contact with the different planes in the same way that in traditional Bragg diffraction light is scattered off rows of atoms in the crystal lattice. In the AOTF, the lattice spacing d is controlled by changing the frequency of the RF driving voltage that drives the piezo electric transducer and therefore the wavelength of the acoustic wave in the crystal.

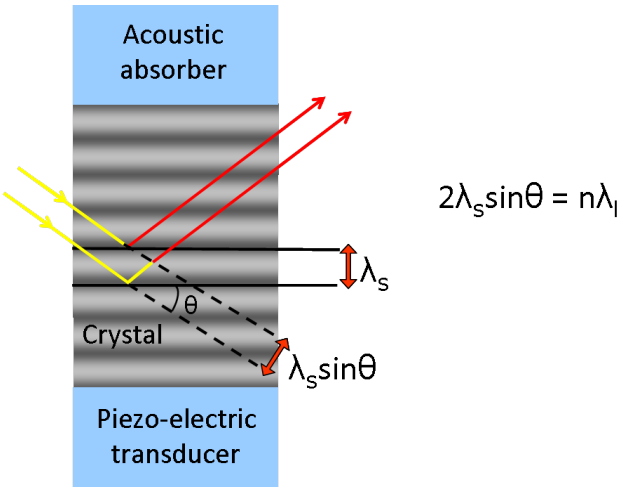

Figure 2.1: Diagram showing how the acousto-optic tuneable filter can be used to select a single wavelength from white light using the Bragg effect.

2.2.2 Extinction Spectra Measurement Method

A system was set up for measuring the extinction spectrum of a solution of colloidal nanorods in water. This was achieved by using the AOTF, to sweep through the required frequency spectrum and a silicon photodiodode, to detect the light transmitted through the sample. A chopper was also included in the set-up, enabling use of a lock-in amplifier, to increase the signal to noise ratio of the transmitted light (See figure 2.2).

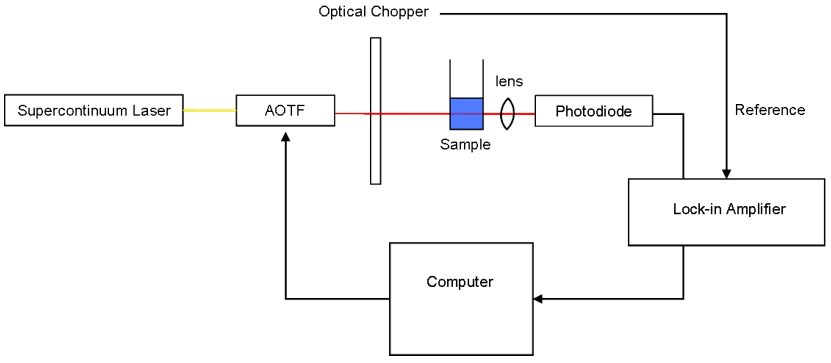

Figure 2.2: System for measuring extinction spectra of a solution of nanoparticles

The AOTF was driven by a programmable IDDS Isomet programmable frequency synthesiser, which was programmed using labview firstly, to cause the AOTF to output light at a required frequency, which was easily switchable between any frequencies in the range output by the supercontinuum and secondly to perform a frequency sweep, either continuous or stepped. The output from the photodiode was also incorporated into the labview program so that spectral measurements could be performed automatically. The automated process of measuring a scan is schematically illustrated in figure 2.3.

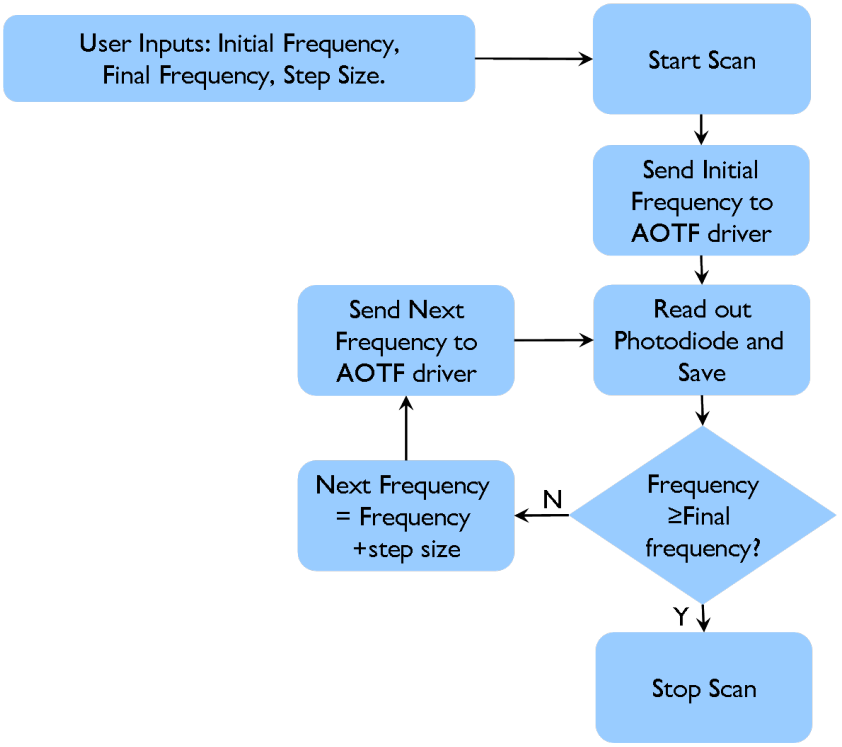

Figure 2.3: Process of measuring an extinction spectra of a solution of nanoparticles

In order to account for any wavelength dependence of the sensitivity of the photodiode and of the supercontinuum laser power, a base line was measured by taking a spectrum for a sample of water of the same volume and in the same cuvette as the nanoparticle solution was measured. The baseline was then subtracted from the data taken for the nanoparticle solution in order to produce a nanoparticle extinction spectrum.

2.2.3 Spectrum of a Solution of Colloidal Nanoparticles

In order to show that the system was capable of detecting the LSPR of nanoparticles, an extinction spectrum of a sample of colloidal nanorods was measured in the wavelength range of 500 to 900 nm and found to be in good agreement with a spectrum of the same sample measured with a UV-Vis spectrometer (as seen in figure 2.4).

The LSPR peak is seen to occur at the same wavelength on both spectra, showing that the system can correctly measure the LSPR of a solution of colloidal particles. The width of the peaks is mainly due to the fact that the particles in the solution are not completely homogeneous in size.

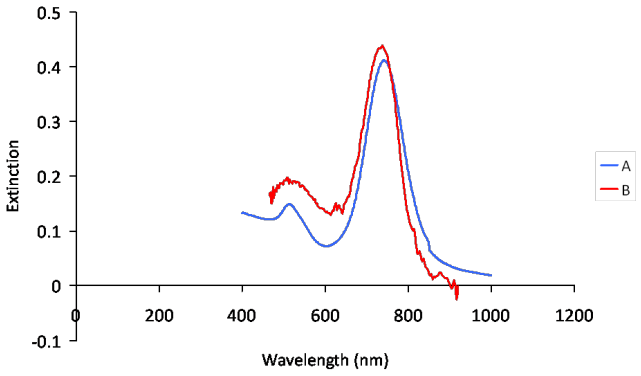

Figure 2.4: Comparison of extinction spectra of nanorods measured using a UV-Vis Spectrometer (A) and the AOTF system (B)

2.3 Hyperspectral Imaging - Experimental Methods

2.3.1 Darkfield Microscopy Methods

A home built darkfield microscope has been used to collect the results shown subsequently in this chapter and in the next chapter, which has been set up as follows. Firstly, the relevant wavelength required for illuminating the sample is selected from a supercontinuum source with an acousto-optic tuneable filter (AOTF) as explained in section 2.2.

Secondly, a ring of light is produced by sending the laser beam into an optical fibre at a slight angle, thereby coupling to one mode of the fibre, which has the effect of producing a hollow cone of light from the fibre. The cone of light then enters the darkfield ring of the microscope objective. Light scattered from the sample is collected with a CCD. The sample is mounted on a stage which allows the user to focus and move to different parts of the sample. Brightfield images were produced using a white light lamp behind the sample. See figure 2.5 for a schematic representation of the setup.

Measurements of nanoparticle spectra were also automated using Labview. The basis of the program used followed the same process as shown in figure 2.3 except the step of collecting data from the photodiode was replaced with capturing an image on the CCD camera and saving it. In addition to the continuous sweep process shown in figure 2.3, a stepped scan was also implemented in order to allow refocussing of the image for different wavelengths. The stepped scan was particularly useful for scans that included infra-red wavelengths for which the microscope objective was not well corrected for chromatic aberration.

In this project the darkfield microscope was tuned to detect nanoparticles with an LSPR in the near infrared part of the spectrum. This wavelength range is the most important

for biological applications, as transmission of light through biological tissue is highest in the near infrared.

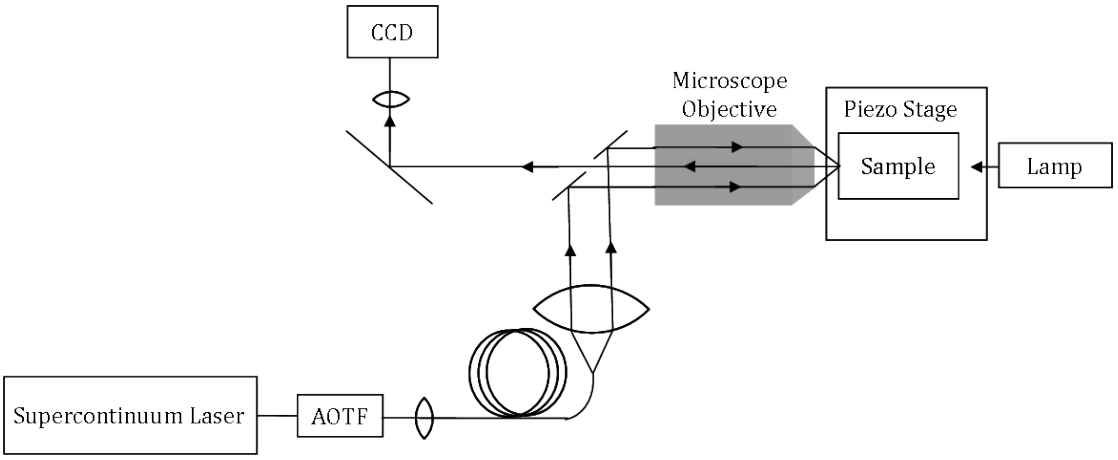

Figure 2.5: Experimental Set-up

2.3.2 Calibration of Darkfield Imaging System

Both the power of the laser light and the sensitivity of the camera have a dependency on wavelength as can be seen in figures 2.6 and 2.7.

Because of the variations in laser power and camera sensitivity with wavelength, the system needs to be well calibrated, in order to show that any change in signal seen is due to the nanoparticles, and not to the inherent changes in the sensitivity of the system at different wavelengths. A method of producing a calibration curve for the whole system is to measure the light scattered from a white paint pigment (TiO_2) sample, using the darkfield microscope, at different wavelengths. The white paint should scatter equally well at all wavelengths of light relevant here. The calibration curve produced by this method includes the camera sensitivity and laser power dependence on wavelength as well as any other possible wavelength dependencies in the system. (See fig 2.8)

The laser power was measured with a power meter for a range of wavelengths after the light had been filtered by the AOTF. The camera sensitivity was also obtained by looking at the broadband scattering source under darkfield illumination and correcting for the previously measured laser power by controlling the amplitude of the acoustic waves in the AOTF. The measured camera sensitivity agreed well with the quantum efficiency stated by the manufacturer.

2.3.3 Image Processing Methods

The wavelength tuneable darkfield setup can be used to collect hyperspectral information for an entire image of 1000×1000 pixels, covering an area on the sample of $145 \times 145 \mu$m.

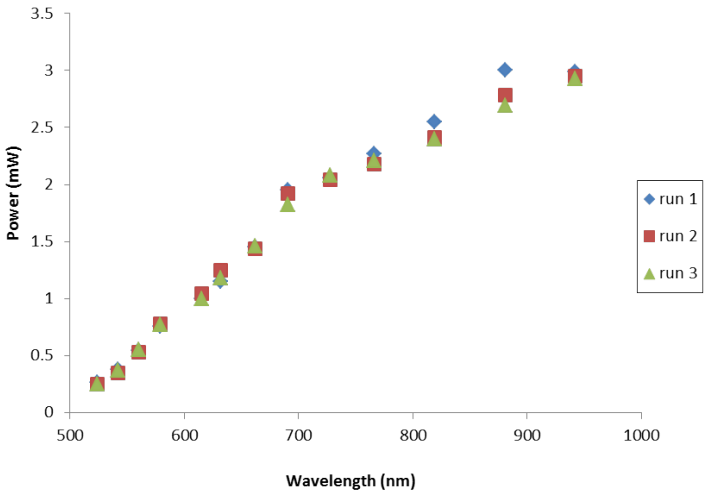

Figure 2.6: Dependency of laser power on wavelength for supercontinuum source

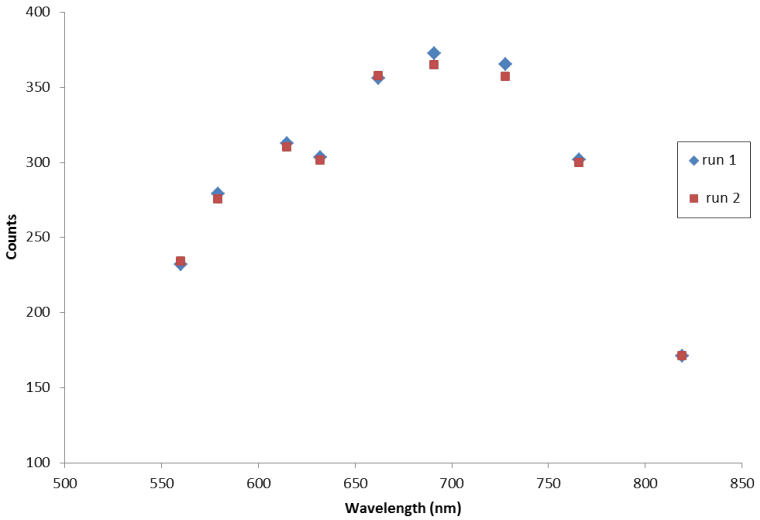

Figure 2.7: CCD Camera sensitivity at different wavelengths. The values measured here agree well with the quantum efficiency stated by the manufacturer.

The hyperspectral information is collected as follows: Using the AOTF, controlled via a Labview program, a wavelength scan of the supercontinuum light is performed. The same Labview program is used to take between three and ten images (depending on user requirement) for each wavelength of the scan with a CCD camera. From these images an averaged image is produced for each wavelength in order to reduce noise. The series of averaged images is then used in the next stage of image processing, which is performed as follows, using Matlab.

First, areas of interest (AOIs) are selected on the image. Next, the intensities of those AOIs are collected for each of the images in the series. Since each image in the series

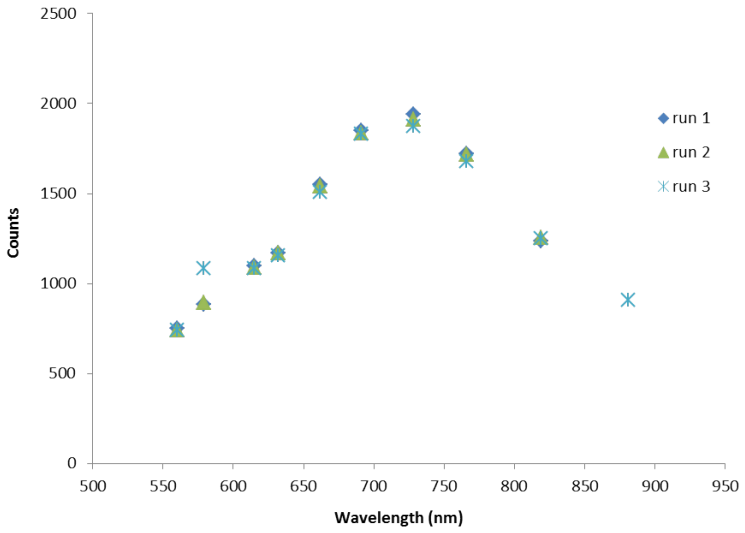

Figure 2.8: Calibration curve showing wavelength dependent sensitivity of dark-field microscope

represents a measurement at a different wavelength, a spectrum is therefore built up for each area of interest.

The sizes of the areas of interest are set to be 7×7 pixels, an area on the sample of approximately $1 \times 1 \mu$m, in order to fully include all the light from a particular nanoparticle, without including too much background signal or light from another neighbouring particle. The positions of particles are also tracked from image to image using a cross correlation function, and the positions of the areas of interest are adjusted accordingly in the program, by shifting the image to the peak of the cross correlation. Position tracking is important, as sometimes the particles may have moved slightly from image to image due to the sample slipping, for example. A movement of the sample of about 500 nm is enough to move the particles partially out of their defined areas of interest, which can disrupt results.

Two different measures of particle intensity are made by the image processing program. Firstly the total number of counts that have arrived at the CCD over the entire area of interest, and secondly the maximum value of counts for any one pixel in the area of interest. It has been found that using the maximum value gives more accurate results as this usually comes from the centre of the bright spot of interest, which is always comfortably inside the area of interest. Even with the methods described above, the edges of bright spots may move slightly outside the areas of interest, which leads to a change in the proportion of light collected from a nanoparticle from image to image. If this happens, the total counts method becomes inaccurate. Also, the total counts method includes a lot of pixels which contain no light from the nanoparticle and may contain background light from other sources with could affect the accuracy of the results.

Therefore, in this thesis the maximum counts from one pixel in the area of interest is used in most cases as the measure of intensity of scattered light.

2.4 Measurement of Longitudinal and Transverse LSPR modes of Gold Nanoantennas with Polarised Light

The hyperspectral darkfield system has been used to measure the scattering spectra due to the longitudinal and transverse modes of a sample of nanoantennas. The nanoantennas consist of two arms, each arm is 200 nm in length, 100 nm wide, and 25 nm thick with a gap between the arms of 20 to 80 nm, on a silicon substrate [85]. The nanoantennas were fabricated lithographically by M. Abb (University of Southampton). In order to only collect light which has been scattered by the nanoparticle at a particular polarisation angle, a polarisation filter was added to the darkfied setup described in section 2.3.1 in front of the CCD camera and a depolariser was added after the AOTF to un-polarise the polarised light exiting the AOTF. In order to account for any polarisation dependence of the system, this was measured by measuring the polarisation dependence of a broadband scattering sample in the system and then correcting for this. The polarisation angle was chosen to be zero when the transmission axis of the polarisation filter was equal to the longitudinal axis of the nanoantennas. As the nanoantenna sample was at a slight angle in the microscope, the polariser was aligned to the sample by illuminating the sample with light with a wavelength of 900 nm and adjusting the rotation angle of the polariser to find where transmitted light was at a maximum. The alignment was then confirmed by drawing a line on top of a column of antennas on the image in PowerPoint and seeing how much the line was rotated from the vertical. Spectra were then measured for polarisation angles of $0° \pm 1°$ and $90° \pm 1°$. Individual spectra for all nanoantennas in the array are measured simultaneously for any given polarisation angle. However the spectra of six typical antennas are presented here for clarity. Figure 2.9 shows the positions of the six nanoparticles in the array.

Figure 2.10 shows the variation in light scattered by nanoantennas 1-6 with wavelength. The longitudinal resonances measured with vertically polarised light (0°) are shown in fig. 2.10a. The transverse resonances measured with horizontally polarised light (90°) are shown in fig. 2.10b.

From figure 2.10 it can be seen that the positions of the longitudinal and transverse spectra of the antennas have been measured successfully using the hyperspectral darkfield imaging system. The longitudinal plasmon resonance for the antennas is found to be at a wavelength of 890 nm +/- 34 nm and the transverse resonance is at 730 nm +/- 18 nm. The reason for the larger difference in peak position between antennas for the longitudinal resonance is because the gap size between the antennas has a higher level of uncertainty than the other dimensions.

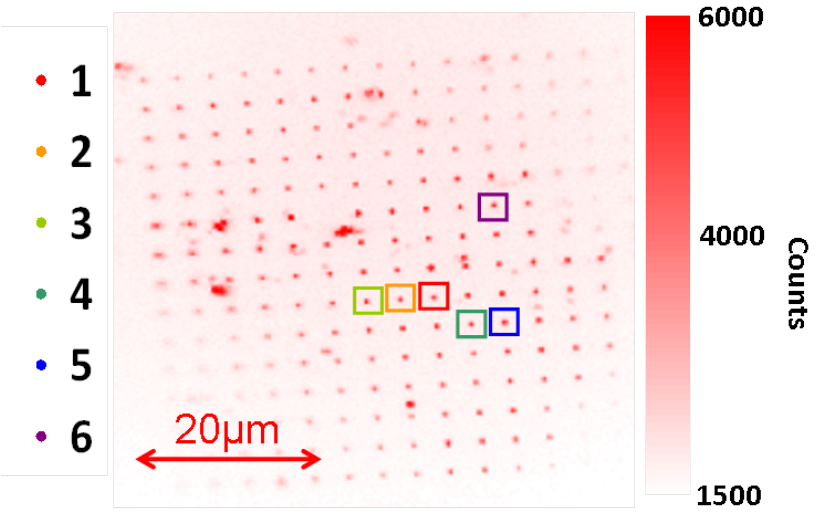

Figure 2.9: Positions of nanoantennas for which spectra have been measured using horizontally and vertically polarised light. The image shown here has been taken at a wavelength of 728 nm using vertically polarised light

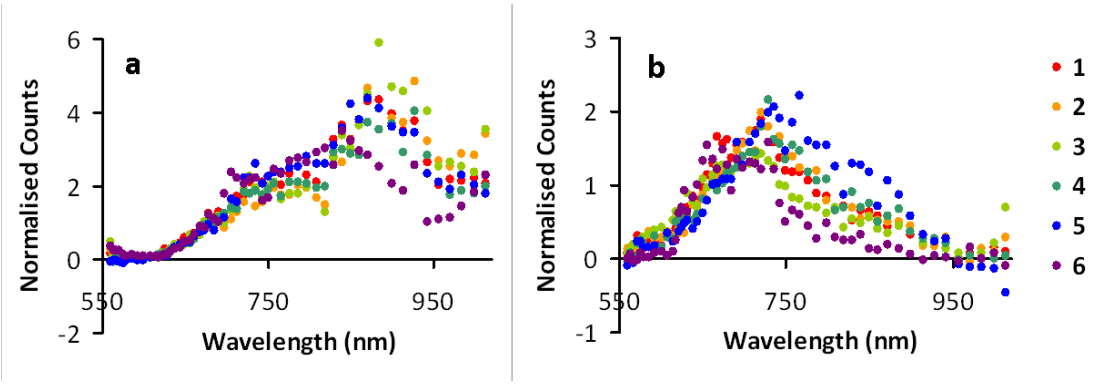

Figure 2.10: a) Spectra of nanoantennas measured using polarised light with a transmission axis aligned with the long axis of the nanoantennas. b)Spectra of nanoantennas measured with polarised light with a transmission axis aligned with the short axis of the nanoantennas.

It is expected that the resonance along the long axis of the antenna would be redshifted in comparison to the resonance along the short axis of the antenna, since the long axis can support a longer wavelength mode and this is indeed what is observed.

2.5 Polarisation Dependence of Gold Nanoantennas

It is also interesting to demonstrate the difference in the polarisation dependence of the nanoantennas at different wavelengths by choosing two wavelengths (the peaks of the longitudinal and transverse resonance) and scanning over polarisation angle between 0 and 180 degrees.

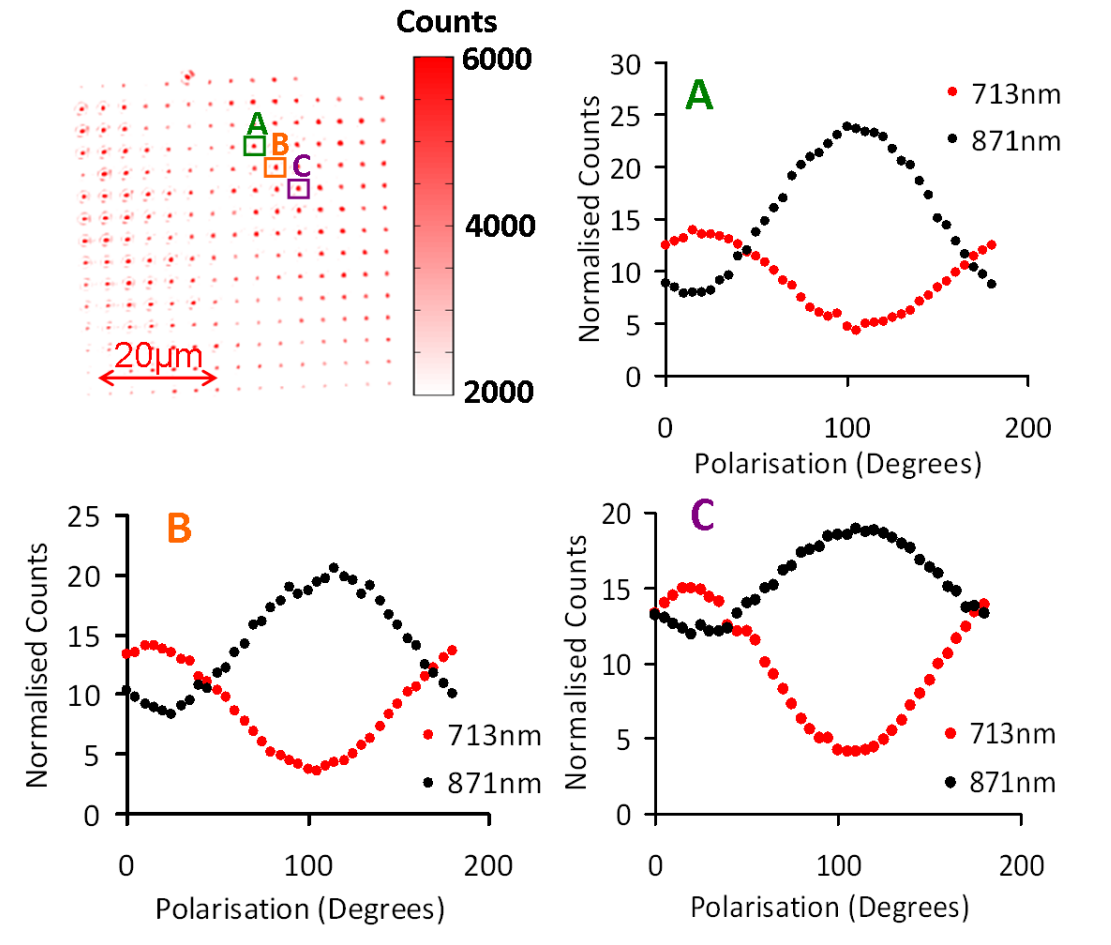

Figure 2.11: A false colour darkfield image of gold nanoantennas taken at 713 nm, 0 degrees polarisation, showing the positions of antennas A, B and C. Plots show the intensity variation of the antennas with polarisation angle for two wavelengths, 713 nm and 871 nm.

Figure 2.11 shows how the light scattered from gold nanoantennas at different polarisation angles varies in intensity due to the longitudinal and transverse plasmon resonances. The polarisation dependence was measured using the hyperspectral darkfield setup with a polariser placed in front of the CCD camera (the same arrangement as in section 2.4) However, in this case the wavelength of incident light was kept constant and the polariser was rotated to collect different polarisations of light scattered from the antennas. The antennas were placed in the setup such that the long axis of the antennas were in line with the transmission axis of the polariser at the 100° position.

It can clearly be seen from figure 2.11 that when the transmission axis of the polariser is parallel to the long axis of the nanoantenna, there is an increase in the intensity of the 871 nm wavelength light. When light with a wavelength of 713 nm is shone onto the antennas, the measured polarisation dependence is 90° out of phase with the polarisation dependence seen for the longer wavelength light and shows a peak at 10°, when the transmission axis of the polariser is parallel to the short axis of the antenna.

These results are to be expected, since 871 nm is the position of the longitudinal LSPR and 713 nm is the position of the transverse LSPR peak.

2.6 Hyperspectral Imaging of Colloidal Gold Nanorods

2.6.1 Identification of Single Nanorods using Polarised Light

The hyperspectral darkfield imaging method is useful for simultaneously measuring the spectra of many nanoparticles or particle clusters on a sample. The measured spectra can be used to identify whether or not nanoparticles are present on the sample. The measured spectra can also provide a good indication of whether or not the detected scattered light is due to single nanoparticles or due to a nanoparticle cluster or aggregate as the spectrum for a cluster or aggregate would be expected to be different from a single particle spectrum due to coupling effects between the nanoparticles [44]. If a measured spectrum agrees well with the theoretically predicted spectrum for the size and shape of colloidal nanoparticles used then this evidence is a strong indication that the scattered light which has been measured is due to a single particle.

However, within a sample of colloidal nanoparticles there is some variation in nanoparticle size, and the size variations in nanorods can also cause the LSPR to change so it would be useful to know if differences between spectra of different bright spots on the sample are due to size variations or to the presence of clusters of nanoparticles.

When polarised light is shone onto a nanoparticle, for the LSPR to be excited the direction of the oscillation of the electric field of the light must match up with the direction of oscillation of electrons in the nanoparticle, required for that particular LSPR mode. That is, for nanorods, the polarisation of light required to excite the longitudinal LSPR mode is perpendicular to the polarisation required to excite the transverse mode, therefore a polarisation dependence of the LSPR will be observed from a sample of nanorods deposited on a glass substrate.

In order to attempt to identify single nanorods, the polarisation angle of light was changed and any changes in the intensity of light scattered from the sample were noted.

Some of the bright spots on the sample were seen to have a polarisation dependence. An example is shown in figure 2.12 which shows two images of a sample of colloidal nanorods taken at two orthogonal polarisations. It can be observed that some bright spots that are present in the first image are not seen in the second image.

The bright spots that were found to have a polarisation dependence were therefore chosen as likely candidates for single nanorods. While this method can give a reasonable indication of whether bright spots are due to single nanoparticles, small clusters of nanoparticles can also show a polarisation dependence. For example two nanorods that

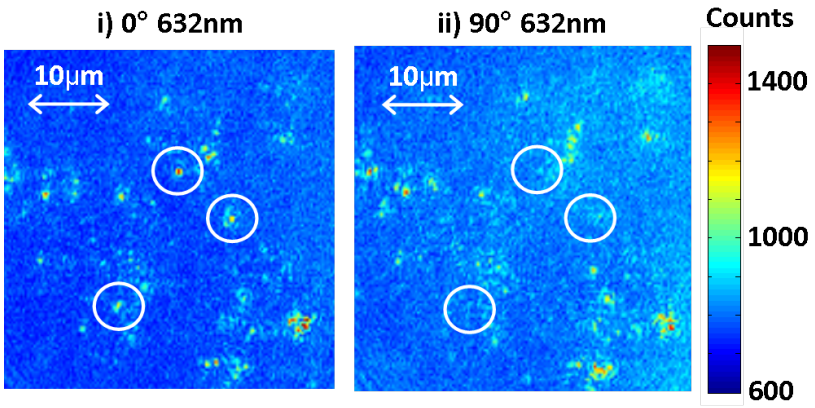

Figure 2.12: Darkfield image of the same area on a sample of colloidal nanorods taken at the same wavelength but at two orthogonal polarisation angles.

are closely spaced and orientated in the same direction would be expected to show a polarisation dependence.

2.6.2 Spectral measurements of Individual Gold Nanorods

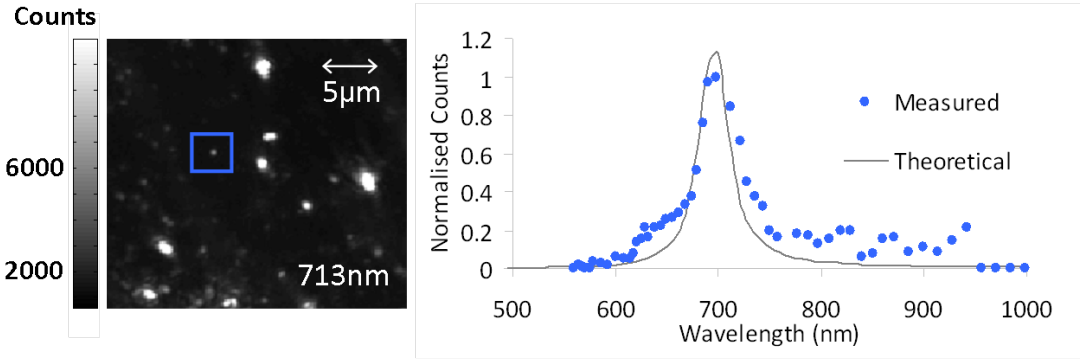

Figure 2.13: A darkfield image of a sample of gold nanorods taken at an illumination wavelength of 713 nm with a measured spectrum of the indicated bright spot on the image, shown along with a theoretically predicted spectrum.

Figure 2.13 shows a spectrum for a single nanorod candidate measured using the hyperspectral imaging system. The nanorod is from a sample of OEG coated nanorods with average length 47 nm and average width of 16 nm, deposited on a TEM grid. The image was taken with an exposure time of 0.2 seconds. A theoretical prediction of the extinction spectrum produced by Martina Abb (University of Southampton) is also shown. The theoretical spectrum has been created by performing finite element analysis on a cylindrical rod with hemispherical end caps of length 47 nm (including end caps), diameter 16 nm, in air. The height of the theoretical peak has been normalised to fit on the graph with the measured peak. The position of the measured peak agrees well with the theoretical prediction of the extinction spectrum for a single nanorod with the same dimensions as the average nanorod dimensions in the sample. The agreement of the

measured peak with the theoretically predicted LSPR strongly suggests that this candidate is a single nanorod. However, it is difficult to make such a statement with surety without further information from, for example, a TEM image of the same nanoparticle.

From the darkfield images and spectra alone, it is difficult to know whether the particles being measured are truly single particles, even though polarised light has been used to identify likely single particle candidates. In addition, a further disadvantage is that the polarisation method for identifying single nanoparticles can only be used for asymmetric nanoparticles such as nanorods and cannot be used for identifying for example, branched or spherical shaped particles. It is also difficult to know, where clusters have been measured, how many particles are in the cluster. Therefore further study of the measurement of single particle spectra using the darkfield hyperspectral imaging system has also been conducted. Spectral measurements correlated with transmission electron microscopy (TEM) images of spherical hollow gold have been measured in order to directly compare the size and shape of particles with their spectra.

2.7 Hyperspectral Measurements Correlated with TEM Images of Hollow Gold Nanoparticles

2.7.1 Experimental Methods

For the purpose of comparing single nanoparticle spectra with TEM images, hollow gold 'nanocages' were deposited onto copper TEM finder grids, which had previously been coated with formvar and carbon. Hollow gold nanoparticles were chosen because it was not possible to detect single hollow gold particles using the polarisation dependence method. Hollow gold particles are of particular interest for biomedical applications because their LSPR falls in the biological near IR window and biological molecules can be encapsulated inside the cavity in the particle and let in and out selectively depending on the size of the molecules and the size of the pores in the hollow gold particles [23]. Hollow gold particles have also been used to trigger release of drugs from liposomes after absorption of infrared light causes the nanoparticles to heat up and cause the liposomes to burst [86].

Figure 2.14 shows three images taken with a TEM at different magnifications and one image taken with the darkfield microscope with incident light at a wavelength of 713 nm. The letters a to p correspond to the same particles/clusters of particles in each image. The letters of the finder grid (for example the letter 'O' shown in the top left corner of fig. 2.14 i)) were used to identify a particular part of the grid to be mapped. Larger nanoparticle aggregates were then used as landmarks in order to find a particular group of single nanoparticles in the darkfield microscope, which had been previously imaged in the TEM. The hyperspectral imaging method was then used to measure the spectra

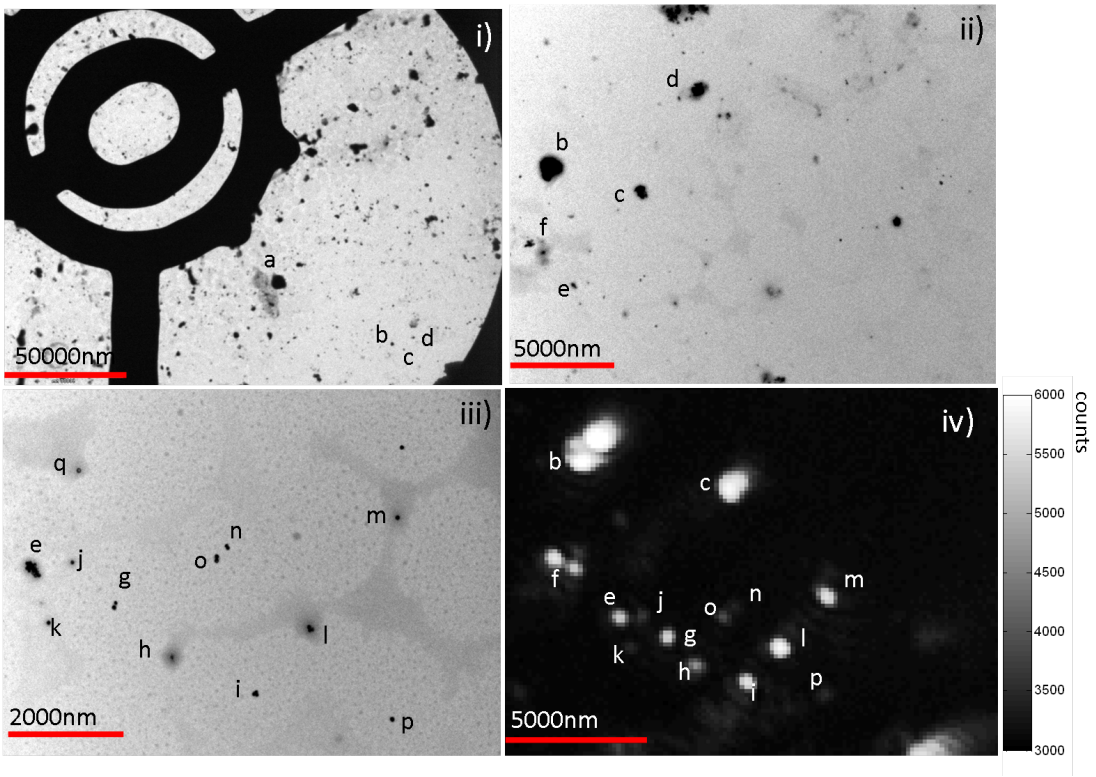

Figure 2.14: i),ii),iii) TEM and iv)darkfield images of hollow gold nanoparticles and nanoparticle clusters

of single particles and small clusters. The error in the method is thought to mainly originate from an error in the focus of each image. The microscope objective used in the experimental set up was not chromatically corrected for wavelengths outside of the visible range. In order to correct for this, the focus was adjusted manually between images. For wavelengths below around 700 nm, the objective was corrected for chromatic aberration and the manual focus adjustments were not needed. In addition to measuring the spectra of the nanoparticles in the hyperspectral darkfield microscope, finite element analysis was performed in order to provide a theoretical reference to compare the measured spectra with.

2.7.2 Comparison of Theoretically Predicted and Measured Spectra

Figure 2.15 shows the spectrum of particle m (which has previously been identified in fig 2.14) along with close up TEM and darkfield images of the particle. The darkfield image shown has been measured at 713 nm, close to the peak of the spectrum. Figure 2.15 also shows a theoretical fit to the experimental spectrum measured for a particle m, a single hollow gold particle in the hyperspectral darkfield microscope. Since the hollow gold nanoparticles were measured on a formvar coated TEM grid, in the FEM models, an average refractive index (1.2) of air (1.0) and formvar (1.4) has been used as an approximation of the refractive index of the surrounding material. The size of the

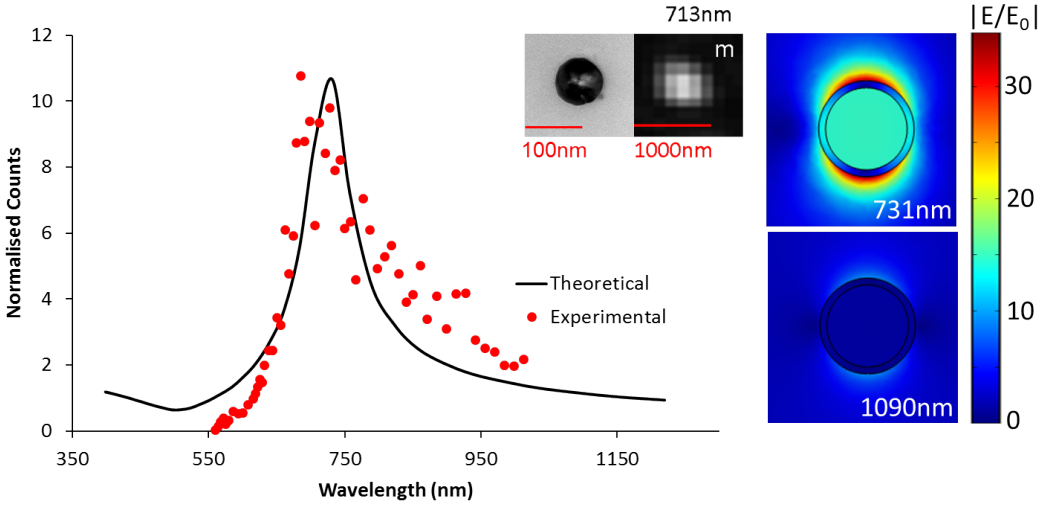

Figure 2.15: Spectrum of particle m measured in the hyperspectral darkfield microscope and a theoretical fit to the data produced by finite element analysis. Darkfield and TEM images of particle m are shown as insets and a near-field map of the electric field enhancement around the modelled particle on and off resonance is also shown.

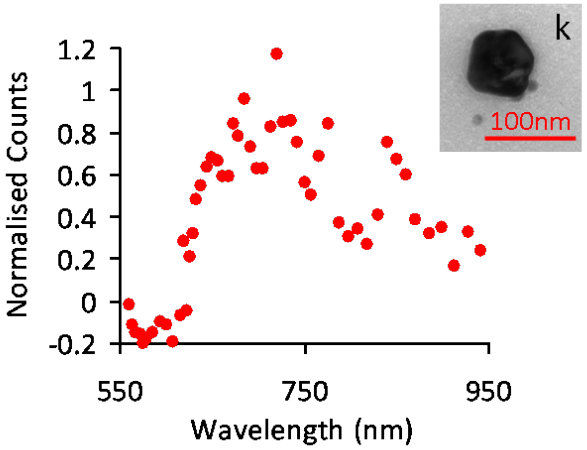

Figure 2.16: Spectrum of particle k measured in the hyperspectral darkfield microscope along with a TEM image of the particle.

particle was taken to be 83 nm in diameter, measured from the TEM image. It is difficult to determine the shell thickness from the TEM images as the shell is not truly a constant thickness. However, for modelling purposes a shell of constant thickness was used and this thickness was estimated by fitting the theoretical spectrum to the experimental data. A shell thickness of 5.5 nm was found to produce a good fit to the experimental data for particle m. The height of the theoretical peak was scaled to the same height as the experimental data. A near-field map of the electric field enhancement($|E| \,/\, |E_0|$) shows that the LSPR peak is due to a dipole mode. Particle m shows a resonance at 685 nm $\pm$ 10 nm which is in agreement with previously measured hollow gold studies

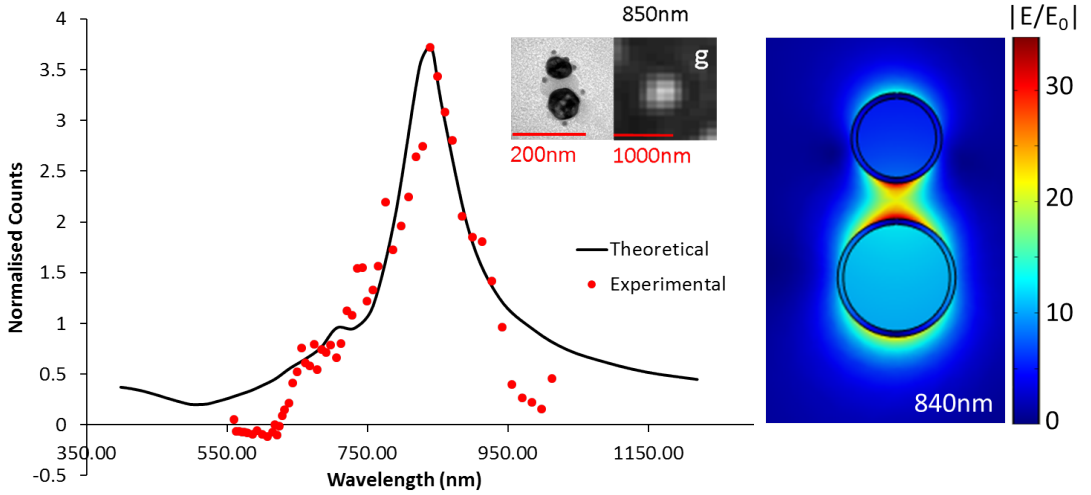

Figure 2.17: Spectrum of particle m measured in the hyperspectral darkfield microscope and a theoretical fit to the data produced by finite element analysis. Darkfield and TEM images of particle m are shown as insets and a near-field map of the electric field enhancement around the modelled particle at the LSPR is also shown.

[87]

Figure 2.16 shows the measured darkfield spectrum of particle k, another single particle. The measured signal for particle k is weaker than for particle m since particle k is smaller and therefore does not scatter light as strongly as particle m. However the peak in the scattering spectrum at the LSPR wavelength is still detectable, demonstrating that the hyperspectral darkfield technique can be used to measure the scattering spectra of particles with a diameter under 100 nm.

Figure 2.17 shows the spectrum of two hollow gold particles closely spaced with a close up TEM image and a darkfield image illuminated with 850 nm wavelength light. In the darkfield image the light from the individual particles is indistinguishable. The spectrum shows that a coupling of the two particles has produced a redshift of the LSPR peak to 840 nm. A theoretical fit to the experimental spectrum is also shown, which was produced by modelling two particles with diameters of 79 nm and 60.5 nm, a separation of 24 nm and shell thicknesses of 3.7 nm. A near-field map of the electric field enhancement shows the field enhancement is concentrated in the gap between the two particles. The thickness of the two shells was assumed to be approximately the same as large differences between the shell thicknesses of the two particles produced Fano resonances which were not observed experimentally. However a slight difference in the shell thicknesses of the two particles could partly account for the difference between the theoretically predicted and observed spectra. It can be seen from figure 2.18 that for two hollow gold particles that are extremely close together, a red shift is seen in the measured spectra, which is in agreement with studies of strongly interacting nanoshells [89]

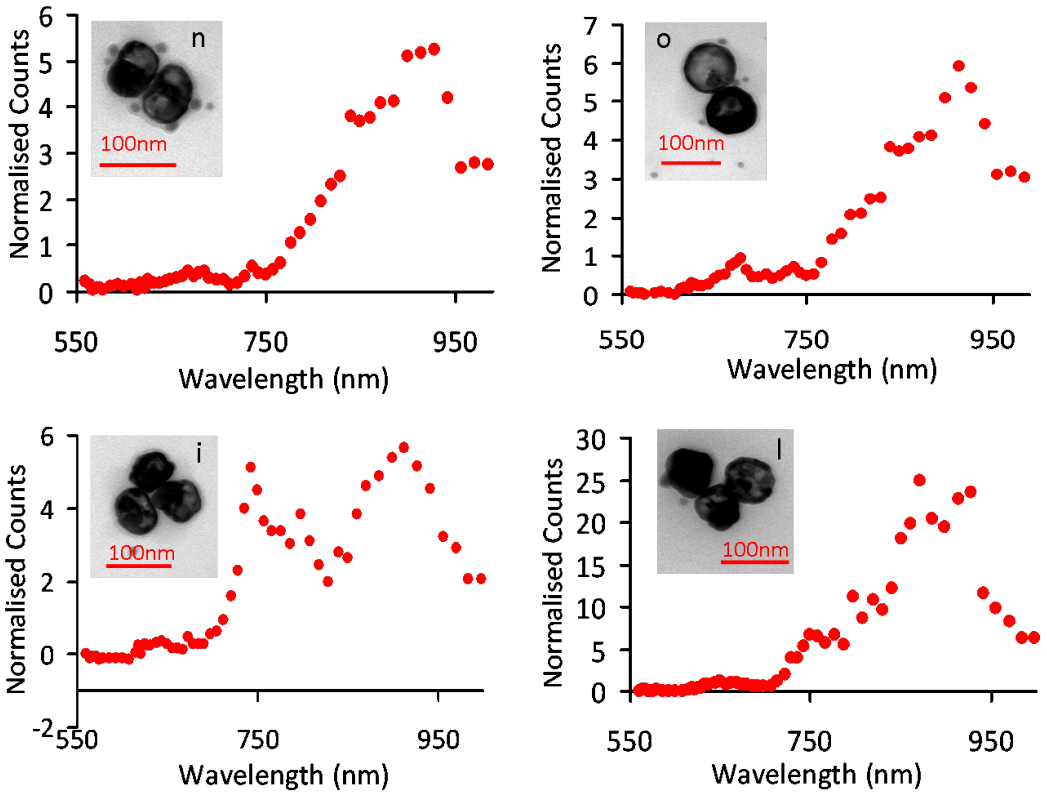

Figure 2.18: Spectra of dimers n and o and trimers i and l measured in the hyperspectral darkfield microscope, along with close up TEM images.

Figure 2.18 shows spectra of hollow gold particle trimers. Both spectra show clear peaks at around 900 nm but the spectrum for trimer i also shows a peak at around 750 nm. This could be due to the fact that the two clusters have different shapes or because they have different orientations. In addition, the light beam is polarised by the AOTF. A depolariser was used to un-polarise the light but a slight polarisation dependence remained. Another factor which could affect the spectrum is that l has a larger total size than i. The spectrum of trimer l seems to show a small shoulder at around 750 nm (the position of the second peak in the spectrum of trimer i) as well as a small peak at around 650 nm. However these features are too small compared to the experimental error to be of clear interest. The particles which make up the trimers shown here are fairly irregular and the shell thicknesses are not constant. The complex LSPR response of the trimers could be due to plasmonic Fano resonances caused by a mismatch in size or shell thickness between the different nanoparticles in the trimers [88].

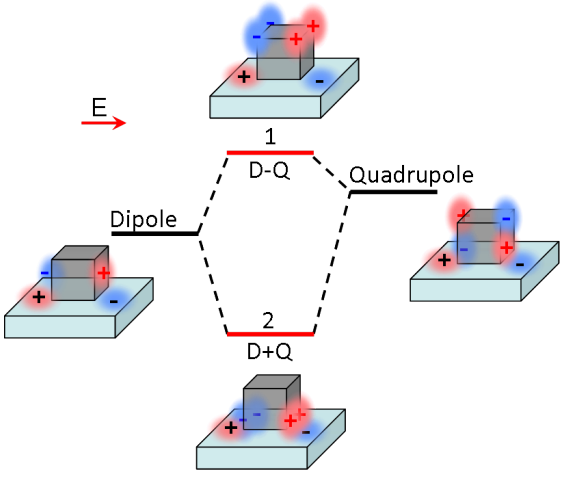

Figure 2.19: Schematic showing the substrate mediated hybridisation of a dipolar and quadrupolar mode resulting in anti-bonding (1) and bonding (2) hybridised modes(adapted from [94]).

2.8 Measurements of the Spectra of Single Silver Nanocubes and Linearly Organised Nanocube Clusters

Silver nanocubes and nanocube clusters are of interest for many applications, in particular for sensing applications such as SERS [90], since the sharp corners of the cubes give rise to intense 'hot spots' of electric field enhancement [91]. When nanocubes are present on a substrate, two peaks are often seen in the spectra. These two peaks are due to a Fano resonance caused by the hybridization of a dipolar and a quadrupolar mode as shown in figure 2.19. One peak is due to a resonance where the electric field is preferentially enhanced away from the substrate (D-Q) and one where the electric field is preferentially enhanced towards the substrate (D+Q) [92; 93]. The hybridization is mediated by image charges which form in the substrate. The magnitude of the induced charges depends on the permittivity of the substrate so the Fano resonance is stronger the higher the permittivity of the substrate [94]. A further effect that has been seen in silver nanocube dimers is splitting of the main dipolar resonance which occurs when the corners of the cubes are rounded [95]. Interaction between nanocubes and high index substrates such as silicon can result in completely different behaviour of nanoparticles compared to their isolated responses [96]. Using the hyperspectral imaging system it is possible to measure an array of nanocube clusters on a silicon substrate to acquire scattering spectra of a number of individual clusters or individual nanocubes.

2.8.1 Experimental Methods

Scattering spectra were measured in the hyperspectral darkfield set-up as previously described. For the polarisation measurements, a polariser was placed in front of the

CCD camera which was rotated between images. The SEM images of the nanocube clusters were taken in a Karl Zeiss Leo SEM after the hyperspectral measurements in case any damage to the sample was caused by the electron beam of the SEM.

The silver nanocubes were produced by O. Rabin et al, according to the method described in [97]. The nanocubes were then deposited onto a silicon substrate to from a nanocube array, which was produced by the same group according to the method described in [98].

2.8.2 Results

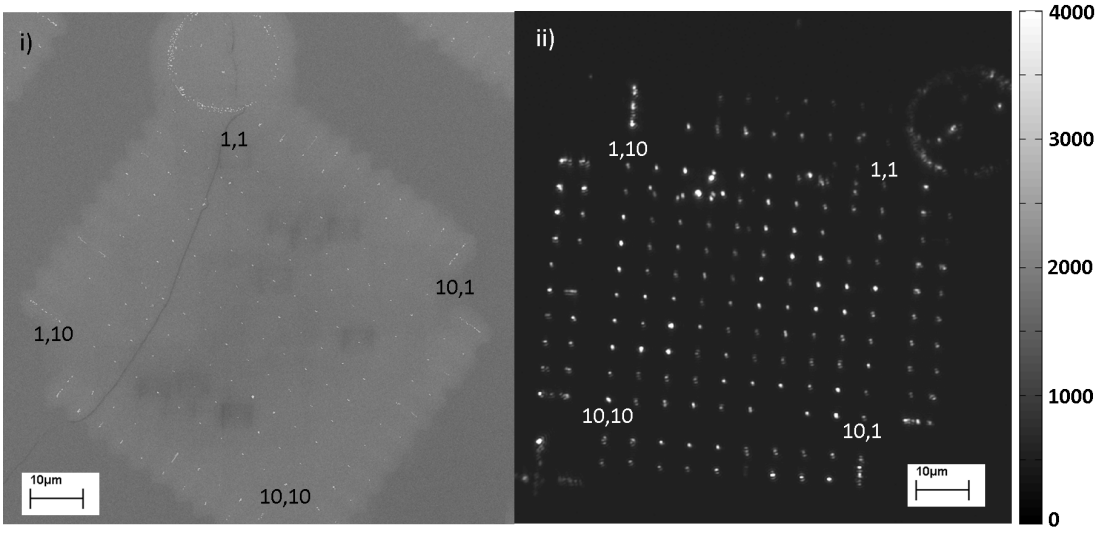

Figure 2.20: i)SEM and ii)darkfield images showing an array of nanocube clusters, with labels showing the system of naming the individual clusters in the array used in subsequent images.

Figure 2.20 shows a comparison of darkfield and SEM images of the array of nanocube clusters. The clusters in the array have between 1 and 4 nanocubes per cluster. In most of the clusters, the nanocubes are aligned in a line, with varying gap distances between the nanocubes in the cluster.

Single Nanocubes

Figure 2.21 shows a polarisation plot for a single silver nanocube from position 1,6 of the array along with scattering spectra and an SEM image of the particle. The scattering spectra show a resonance at 698 nm $\pm$ 10 nm which does not seem to have a polarisation dependence.

Overall, the single nanocubes seem to show a weak polarisation dependence with a peak aligned with one of the straight axis of the cube.

Connected Dimers

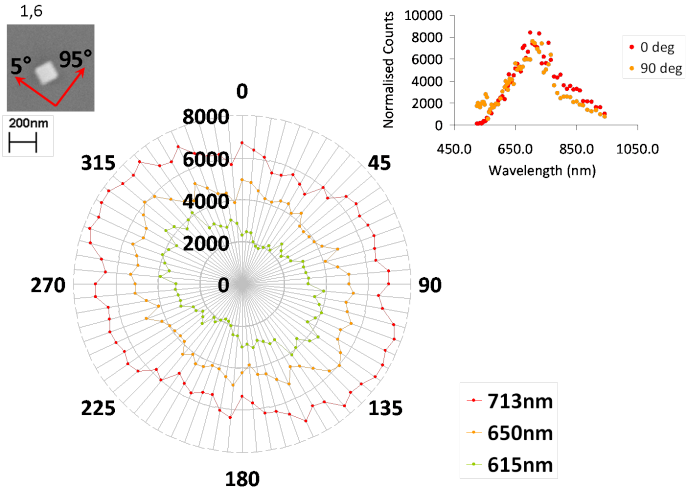

Figure 2.21: A polar plot showing scattering from the nanocube at different laser polarisations for three different wavelengths, shown with an SEM image of the nanocube and a plot showing the scattering spectra measured at two different polarisations

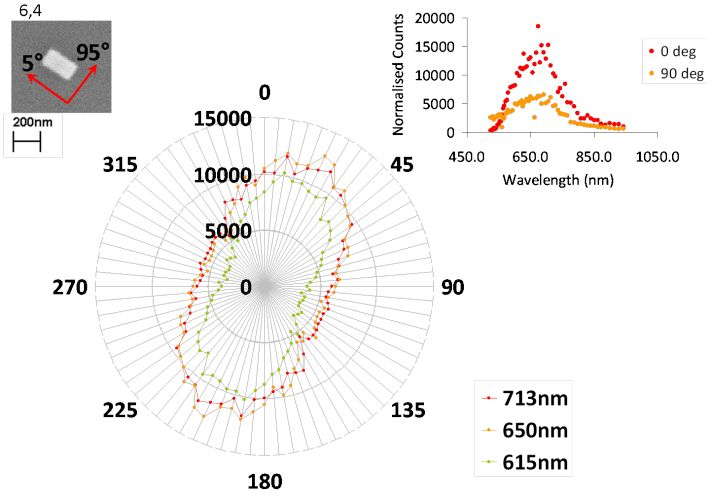

Figure 2.22: A polar plot showing scattering from the nanocube dimer in position 6,4 shown with an SEM image and a plot showing the scattering spectra

The connected dimers seem to show a strong polarisation dependence, with a maximum along the straight axis of the particle dimer. This effect can be seen in figures 2.22 and 2.23.

Separated Dimers

Figure 2.24 shows a polarisation plot for a silver nanocube dimer from position 9,4 of the array along with scattering spectra and SEM image of the particle. The scattering spectra show a resonance at 706 nm ± 10 nm but the scattering from the nanoparticles

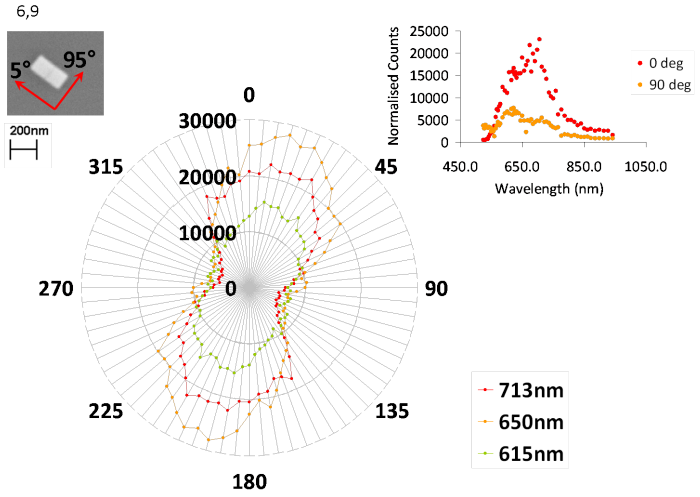

Figure 2.23: A polar plot showing scattering from the nanocube dimer in position 6,9 shown with an SEM image and a plot showing the scattering spectra

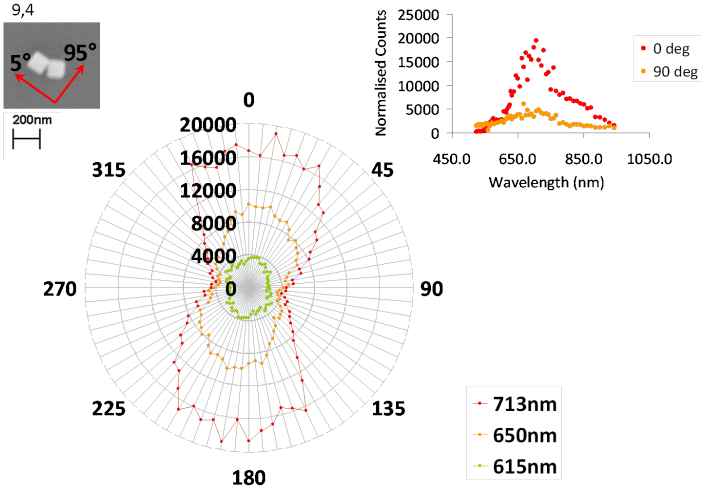

Figure 2.24: A polar plot showing scattering from the nanocube dimer in position 9,4 shown with an SEM image and a plot showing the scattering spectra

is much stronger when the polarisaton of the laser is aligned with the direction of the long axis of the nanocube dimer.

Figures 2.25 and 2.26 show the polar plots and scattering spectra for nanocube dimers with a larger spacing between the two cubes in the dimer than those shown in figures 2.22 - 2.24. The polarisation dependence seen for the closely spaced dimers is not seen in this case and the resonance present in the scattering spectra is seen to blueshift to around 650 nm. A weak second peak is also seen in the scattering spectra at 850 nm, which is more pronounced when the polarisation is aligned with the long axis of the nanocube dimer for both dimers.

Overall, the peak seen at 650 nm does not seem to show a large polarisation anisotropy.

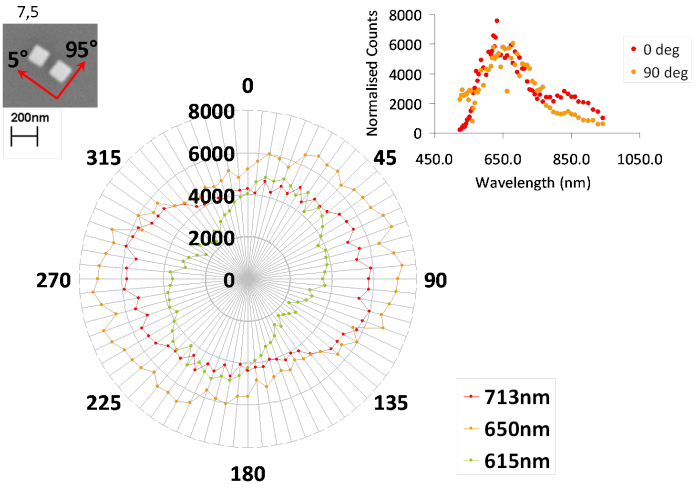

Figure 2.25: A polar plot showing scattering from the nanocube dimer in position 7,5 shown with an SEM image and a plot showing the scattering spectra

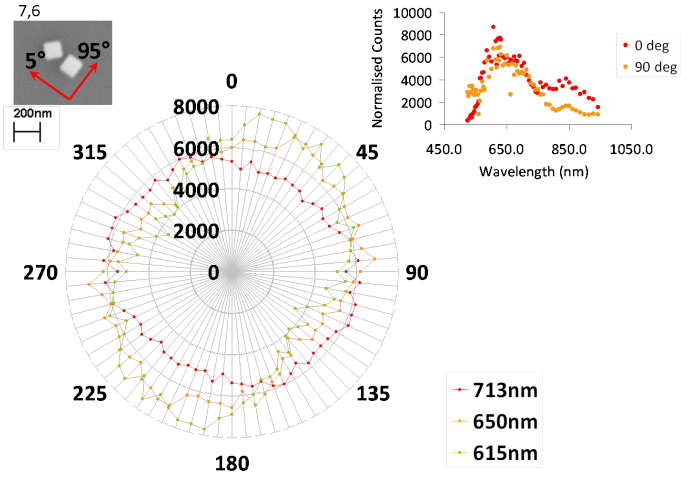

Figure 2.26: A polar plot showing scattering from the nanocube dimer in position 7,6 at different laser polarisations for three different wavelengths, shown with an SEM image of the nanocube and a plot showing the scattering spectra measured at two different polarisations

There seems to be a secondary feature at 850 nm for all the separated dimers with a maximum along the alignment axis. This feature is also seen for pairs of nanocubes which are slightly rotated with respect to each other, such as in figure 2.26.

Trimers

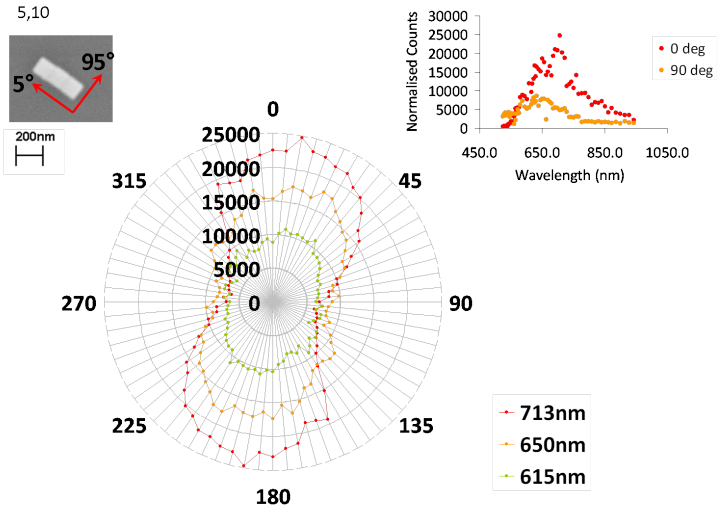

Figure 2.27: A polar plot showing scattering from the nanocube trimer in position 5,10 at different laser polarisations for three different wavelengths, shown with an SEM image of the nanocube and a plot showing the scattering spectra measured at two different polarisations

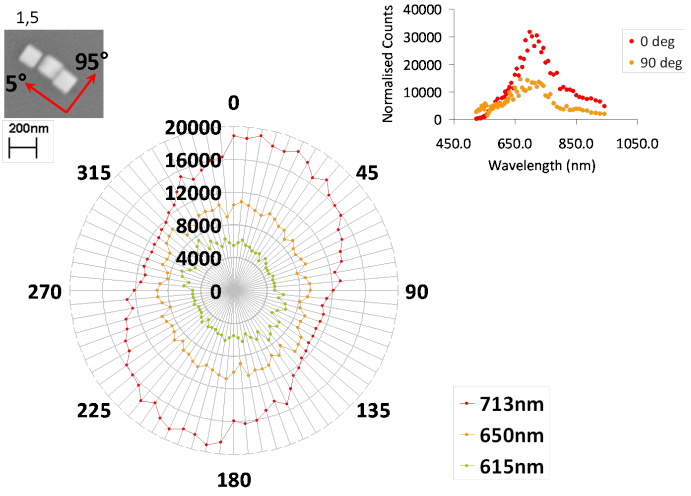

Figure 2.28: A polar plot showing scattering from the nanocube trimer in position 1,5 at different laser polarisations for three different wavelengths, shown with an SEM image of the nanocube and a plot showing the scattering spectra measured at two different polarisations

For closely spaced trimers in the array such as 5,10 shown in figure 2.27 a similar result is seen as for the closely spaced dimers. More scattering from the trimer is seen when the polarisation of the laser is aligned with the long axis of the trimer. A difference between the closely spaced trimer and the closely spaced dimers is that for the trimer a bigger shift in the resonance is seen between the two different polarisations at which the full spectrum has been measured. For trimers with a larger spacing between the nanocubes,

less of a polarisation dependence is seen as shown in figure 2.28. The trimers seem to show similar responses to the dimers in that polarisation dependence is weaker when the nanocubes are spaced farther apart.

Tetramer

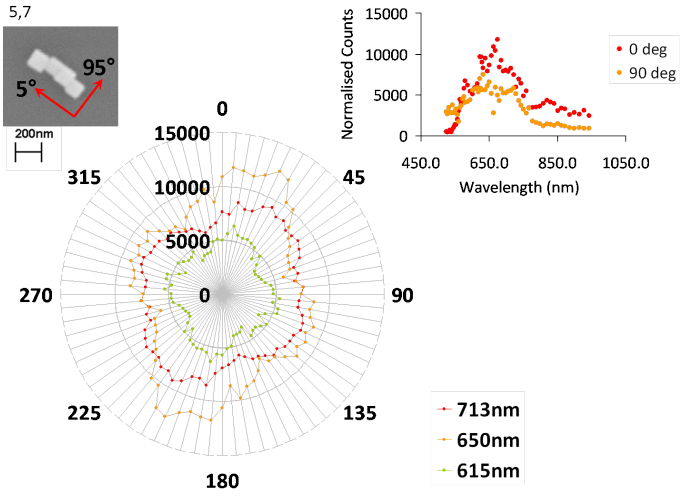

Figure 2.29: A polar plot showing scattering from the nanocube tetramer in position 5,7 at different laser polarisations for three different wavelengths, shown with an SEM image of the nanocube and a plot showing the scattering spectra measured at two different polarisations

Figure 2.29 shows a nanocube tetramer. For light polarised in the direction of the long axis of the tetramer, A peak in the spectrum is seen at 674 nm ± 10 nm and a further shoulder is seen at 819 nm ± 10 nm. For light polarised in the direction of the short axis of the tetramer, a peak is seen at 632 nm ± 10 nm with a shoulder at 721 nm ± 10 nm. The nanocube tetramer exhibits a complex polarisation response, which could be due to the horizontal misalignment of the cubes relative to each other.

2.8.3 Discussion

Overall, the system of nanocube clusters on silicon with various orientations of and spacings between the nanocubes in each cluster is complicated as there are many parameters involved which affect the resonances of such a system. The hyperspectral darkfield system is particularly useful for cases like this where it is desirable to know where the plasmon resonances are for particular individual cluster which may be used for SERS, for example, but where it may be difficult to predict what the plasmon resoanances might be without modelling each individual cluster. As can be seen from the results above, small changes in parameters such as gap spacing appear to have an effect on the polarisation of the resonances and on the peak positions.

From a comparison of the measured results with those found in [94] and [92] it appears that the resonance measured for the single cube is the lowest energy mode (the D+Q hybridised mode), in which the field is strongest towards the substrate. For the dimers, the result is in agreement with [95], that is, a stronger peak is seen in the visible for the interparticle axis and a weaker peak is seen for the perpendicular axis. However, the pronounced redshift observed in [95] was not seen. This difference could be caused by an interaction with the substrate, which has already produced a strong redshift in the single particle case.

2.9 Conclusions

In this chapter, the hyperspectral darkfield microscopy method has been shown to be successful for imaging of and performing spectral measurements on gold nanoparticles. A bespoke darkfield microscope has been built which enables darkfield imaging over a range of near IR and visible wavelengths through the use of a supercontinuum laser and an acousto-optic tuneable filter. Automated wavelength scans can be performed and therefore spectral information can be aquired covering the whole field of view of the darkfield microscope simultaneously, as opposed to a point by point method. The hyperspectral darkfield method has been used to meaure both the transverse and longitudinal LSPR peaks of an array of lithographically produced nanoantennas. The system has also been used to measure spectra of single colloidal nanorods and to measure the spectra of colloidal hollow gold nanoparticles, which have also been imaged in a TEM in order to correlate data aquired from these two imaging systems. In addition, the hyperspectral darkfield system has been used to measure the scattering spectra and polarisation dependence of individual silver nanocubes and silver nanocube clusters, which have also been imaged in an SEM to correlate the measured spectra to particular clusters.

Overall the hyperspectral darkfield imaging system has been shown to be a useful tool for imaging of gold and silver nanoparticles on a substrate. Individual nanoparticles can be detected as long as they are separated spatially from each other by at least 300 nm. The sensitivity of the darkfield microscope has also been demonstrated - the smallest nanoparticles detected individually using this system have been the gold nanorods of length 47 nm, diameter 16 nm. Gold nanoparticles larger than this can be imaged using the hyperspectral imaging system and spectra of the particles can also be measured.

The results in this chapter also demonstrate the limitations of this method. The spectra measured are not as precise as those which can be measured using other spectroscopy methods, for example spatial modulation microscopy or conventional broadband darkfield spectroscopy using a grating spectrometer, but the advantage of the hyperspectral darkfield technique is that spectra of multiple nanoparticles can be measured simultaneously.

In applications requiring spectral measurements of nanoparticles, the hyperspectral darkfield method could be useful as a method both to view the nanoparticles on the substrate (a non-trivial problem when the nanoparticles are below the diffraction limit of optical brightfield microscopes) and to perform a preliminary spectral measurement of an area of the sample of order $100 \times 100\mu$m from which particular nanoparticles of interest could be defined for further, more precise spectral measurements on select individual particles or clusters.

In the next chapter the development of the darkfield microscopy technique for imaging the interactions between nanoparticles and cells will be discussed.

Chapter 3

Darkfield Microscopy for Detection of Gold Nanoparticles in Cells

In this chapter, the use of darkfield microscopy for the detection of gold nanoparticles inside cells is discussed. It is possible to use darkfield microscopy for the detection of metallic nanoparticles on a cellular background [24; 99], since due to their plasmonic properties, nanoparticles with dimensions over 50 nm scatter light strongly at a particular resonant wavelength compared to any background scattering from cells.

The purpose of developing the darkfield detection method described here is to demonstrate the detection of plasmonic nanoparticles on a cellular background and to show how the positions of nanoparticles inside cells can be identified using this method. A further advantage of using darkfield microscopy as a method for detecting nanoparticles in cells is that due to the short exposure times of between 0.01 and 0.2 seconds needed to collect darkfield images, it is possible to image in real time using this method, which means that live cell imaging is possible.

3.1 Detection of Gold Nanorods in Fixed Dendritic Cells using Darkfield Microscopy

In this project, the method of using darkfield microscopy to detect plasmonic nanoparticles inside cells has firstly been demonstrated using fixed dendritic cell samples. Dendritic cells have been grown and then incubated with gold nanorods with a known plasmon resonance at 705 nm. The home built darkfield microscope set up described in chapter 3 has been used, which allows darkfield images to be aquired at different

wavelengths of light ranging from 500 to 900 nm, easily covering the longitudinal plasmon resonance of the nanorods. The presence of nanoparticles in a sample of dendritic cells has been confirmed by comparing the amount of scattered light from a cell sample that has been incubated with nanoparticles to the signal from a control sample of cells without nanoparticles.

3.1.1 Cell Preparation Methods

Dendritic cell (DC 2.4 cell line) samples have been produced by H. Warren (University of Southampton, Physics and Astronomy) and N. Fairbairn with the help of R. Carter (University of Southampton, School of Medicine).

Different samples were produced as follows: $1x10^5$ DC 2.4 dendritic cells were added to each well of a 12-well microplate, each containing a coverslip and incubated for 24 hours in standard growth medium at 37°C. Nanoparticle solution (40 µl, 20 µl of concentration with longitudinal extinction peak with an optical density of 2.5), produced by R. Fernandes (University of Southampton, Physics and Astronomy) was then added to the relevant wells and centifuged together with the cell solution(1-2 mins, 250 rpm), The samples were then incubated in standard growth medium at 37°C for periods of 1 hour and 2 hours. A control sample of cells without nanoparticles was also produced. The coverslips were then washed in PBS, fixed in paraformaldehyde for 7 mins and washed again in PBS. Slides were prepared by gluing coverslips to glass slides with moviol.

3.1.2 Results

Figure 3.1 shows dendritic cells that have been incubated with gold nanorods and a control sample of cells without nanorods. It can be clearly seen that the sample which gives the highest signal under the darkfield microscope is the sample with 40 µl of nanorod solution incubated for 2 hrs, at a wavelength of 691 nm. This wavelength is within the longitudinal plasmon resonance peak of the nanorods, as can be seen from figure 3.2, an extinction spectrum measured by R. Fernandes. This evidence strongly suggests that the increased signal from this sample is due to the presence of nanoparticles.

The spatial distribution of the detected scattering signal suggests that the nanoparticles may be mainly located around the edges of the cell and it is likely that they have been uptaken in the endosomes of the cell. This experiment is mainly a test of whether the home built darkfield microscope would be able to detect the scattering signal of the nanorods on top of a cellular background, so for this purpose it is sufficient that the nanoparticles are present and concentrated at the position of the cells.

Figure 3.1 shows an increase in signal for cells that have been incubated for a longer time. This result suggests that there is some uptake of, or interaction between, the

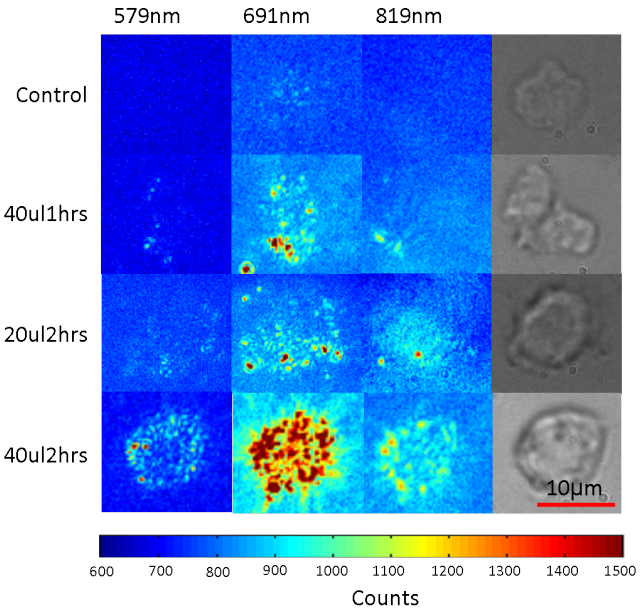

Figure 3.1: Summary of darkfield images from samples of cells incubated with different amounts of nanoparticles for different lengths of time. A brightfield image of each cell is also shown.

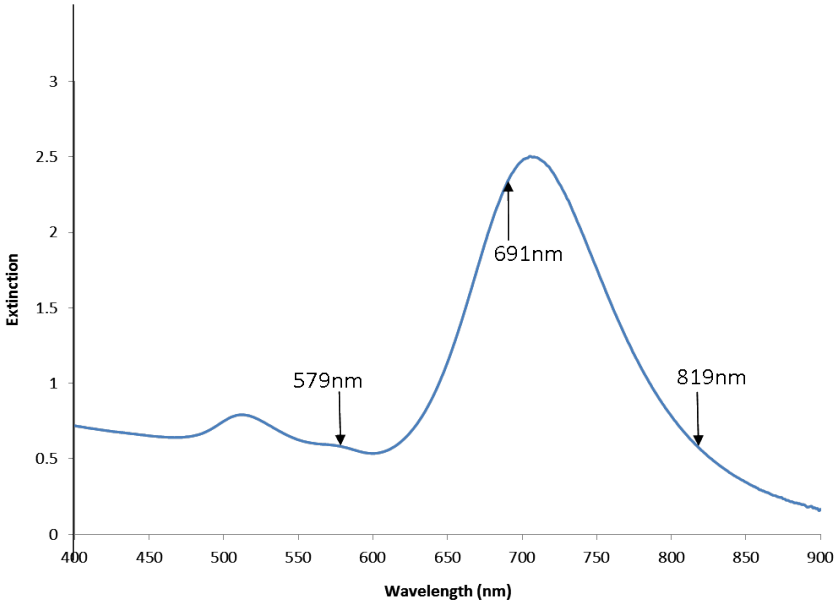

Figure 3.2: Extinction spectrum of gold nanorod solution used in these experiments, measured by R. Fernandes by UV-Vis spectrometry.

nanoparticles and the cells, since the cells are washed after incubation with nanoparticles so any nanoparticles that are not attached to, or inside the cells should be washed away. A higher signal is found at all wavelengths when more nanoparticles are present in the sample. This effect could be due to a broadening of the plasmon resonance peak due to some aggregation of the nanorods as they are collected in the endosomes of the cells.

The darkfield microscope has a wavelength dependent sensitivity, with a maximun

around 730 nm. The darkfield images shown in figure 3.1 are the original measured images so the wavelength dependence of the system has not been corrected for. To verify that the signal observed in fig 3.1 is due to nanoparticles, the mean value of light scattered over the total area of each cell is shown for different wavelengths, corrected for system efficiency, in figure 3.3. In the absence of nanoparticles, a flat response is seen. Where nanoparticles are present, a clear peak is observed.

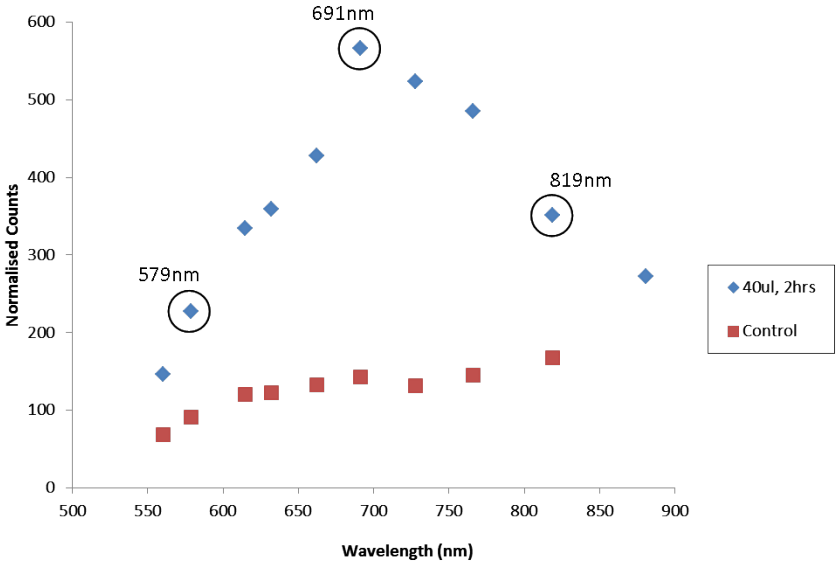

Figure 3.3: Normalised values of scattered light from sample, measured at camera, for sample containing 40 µl of nanoparticles, incubated with cells for 2hrs, and a control cell sample.

Overall, the darkfield microscopy method seems to be successful at enabling detection of gold nanorods in a cellular environment as long as certain conditions are satisfied. Specifically, when the wavelength of light is at the plasmon resonance of the nanoparticles, when the concentration of nanorods is high enough, and the incubation time is long enough to allow the nanoparticles to attach to, or be taken up by the cells.

3.2 Three dimensional Cell Imaging

The darkfield microscopy images shown in the previous section can only be used to localise the position of the nanoparticle in the XY plane. From these images it is difficult to tell the difference between whether the nanoparticle has been internalised in the cell, is attached to the surface, or is positioned some distance above or below the cell in the image. It can be seen that the nanoparticle and the cell have the same position in the Z plane by seeing that they come into focus at the same point. However, whilst the nanoparticle is a point like object with a clear focus, the cell is more spread through the Z direction, so as the focus is changed, different parts of the cell go in and out of focus.

Because of this effect, it can be difficult to use two dimensional images of cells with nanoparticles to localise the position of any nanoparticles inside the cell. Therefore, a method of visualising this information in a three dimensional image has been developed, by building up 3D images from 2D slices that are taken at different Z positions through the sample.

3.2.1 Experimental Methods

The same home built darkfield set up described previously has been used to take the 2D images which make up the slices of the final 3D image. In order to produce the 3D scans, the sample is mounted on a piezo stage, with a computer controlled scan range of 20 μm in the Z direction. The stage is used to scan the sample through the focus of the microscope objective and a 2D image is collected every 0.5 μm. A Matlab program is used to convert the 2D images into a 3D array, in a format which can be opened with the visualisation program MayaVi. In order to reduce the out of focus light from each 2D slice, it can also be useful to differentiate each 2D image in the X or Y direction so that only the sharper parts of the 2D image contribute to the 3D image. The image differentiation was performed using a Matlab program. The effect can be seen in figure 3.4 which shows colloidal nanorods which have been deposited on a TEM grid and nanoantennas fabricated with e-beam lithography on an ITO coated glass substrate.

3.2.2 Results

In order to demonstrate the depth of focus of the darkfield system, a 3D image array of nanoantennas (fabricated by M. Abb) is shown in figure 3.5. The nanoantennas are positioned on the surface of a glass slide, so they all have the same position in the Z direction. From figure 3.5 it can be seen that the resolution of the Z position of the nanoantennas is approximately 2 μm, which is the FWHM of a crossection taken through an antenna, shown in figure 3.6.

Figure 3.6 shows a cross section through the 2D slices in the Z direction. The two lines on the graph show the intensity change with Z position for 2D slices which have been differentiated in the x direction and undifferentiated slices. From this graph it can be seen that image differentiation gives a slightly sharper focus than using undifferentiated images. For the nanoantenna image only a slight difference is seen between differentiated and undifferentiated images because the antennas are on a glass substrate with minimal background scattering so the undifferentiated image is already very sharp. However, the antenna example adequately demonstrates the limits of 3D localisation of nanoparticles using the method described here.

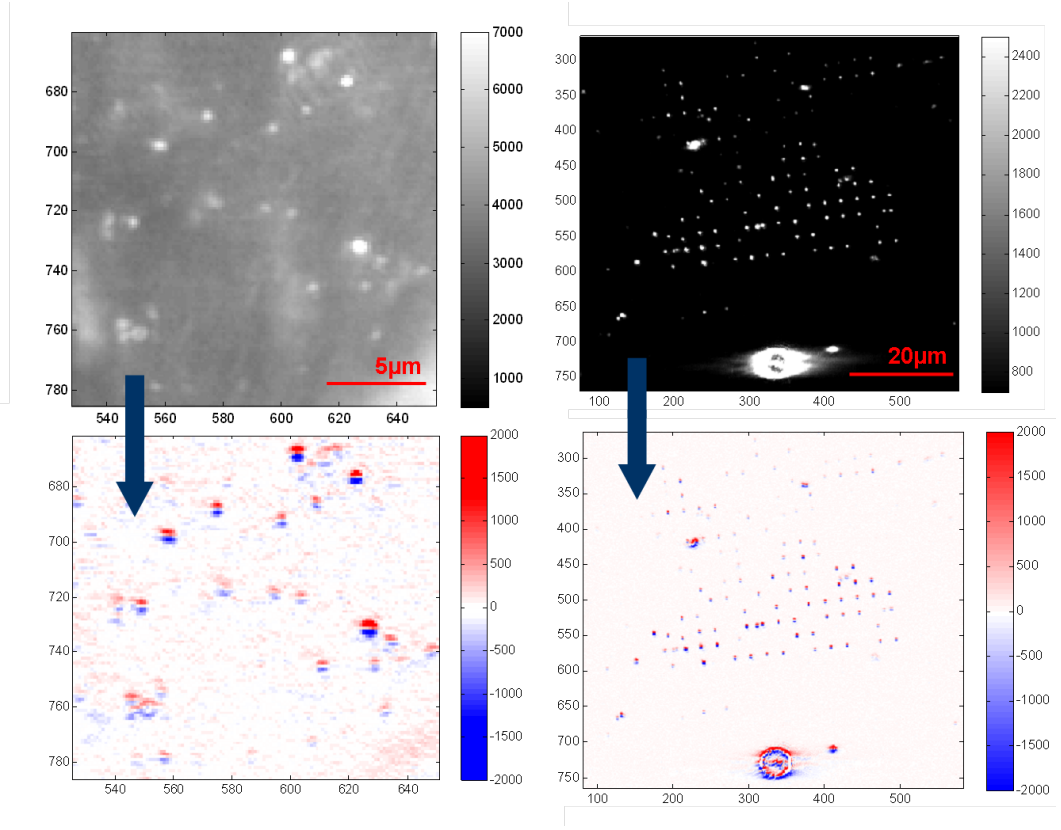

Figure 3.4: Images of colloidal nanorods (i) and an array of nanoantennas with a contamination spot (ii), before and after differentiation

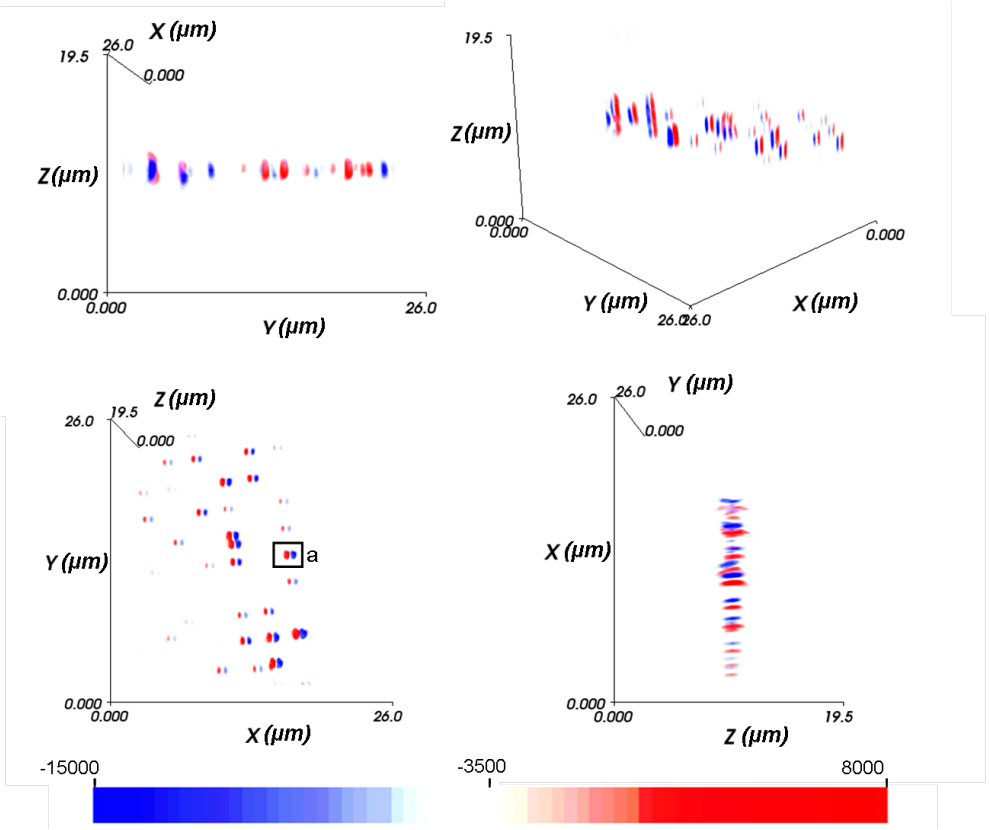

Figure 3.5: 3D image of nanoantennas shown at different angles

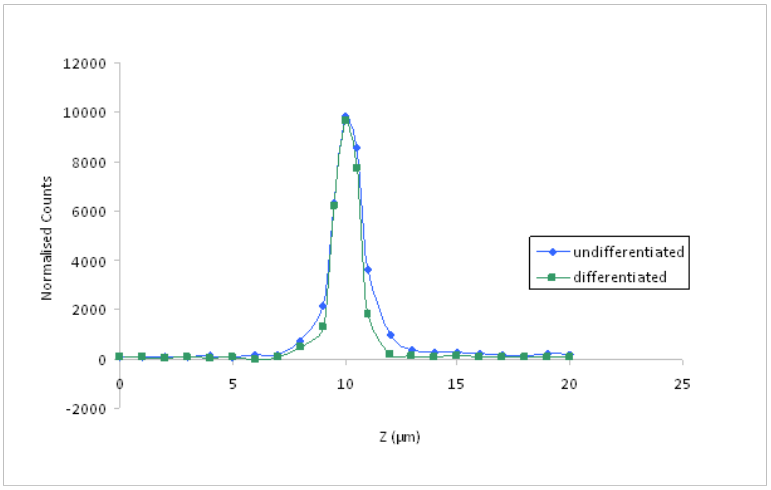

Figure 3.6: cross section of antenna a for differentiated and undifferentiated images

A dendritic cell sample, incubated with gold nanorods as described in chapter 3 has also been imaged using the 3D imaging technique described above. Figure 3.7 shows four 2D slices that are part of the series of slices used to build the 3D image of the cell. For these images an alternative method has been used to minimise background light. The images have been recorded at two different darkfield wavelengths. Firstly at 713 nm, which is on resonance for the nanorods, and also at 650 nm, which is off resonance. To normalise the images, the off resonance image is subtracted from the on resonance image (the variation in laser power at different wavelengths is also accounted for). The normalised darkfield image is then added to the brightfield image so that the position of the cell can be seen as well as the nanorods, since the cell is hardly visible in darkfield. The reason for performing the normalisation is to try and reduce light which is not due to scattering from nanoparticles in the image.

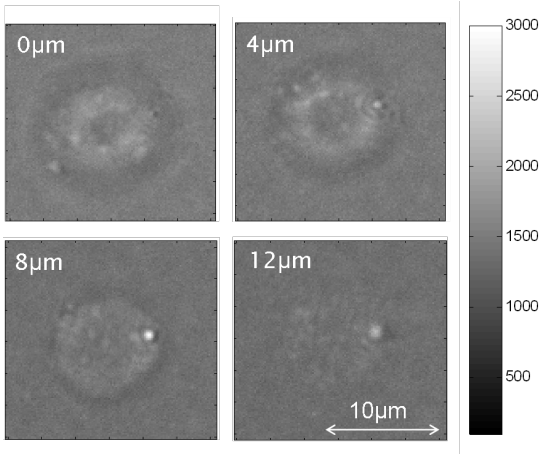

Figure 3.7: 2D slices of a dendritic cell incubated with gold nanorods, taken at different Z positions

The 2D slices are then stacked to form a 3D image. The 3D image of the dendritic cell shown in figure 3.7 is shown from different angles in figure 3.8.

From figure 3.8 it is possible to clearly see the Z position of the bright nanoparticle cluster (which can be seen as a red spot in the image), whilst a 2D image can only show the X and Y position. The 3D imaging technique is useful to show the position of nanoparticles relative to a cell. The technique can be used to confirm that nanoparticles have truly been internalised inside a cell or to see if nanoparticles are, for example, attached to the surface of a cell.

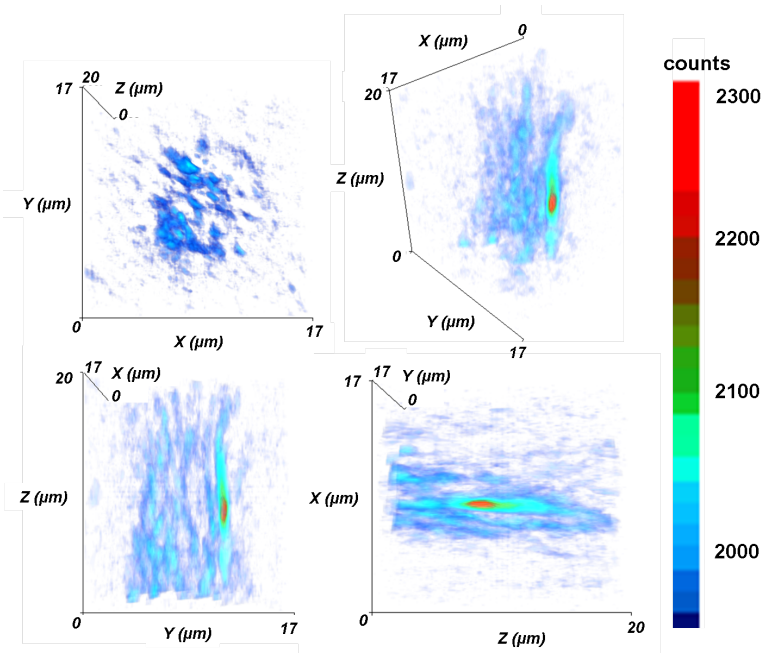

Figure 3.8: 3D image of a dendritic cell incubated with gold nanorods shown from different angles

3.3 Imaging of Fibroblast Cells

The darkfield imaging system has been shown to be useful in imaging cells and for detecting the presence of nanoparticles in a sample of cells. However, in order to improve the imaging system further, an additional 405 nm laser was added to the set up in order to take fluorescence images of cells.

Fixed fibroblast cells (cell line L929) have been imaged using the darkfield imaging system. The clarity of the images has been improved by using a fluorescent dye (DAPI) with an emmision maximum at 461 nm, to stain the nuclei of the cells and the experimental set up has been modified in order to enable fluorescence images of the cells to be taken as well as brightfield and darkfield images. The Fluorescent dye was excited with a 405 nm laser which is coupled into the microscope objective using a dichroic mirror. A fluorescence filter was also placed in front of the CCD camera in order to detect only the light which is emitted by the fluorescent dye and to cut out light from the 405 nm laser.

A sample of cells which were incubated with 100 µl of gold nanorod solution which had an optical density of 1, coated with HS-PEG-COOH for 6hrs and a control sample of cells that were prepared in the same manner except for the inclusion of nanoparticles were compared. Both samples were prepared by A. Christofidou (University of Southampton).

Figure 3.9 shows brightfield, fluorescence and darkfield images of a sample of cells incubated with nanorods for 6hrs. In the fluorescence image, the nuclei of the cells can be

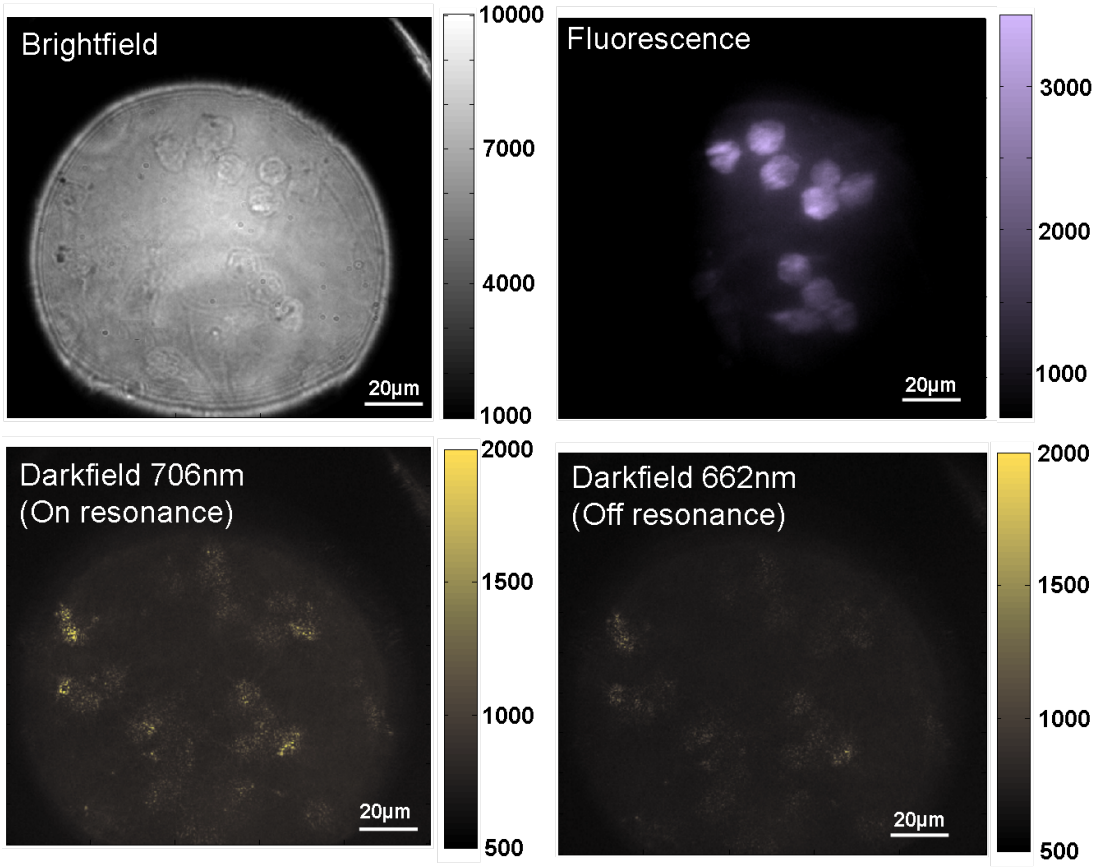

Figure 3.9: Brightfield, fluorescence and darkfield images of a sample of cells that has been incubated with gold nanorods for 6hrs. Darkfield images are shown for two different wavelengths, 706 nm which is close to the resonance of the nanorods, and 662 nm which is off resonance.

seen as these have been stained with DAPI. More scattering is seen on the darkfield image measured at 706 nm than on the darkfield image measured at 662 nm. This increase in scattering close to the expected LSPR of the nanoparticles is an indication of the presence of nanoparticles in the cells. The images shown in figure 3.9 are uncalibrated images so the wavelngth dependant sensitivity of the system has not been taken into account. Calibrated data from the same images is shown in figure **??**.

In order to verfy that the increase in scattering is due to the nanoparticles rather than just scattering from the cells, spectra were measured of small areas of the cell, using the hyperspectral darkfield imaging system described in chapter 3.

From the spectra shown in figures 3.10 and 3.11 it can be seen that the spectra of the scattered light from the sample of cells that has been incubated with the nanoparticles for 6hrs are typical nanoparticle spectra with peaks that are close to the expected LSPR of the nanoparticles which is at 705 nm. The spectra of scattered light from the control sample, on the other hand, do not show any obvious peaks and the intensity of light

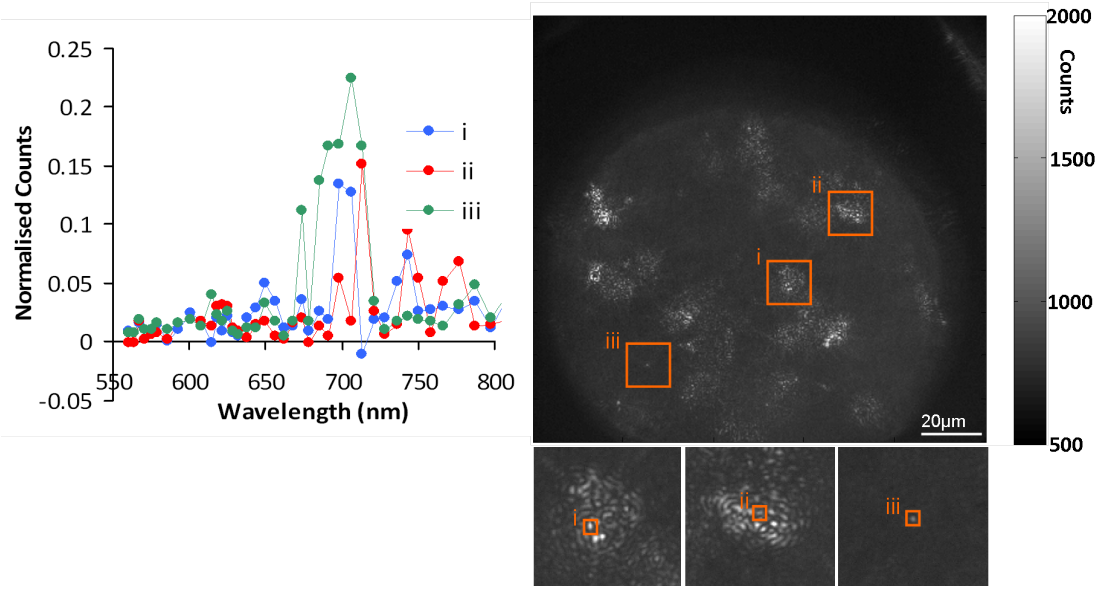

Figure 3.10: Spectra of areas of scattering in cells that have been incubated with gold nanorods. Areas a, b, and c on the full darkfield image correspond to the close up images a, b and c Spectra of bright spots i, ii and iii are shown

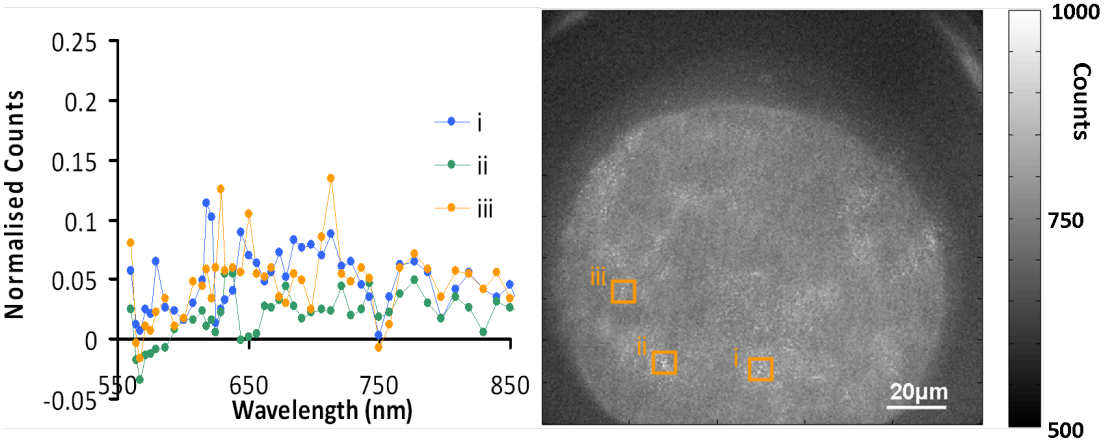

Figure 3.11: Spectra of areas of scattering in a control sample of cells. Areas a, b, and c on the full darkfield image correspond to the close up images a, b and c Spectra of bright spots i, ii and iii are shown

scattered from the sample is also lower, as can be seen in the difference in normalised counts between the two samples.

3.4 Imaging of SHSY-5Y Cells

Nanoparticles hold great potential for use in neuroscience as they have the potential to cross the blood brain barrier [25; 26]. The blood brain barrier refers to the tight junctions around capilliaries that separate the blood from the extra cellular fluid in the central

nervous system. These tight junctions do not exist elsewhere in the circulatory system and they make it extremely difficult to deliver drugs to the central nervous system. Since nanoparticles have the potential to deliver drugs across the blood brain barrier there is a lot of interest in studying the way they interact with the cells of the central nervous system.

In addition, the impact of exposing the nervous system to nanoparticles should be assesed [100], since the nervous system could come into contact with nanoparticles by multiple delivery pathways due to its spatial distribution within the body and close proximity to nanoparticle exposure sites such as skin. The ease with which nanoparticles enter a cell and the degree of clustering of nanoparticles inside the cell can depend on the type of nanoparticle coating. The TET-1 peptide specifically binds to the trisialoganglioside clostridial toxin receptor on neurons, possibly promoting a receptor-mediated endocytosis [101].

In order to further understand the interactions of these TET-1 coated nanoparticles with cells of the central nervous system a series of experiments have been conducted using darkfield microscopy to image the nanoparticles, and brightfield and fluorescence microscopy to image the cells. The information from the three images has been combined to identify the position of the nanoparticles relative to the cell. Spectra of the nanoparticles have also been measured using the hyperspectral darkfield technique.

SHSY-5Y cells are a cell line which is originally derived from human neuroblastoma cells. In this experiment SHSY-5Y cells have been incubated with hollow gold nanoparticles coated with TET-1 peptide for incubation times of 1hr and 2hrs. A control sample without nanoparticles has also been produced. SHSY-5Y cell samples were prepared by A. Christofidou.

Figure 3.12 shows images of a cell that has been incubated with nanoparticles for 2hrs. The original darkfield image is shown, along with a combined false colour image showing brightfield, darkfield and fluorescence (darkfield shown in red, fluorescence shown in blue). The fluorescence image was achieved by staining the nuclei of the cells with DAPI and exciting the dye with a 405 nm wavelength laser. Spectra were also measured for different parts of the cell using the hyperspectral darkfield system described previously. The purpose of measuring spectra in this case was to try to identify if the bright spots observed in darkfield were due to nanoparticles or to scattering from the cell. All three of the spectra show peaks, suggesting the presence of nanoparticles. Spectra i and ii both show narrow peaks at 728 nm, which is close to the theoretically predicted peak for average sized hollow gold particles at 740 nm. Peak ii is twice as high as peaks i and iii which are of a similar height, which may suggest that i and iii are single nanoparticles.

Figure 3.13 shows images of a cell from the sample which has been incubated with nanoparticles for 1hr along with spectra. Spectra i, ii and iv show broad peaks with maxima around 700 nm, which is a blueshift from the expected hollow gold nanoparticle

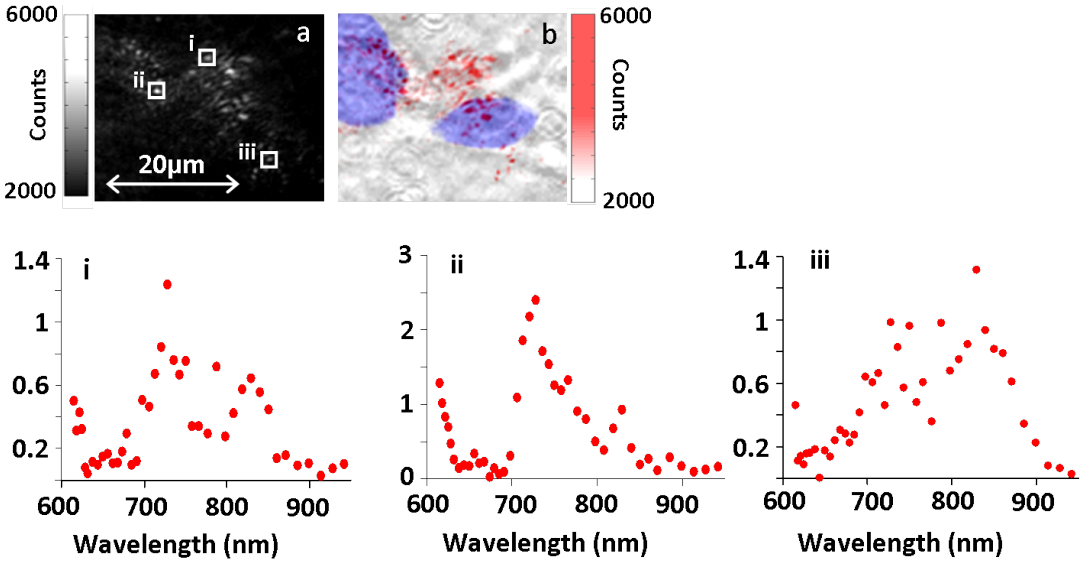

Figure 3.12: (a) A darkfield image and (b) a combined false colour image showing darkfield, fluorescence and brightfield image of a SHSY-5Y cell that has been incubated with hollow gold nanoparticles for 2hrs are shown along with spectra i - iii, taken from different bright spots indicated on (a)

resonance. Spectrum ii shows a spectrum with two peaks, which looks similar to the spectrum measured for a nanoparticle trimer shown in chapter 2.

Figure 3.14 shows images of a cell from a control sample of SHSY-5Y cells which have not been incubated with nanoparticles. It can be seen that there are some bright spots observed when the cell is viewed in darkfield. These bright spots are due to light that has been scattered from the cell and can be differentiated from the nanoparticle signals, by the measured spectra. The spectra measured for the control cell do not show the characteristic peaks of nanoparticle resonances and the variation in intensity of light with wavelength is less for the control cell sample.

Overall the comparison of the three samples suggests that nanoparticles are not present in the control sample but are present in both the 1hr and 2hr incubation samples. It can be seen from the 2hr and 1hr incubation samples that the nanoparticles are interacting with the cell in some way as they are found along the outline of the nuclei in some instances. However it is difficult to say whether the nanoparticles are inside the cell or bound to the outside. It is also clear that some scattering is seen near to the cells which does not seem to be directly related to the cells. An example of this can be seen in the 1hr incubation image in the top right corner of the image. Spectrum iii is measured from this area and seems to be a nanoparticle spectrum rather than due to, for example, dust on the sample. The cells have been washed in order to remove any nanoparticles that are not directly bound to the cells but in this case it seems that not all of the nanoparticles have been succesfully removed from the substrate. Therefore some of the nanoparticles present on these samples could be attached to the substrate rather than

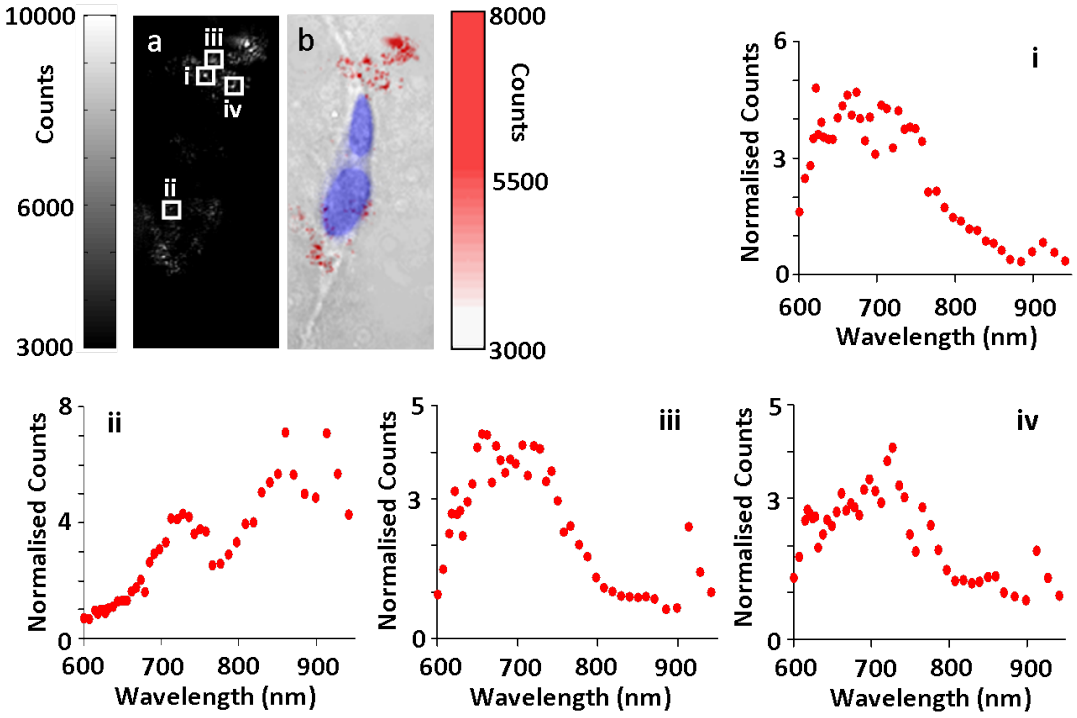

Figure 3.13: (a) A darkfield image and (b) a combined false colour image showing darkfield, fluorescence and brightfield image of a SHSY-5Y cell that has been incubated with hollow gold nanoparticles for 1hr are shown along with spectra i - iv, taken from different bright spots indicated on (a)

attached to or inside the cells. The way the nanoparticles seem to line up around the edges of the nuclei of the cells, however, suggests that these nanoparticles, at least, are interacting with the cells.

3.5 Real Time Darkfield Imaging

3.5.1 Real Time Imaging of Hollow Gold Nanoparticles in Solution

The exposure times required for darkfield imaging of nanoparticles and cells are fairly low (<1 sec), Therefore it is possible to perform real time imaging measurements. Real time darkfield imaging has been demonstrated on a solution of nanoparticles, where the motion of individual nanoparticles or nanoparticle clusters can be tracked. The darkfield microscope was set up as described in chapter 2. The nanoparticles used were hollow gold nanospheres coated with OEG-HG005-COOH. A glass coverslip coated in poly-l-lysine was used as the base of the container which held the nanoparticle solution and the microscope was focused on the surface of the coverslip that was in the nanoparticle solution. The Labview program used to capture and save the darkfield images was modified to capture and save a series of frames one after the other. These frames were then combined using a Matlab program to produce a video. The exposure times used

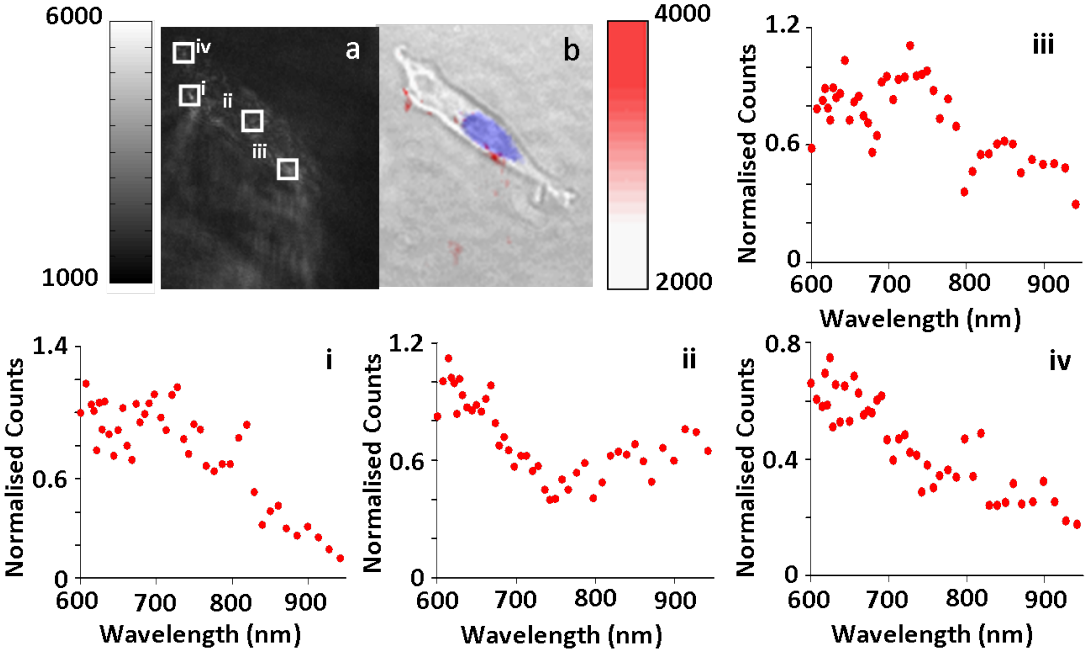

Figure 3.14: (a) A darkfield image and (b) a combined false colour image showing darkfield, fluorescence and brightfield image of a control SHSY-5Y cell that has not been incubated with hollow gold nanoparticles are shown along with spectra i - iv, taken from different bright spots indicated on (a)

for the individual frames were 0.01 to 0.1 seconds. However, the time taken to save each image with the Labview program had the effect of slowing down the frame rate to between 1.4 and 1.9 frames per second, for exposure times between 0.01 and 0.1 seconds. The exposure time used for a particular video was chosen so as to collect enough light from the sample whilst avoiding over-exposure

An example of a few consecutive frames of a video are shown in figure 3.15. It can be seen that it is possible to track individual particles and clusters. A clear example of this can be seen by focusing on the bright spot indicated by the arrow in the first frame of figure 3.15 which moves around on the surface of the glass coverslip before sticking to the coverslip in frame 16. Nanoparticles and nanoparticle clusters that are higher up in the solution above the coverslip can also be recognised by the pattern of rings characteristic of a point like bright spot which is out of focus. These out of focus patterns could also be used to track the positions of the particles in the vertical direction although this step is outside the scope of this project.

3.5.2 Real Time Imaging of Cells and Nanoparticles

Real time imaging is a useful tool and one of the advantages of darkfield imaging over other nanoparticle imaging methods is that real time imaging is possible with darkfield [102], which would be difficult with, for example, a scanning imaging method. One

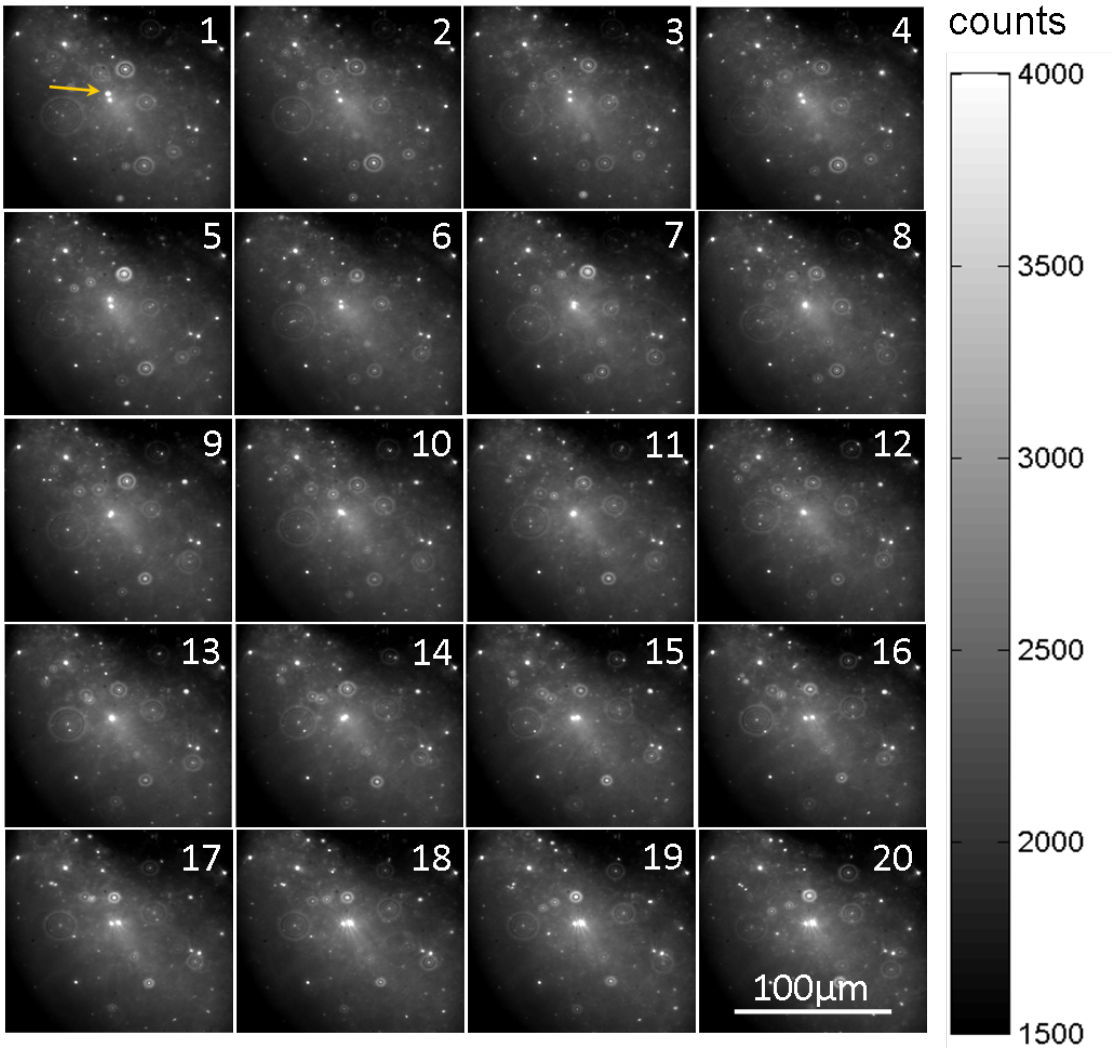

Figure 3.15: 20 consecutive frames, each taken with an exposure time of 0.1s (constituting a total capture time of 38 seconds) from a video of hollow gold nanoparticles in solution illuminated with a darkfield illumination at a wavelength of 728 nm

possible application of real time darkfield imaging is to study nanoparticle uptake by cells in real time. The real time videos of SHSY-5Y cells in the presence of nanoparticles have also been recorded using this system to demonstrate the potential for live cell darkfield imaging.

The SHSY-5Y cells were grown as described in section 3.4 inside a purpose built chamber which fitted into the darkfield setup. 1ml of nanoparticles of concentration with an extinction peak with an optical density of 0.5 was added to the cells for 1hr and then the chamber was fully sealed and moved to the darkfield microscope for imaging. The temperature of the chamber was kept at 37.5 +/- 1 °C during the darkfield measurement by use of a temperature controller. The positions of the cells were verified with brightfield and fluorescence before recording the darkfield video.

An example of a short section of the video is shown frame by frame in figure 3.16. It can be seen from this figure that the nanoparticle follows a random walk path with a total path length of 47 µm in 20 frames with the furthest distance moved between two frames being 3.5 µm. It is clear that the imaging frame rate is fast enough to enable tracking of individual nanoparticles.

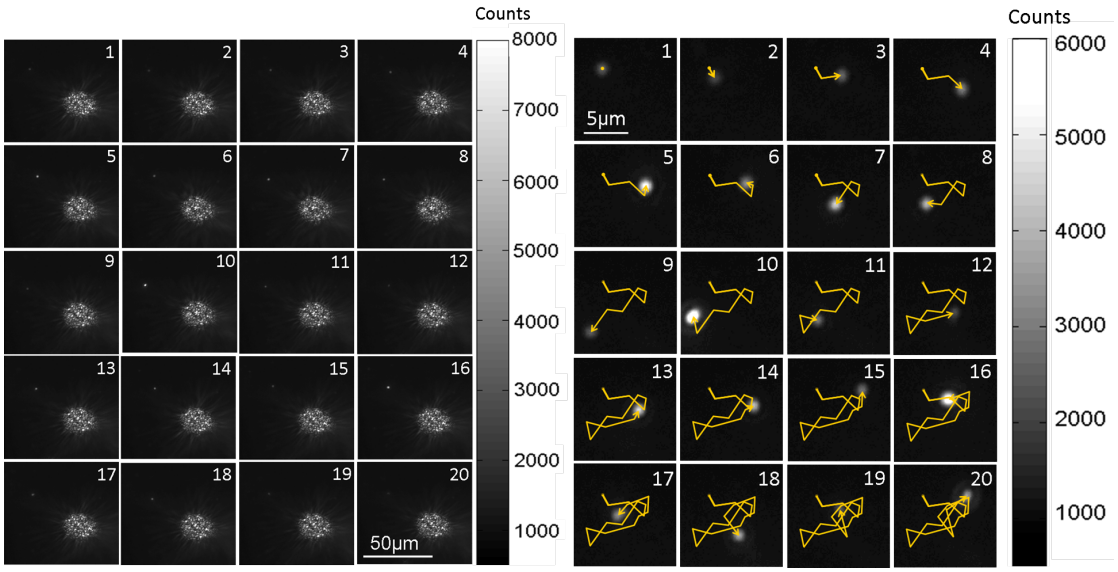

Figure 3.16: 20 consecutive frames taken at 0.01 s exposure time (constituting a total capture time of 28 seconds) showing a cell with nearby hollow gold nanoparticle along with close-up views of the nanoparticle, showing the path followed by the nanoparticle

3.6 Conclusions

In this chapter, the use of darkfield microscopy as a tool for imaging nanoparticles inside cells has been demonstrated. The wide ranging biomedical applications of nanoparticles mean that there is a high demand for methods of detecting nanoparticles on a cellular background, which can be achieved with darkfield microscopy.

The detection of CTAB coated gold nanorods in DC 2.4 cells was first demonstrated. The highest darkfield signal was seen for cells that had been incubated with the highest number of nanorods for the longest time (40 µl of OD 2.5 solution for 2hrs) when the cells were viewed in darkfield at the LSPR wavelength of the nanorods. The presence of nanorods was confirmed by measuring average spectra of light scattered from cells using the hyperspectral darkfield system. The difference seen between the control sample and the 40 µl 2hrs sample clearly indicated the presense of nanorods in the 40 µl 2hrs sample. The other samples, which contained nanoparticles at a lower concentration or where a shorter incubation time of 1hr was used also showed an increase in signal at the LSPR wavelength but to a lesser extent, suggesting that nanoparticles were also

present in these samples but not as many nanoparticles were present. The difference in signal from the nanoparticles seen for different incubation times indicates uptake of the nanoparticles over time by the cell which is to be expected for CTAB coated nanoparticles [103]. Overall this experiment showed that darkfield microscopy was a suitable choice for detecting the presence of nanoparticles inside cells.

One of the main disadvantages of using standard darkfield microscopy for the detection of nanoparticles in cells is that it can be difficult to differentiate between nanoparticles that are on the surface of the cell and nanoparticles that are inside the cell. In order to overcome this problem a 3D darkfield system was developed in which 2D darkfield images were captured at different focuses and then built up into a 3D image, in order to show the 3D position of nanoparticles relative to cells. The depth of focus of the darkfield system was also measured using this technique and was found to be approximately 2 μm. It was also found that taking the derivative of the image improved the depth of focus slightly.

The hyperspectral darkfield system described in chapter 2 has also been used for collecting spectral information from images of nanoparticles in cells. The hyperspectral system is a useful improvement on standard darkfield microscopy, particularly in the context of using darkfield for detection of nanoparticles inside cells as spectra of bright spots can be used to confirm that they are indeed due to light scattered from the nanoparticle rather than from the cell or another scatterer such as dust on the sample. The use of the hyperspectral darfield system has been demonstrated in this chapter for imaging L929 and SHSY-5Y cells.

Another advantage of darkfield microscopoy over other imaging systems commonly used to detect the presence of nanoparticles inside cells (for example TEM) is that it is well suited to real time imaging of live cells. Real time darkfield imaging of hollow gold nanoparticles in solution and of live cells incubated with nanoparticles has been demonstrated.

Overall, darkfield microscopy has been shown to be a useful tool for detection of nanoparticles inside cells, particularly when combined with a hyperspectral system for measuring spectra of multiple nanoparticles on an image. The hyperspectral system is ideal for measuring nanoparticles in cells as many different sites of interest can be measured simultaneously, which means it is possible to collect spectral information from many different suspected nanoparticle sites in the cell. Spectral information is useful as it enables identification of nanoparticles and could also be used to identify whether the nanoparticles are individual or in small clusters from the different spectral signatures. This information is useful as it could help to understand aggregation effects within cells which could provide information about cellular processes.

Chapter 4

Spatial Modulation Microscopy of Nanoparticles and Cells

Along with darkfield microscopy, another technique that has been used for imaging metallic nanoparticles in this project is spatial modulation microscopy (SMM). The use of a spatial modulation technique for quantitatively measuring the optical properties of plasmonic nanoparticles has been previously demonstrated and has been shown to be a valuble technique for gathering information about the properties of plasmonic nanoparticles as small as 5 nm in diameter [53; 13; 107]. In this project, in order to further increase the usefulness and expand the possible applications of SMM, this technique has been developed into a fast imaging technique with each image covering an area of up to $20 \times 20\mu$m and taking only several seconds to acquire [104].

Another area that has been explored in this project is the potential of using SMM for imaging cells, and in particular for imaging nanoparticles in the cellular environment.

4.1 Theoretical Background

The principle behind the spatial modulation technique can be explained as follows. The nanoparticle is positioned in the focus of a laser beam. The position of the laser beam is then modulated using a piezo mirror, which has the effect of translating the position of the nanoparticle relative to the centre of the laser beam as shown in figure 4.1.

The nanoparticle is much smaller than the focus of the laser beam. The total transmitted laser power with a nanoparticle in the focus of the beam is therefore given by

$$P_t = P_i - \sigma_{ext} I(x, y), \tag{4.1}$$

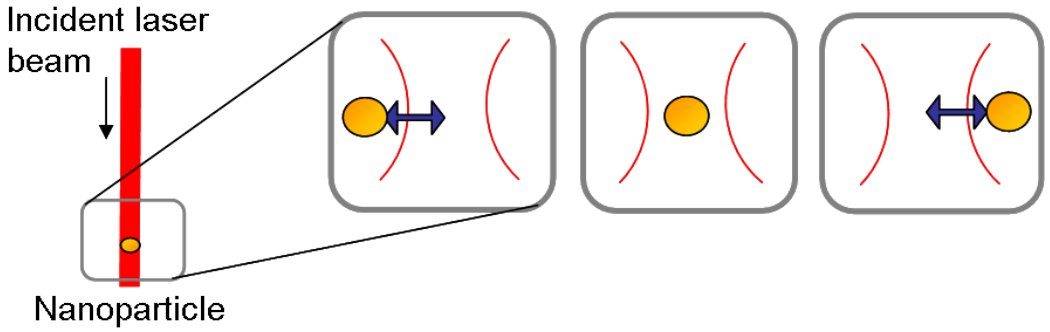

Figure 4.1: Spatial Modulation Microscopy: The position of the nanoparticle is translated in and out of the focus of a laser beam, creating a modulating intensity signal which enables detection using a lock in amplifier or a detector which uses the phase stepping technique.

where P_i is the incident laser power σ_{ext} is the extinction cross section of the nanoparticle $I(x, y)$ is the spatial intensity profile of the beam. When the modulation of the position of the nanoparticle is introduced in the x direction, the transmitted power is given by

$$P_t = P_i - \sigma_{ext} I[x + \delta x \sin(2\pi f t), y], \tag{4.2}$$

where δx is the modulation amplitude and f is the modulation frequency. Because the spatial intensity profile of the beam is a Gaussian, the beam power drops off quite rapidly away from the centre of the focal spot. Therefore, it is sufficient for the modulation amplitude to be small compared to the beam size. Equation 4.2 can therefore be expressed using a Taylor expansion as

$$P_t \simeq P_i - \sigma_{ext} I(x, y) - \sigma_{ext} I'(x, y)\delta x \sin(2\pi f t) - \sigma_{ext} \frac{I''}{2}(x, y)\delta x^2 \sin^2(2\pi f t), \tag{4.3}$$

where I' is the first derivative of $I(x, y)$ with respect to x and I'' is the second derivative of $I(x, y)$ with respect to x. The 2f signal aquires an additional minus sign from equation 4.3 since $\sin^2(2\pi f t) = \frac{1-\cos 4\pi f t}{2}$, which is why the measured 2f signal appears to be reversed in comparison to I".

In order to see the extinction signal of the nanoparticle, the measurement value of interest is $\Delta T/T$, the change in transmission over the total transmission, which is given by $(P_t - P_i)/P_i$ [53]. From equation 4.3 it is apparent that this value will contain components with frequencies $1f$ and $2f$ proportional to I' and I'' respectively.

Because $I(x, y)$ is a Gaussian with a maximum value at $x = 0$, the value of I' is equal to zero when x displacement is zero and I'' is at a minimum as shown in figure 4.2. Therefore

the position of the particle is given by a zero between a maximum and minimum for the $1f$ signal and by a maximum in between two minima for the $2f$ signal.

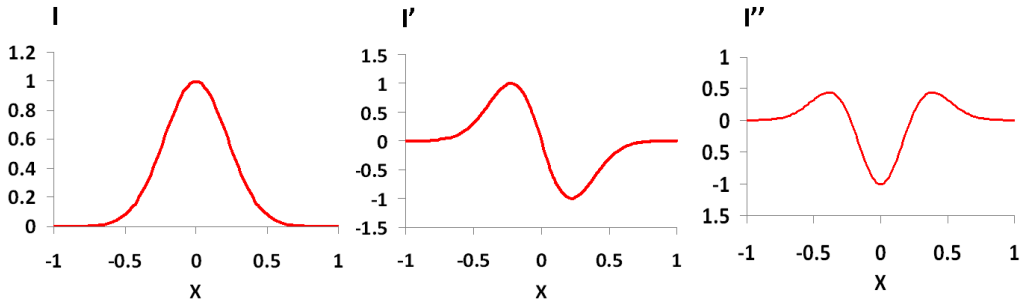

Figure 4.2: The shape of the original beam profile, I, is shown, along with I' and I". The 1f SMM signal is proportional to I' and the 2f signal is proportional to I"

4.2 Point-Scanning Spatial Modulation Microscopy

Spatial modulation microscopy has been demonstrated with a slow, point by point method using a lock-in amplifier and silicon photodiode to recover the small modulating signal on top of the large background. Using this slow scanning method, in order to scan an area of the sample, the sample can be moved using a piezo stage, and an image built up pixel by pixel. The experimental setup used for the lock-in detection method is shown in figure 4.3.

The microscope objective used in the experimental setup had a numerical aperture of 0.9, which can produce a diffraction limited spot size of 389 nm at a wavelength of 700 nm.

Single particle spectra can also be measured using the spatial modulation technique. Figure 4.5 shows the spectrum of the nanorod cluster imaged in figure 4.4 which has been collected by focusing the laser beam onto the cluster, aligning the centre of the laser beam with the cluster by maximising the $\Delta T/T$ signal, and noting the value of $\Delta T/T$ for a range of wavelengths. The wavelength scan was performed by using a supercontinuum laser and an acousto-optic tuneable filter. The spectrum shows a clear peak at 700 nm, which is close to the bulk LSPR of the sample of nanorods at 705 nm. The fact that the spectrum is quite broad indicates that the particle shown in figure 4.4 is likely to be a cluster of nanorods rather than a single particle.

Although lock-in based spatial modulation can be used to measure spectra, this method is more time consuming than the darkfield hyperspectral imaging system described earlier in the project. The spectra measured using spatial modulation spectroscopy must be measured particle by particle and it can be difficult to find particles on the sample

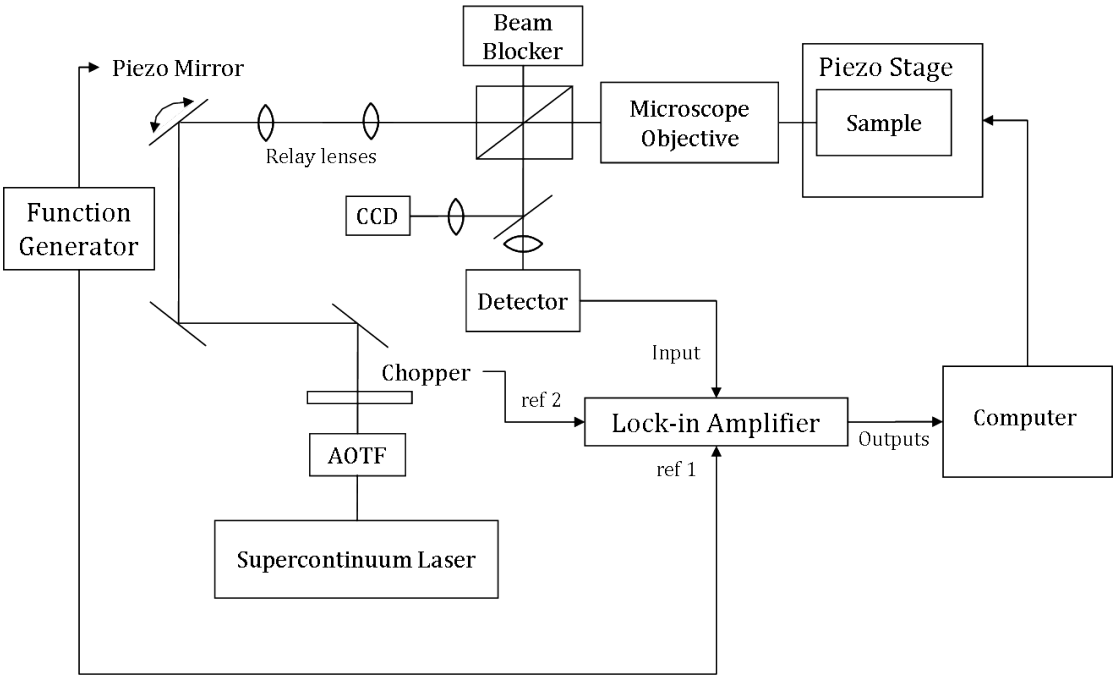

Figure 4.3: Experimental setup for spatial modulation microscopy using a lock-in amplifier.

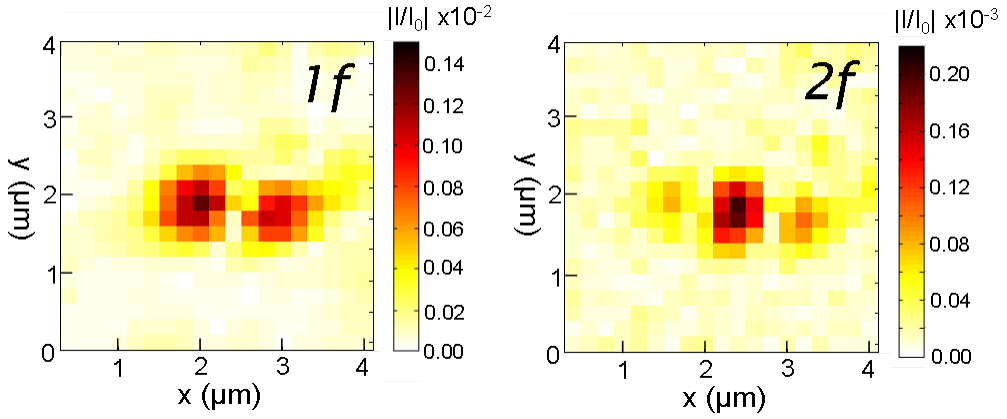

Figure 4.4: 1f and 2f signals for a nanorod cluster measured using the point scanning method at a wavelength of 713 nm

without using another imaging system such as darkfield in order to examine the sample globally.

4.2.1 Imaging of Nanoantennas using the Point-Scanning Method

The point-scanning spatial modulation setup was tested using gold nanoantennas on an ITO coated glass substrate, fabricated with E-beam lithography by M. Abb. The nanoantennas are comprised of two arms, each arm is 200 nm in length, 100 nm wide, and 25 nm thick with a gap between the arms of 20 to 80 nm and were designed to have a resonant dipole mode at around 850 nm [85]. The nanoantennas can be detected

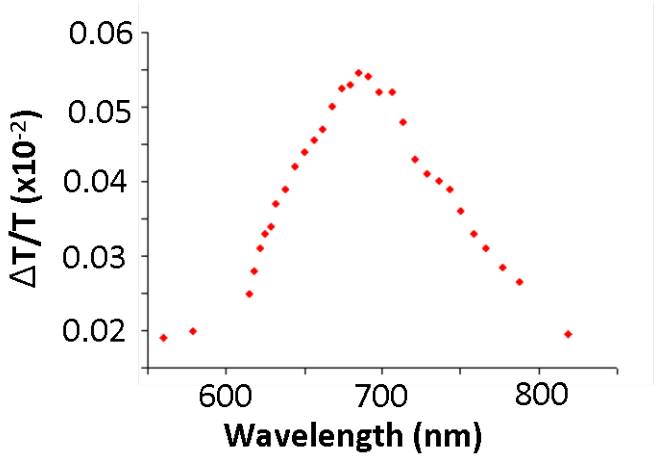

Figure 4.5: Extinction spectrum of nanorod cluster measured using SMM

using spatial modulation microscopy, as shown in figure 4.6. In this case the 2f spatial modulation signal was used. That is, the first harmonic of the modulation frequency was used as the lock-in reference frequency. The reason for using the 2f signal is that this produces a bright area on the image at the position of the nanoparticle, while the 1f signal, (at the fundamental modulation frequency) gives zero intensity at the position of the nanoparticle.

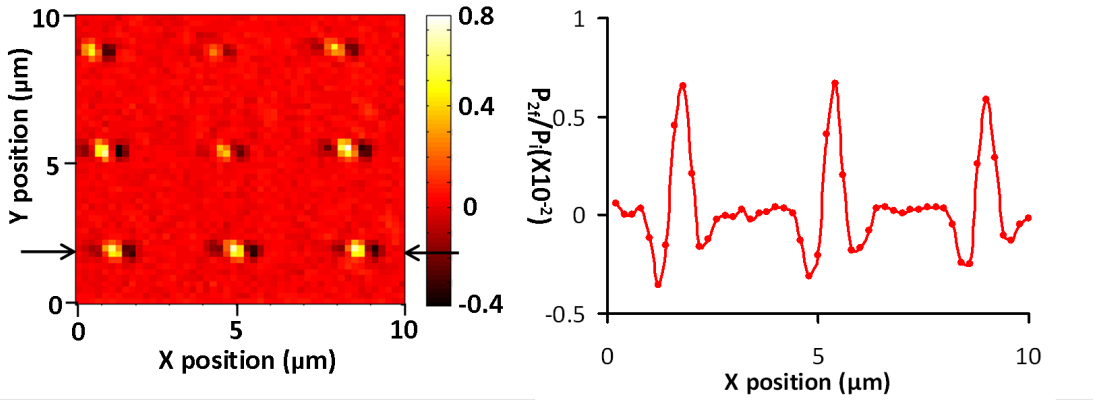

Figure 4.6: 2f SMM image of array of nanoantennas measured with an illumination wavelength of 713nm using the point scanning lock-in detection method, along with a cross section taken through the image at y=2μm through a row of antennas.

It is also possible to calculate a value for the extinction cross section for the antennas, as follows.

For an incident beam with power P_i, focused on the antenna with a width of focus w, and distance x from the centre of the beam, the beam profile I(x) is given by

$$I(x) = \frac{P_i}{\pi w^2} e^{(-x^2/w^2)}. \tag{4.4}$$

The measured 2f signal (T_{2f}) is given by P_{2f}/P_i where P_{2f} is the 2f term in equation 4.3.

$$P_{2f} = -\sigma_{ext}\frac{I''}{2}(x,y)\delta x^2 sin^2(2\pi ft). \tag{4.5}$$

At $x = 0$ the 2nd derivative of I is given by

$$I''(0) = -\frac{2P_i}{\pi w^4}. \tag{4.6}$$

the extinction cross section is therefore

$$\sigma = \frac{\pi w^4 T_{2f}}{dx^2}. \tag{4.7}$$

With a width of focus $w = 500nm$, displacement of the spot in the x direction due to the spatial modulation $dx = 300nm$ and using a value of T_{2f} of 0.65 taken from figure 4.6 this gives an extinction cross section of $1.4 \times 10^4 nm^2$. This value is in reasonable agreement with the calculated cross-sections for these nanoantennas presented in [85].

4.2.2 Imaging of DC 2.4 cells using the Point-Scanning Method

Since this project has a focus on biological applications, the point scanning spatial modulation microscopy technique has also been used to image biological cells. Figure 7 shows SMM images of two different samples of DC 2.4 cells. Sample 1 is a control sample of normal DC 2.4 cells, while sample 2 has been incubated with a solution of CTAB coated gold nanorods.

In image c, the outline of the cell can be clearly seen along with some changes in refractive index within the cell, indicative of internal structure. In images d and e, the highlighted area of interest shows some features with a higher level of extinction than the rest of the cell. Since no cells were seen with these features in sample 1, this would suggest that the areas of higher extinction are due to the presence of gold nanoparticles which may be aggregated within an endosome of the cell. The SMM point scanning method has been shown to have potential use for imaging of plasmonic nanoparticles on a substrate or in a biological cell. However, the images shown in figure 4.7 took approximately two hours to aquire so this is clearly not a viable option for most cellular imaging applications. Therefore the next step in the project was to develop a faster version of SMM imaging system.

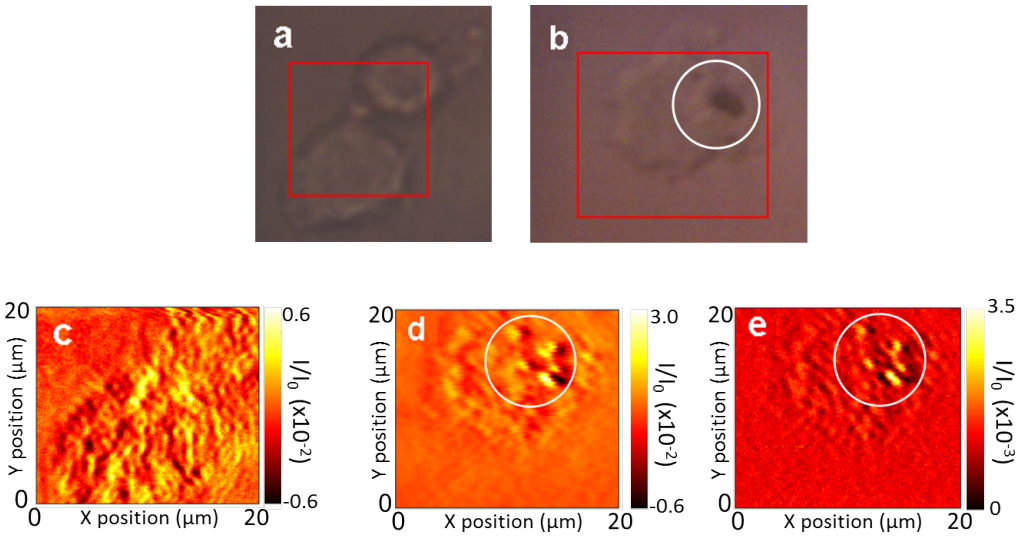

Figure 4.7: a,b) brightfield images of dendritic cells without (a) and with (b) metal nanoparticle incubation. Dark regions in (b) represent nanoparticle aggregates. (c,d) Point-scanning SMM images of the two cells at the 1f frequency measured at 713nm illumination wavelength. (e) Image of sample b at the 2f frequency measured at 713nm illumination wavelength. The red highlighted areas on images a and b are the same areas as images c and d/e repectively

4.3 SMM - Fast Scanning Method

The current disadvantage of using the lock-in technique is that it requires point by point measurements on individual nanoparticles and scanning across an area using this technique is very time consuming. Here, a new technique is demonstrated which enables the development of the spatial modulation measurement technique into an imaging system which can be used for simultaneous measurement of nanoparticles spread over an area of $20 \times 20\mu$m. This fast scanning spatial modulation method makes use of a CMOS modulated light camera produced by the research group of Prof. M. Somekh at Nottingham University. The line camera uses a phase stepping technique to detect a modulating signal [71; 72]. The use of the line camera means that a lock in amplifier is no longer needed to detect the modulating signal produced by the spatial modulation technique. The line camera can also detect light incident on a line of pixels simultaneously, which speeds up the measurement time since a piezo stage is only needed to scan one dimension rather than two. The fast scanning technique shown here has improved the time taken to image an area on the sample of 20x20 μm from over an hour when using a point scanning system, to approximately 1 second

4.3.1 Experimental Methods

The CMOS camera enables simultaneous detection of a line of pixels. An image can therefore be collected much faster than the point scanning method described earlier in

this chapter. The experimental set up for the line scanning method can be explained as follows. A vertical line focus was created from a 690nm laser diode source using a cylindrical lens. The sample was measured in transmission using a microscope consisting of two 100× 0.9 NA microscope objectives. The light transmitted through the camera can either be directed onto the CMOS line detector or a CCD camera, which is used for sample positioning along with a brightfield illumination set up. A diagram of the experimental set up is shown in figure 4.8.

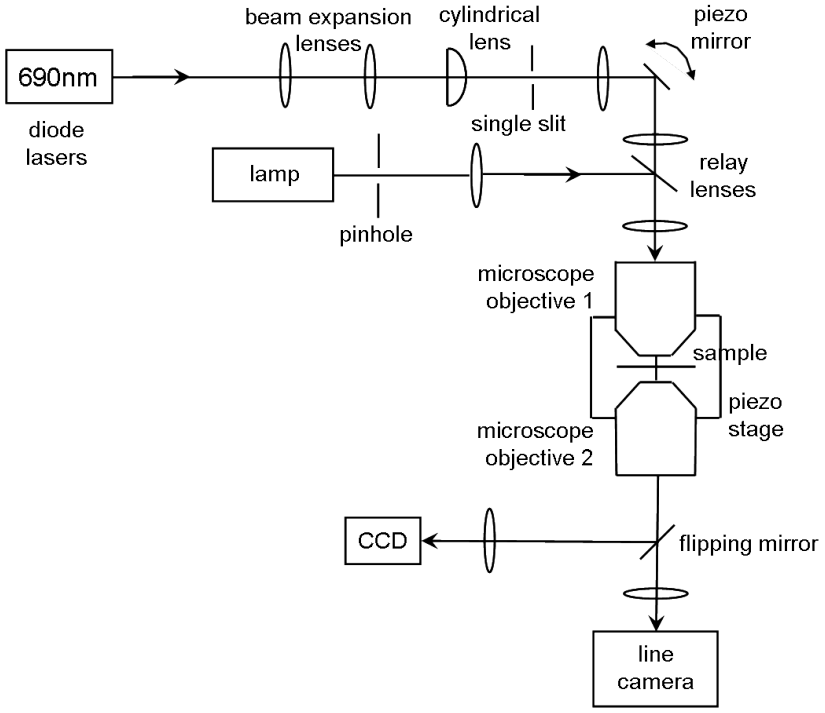

Figure 4.8: Experimental setup for spatial modulation microscopy measurements using CMOS line camera.

The CMOS line camera makes use of multiple wells and a phase stepping technique to detect a modulating signal, replacing conventional lock-in detection. The camera features a pixel well depth of 2 x 10^9 electrons, allowing a theoretical shot noise limited performance of 2 x 10^{-5} per well. The phase stepping technique can be explained as follows. The intensity of the light source on the detector, when the position of the focus is modulated using a single frequency sine wave is given by equation 4.8.

$$I = A + B\cos(\omega t + \phi) \tag{4.8}$$

The camera samples the waveform four times per cycle (every 90°) and aquires four different values of I, leading to a set of four simultaneous equations (4.9):

$$I_1 = A + B\cos(\phi)$$

$$I_2 = A - B\sin(\phi)$$

$$I_3 = A - B\cos(\phi)$$
$$I_4 = A + B\sin(\phi). \tag{4.9}$$

These equations are solved to give;

$$A = (I_1 + I_2 + I_3 + I_4)/4$$
$$B = \sqrt{(I_1 - I_3)^2 + (I_4 - I_2)^2}/2$$
$$\phi = tan^{-1}\frac{I_4 - I_2}{I_1 - I_3}. \tag{4.10}$$

The CMOS line camera has four wells per pixel, therefore it is able to sample higher modulation frequencies than a conventional camera as the four phase steps can be aquired and stored without needing to readout the camera after each step. The intensity signal in every well is integrated over a quarter of a cycle for each step, after which the on-chip electronics switches to the next well.

It is also possible to obtain the 1f and 2f components of the modulated signal using the CMOS line camera, as long as the phase of the fundamental and harmonics are known and remain constant. The amplitudes of the 1f and 2f components are given by

$$\Delta I_{1f} = [(I_1 + I_2) - (I_3 + I_4)]/2$$
$$\Delta I_{2f} = [(I_1 - I_2) + (I_3 - I_4)]/4. \tag{4.11}$$

4.4 Normalisation of Images

After the collection of raw images using the line scan method, the images were further processed in order to improve their quality. The raw images are prone to contain noise in the form of lines of high and low intensity across the image which is due to the line of laser light not having a constant intensity along its length, and because of slight differences in sensitivity of different pixels of the line camera. In order to improve the quality of the image, a few columns at an edge of the intensity image, away from the cell, were averaged over to produce a single column of average values, which were then subtracted from each of the individual columns in the image. An example of an intensity image before and after processing is shown in figure 4.9. To normalise the 1f and 2f images, the images were divided by this normalisation factor. The reason for using an average taken from columns of pixels at one edge of the image as a normalisation factor was to use an average of the background, in order to remove only the horizontal lines from the image without removing parts of the image relating to the cell. Since the horizontal lines were different for images taken at different times, using an edge of the image itself

was found to give a better result than taking a separate reference image of an empty area of the sample and using this as the normalisation factor.

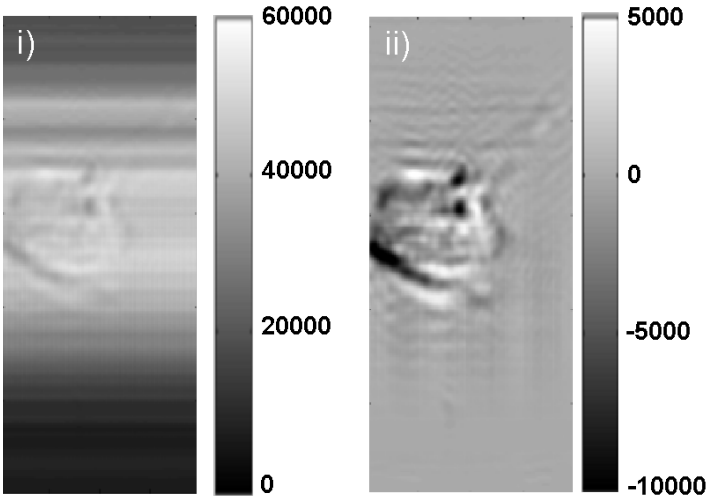

Figure 4.9: Image of a dendritic cell measured using line scanning technique i) before and ii) after normalisation.

The ripples in the image are likely coherence artifacts caused by the coherence of the laser used in taking the image and diffraction of light from the object [108].

4.5 Results

The SMM line scanning system has been used to image an array of gold nanoantennas on an ITO coated glass substrate, fabricated with E-beam lithography by M. Abb, in order to demonstrate the limits in sensitivity of the system. The nanoantennas are comprised of two arms, each 200nm in length, 100nm wide, and 25nm thick with a gap between the arms of 20 to 80nm with a resonant dipole mode at around 850 nm [85]. An SEM image of the nanoantennas is shown in figure 4.11(a).

Two-dimensional SMM maps were made of the transmitted intensity T_I as well as the 1f and 2f components of the spatial modulation intensity, respectively denoted as ΔT_{1f} and ΔT_{2f} [53]. For the intensity graph, the normalisation method described in the previous section was used. That is, an average line frame in absence of antennas (denoted as $\langle T \rangle$) was subtracted to remove a constant variation in pixel illumination. Figure 4.11(b) shows typical cross-sections through a single antenna selected from a larger image shown in Fig. 4.11. The signals can be fitted to a Gaussian beam profile for ΔT and its first and second derivatives for ΔT_{1f} and ΔT_{2f}, as expected from theory [53]. The fits yield a full-width-at-half-maximum of 0.8 ± 0.1 μm. This is larger than the diffraction limit due to aberrations in the imaging system. The depth of focus of the SMM signals follows the divergence of the Gaussian beam and results in a decay over ~ 1.5 μm. The absence

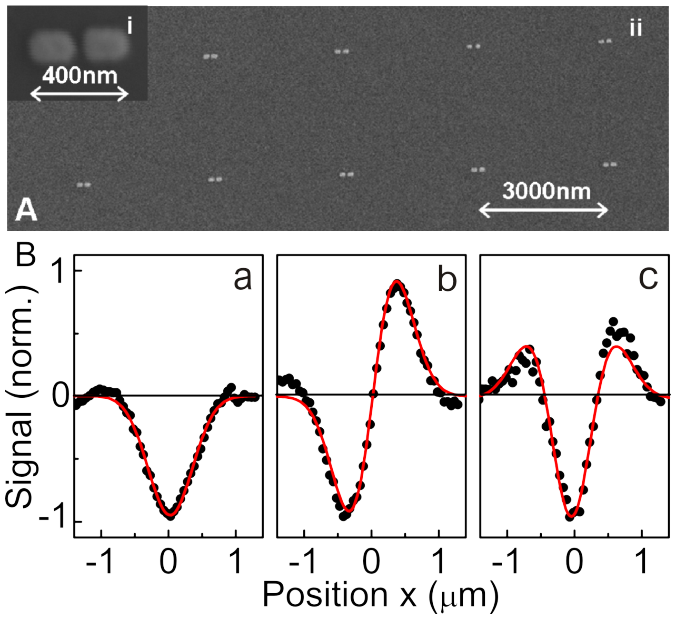

Figure 4.10: a) SEM images of nanoantennnas, with close up of single antenna. (b) Experimental data for a single antenna for a) intensity $T_I - \langle T \rangle$, and SMM profiles at b) first (ΔT_{1f}) and c) second harmonic (ΔT_{2f}) of the modulation frequency, together with fits (lines) to the derivatives of a Gaussian beam profile of 0.8 ± 0.01 μm width.

of an out-of-focus background signal is of potential use in imaging of three-dimensional specimens.

Figure 4.11 shows the SMM image obtained for a 20×25 μm^2 area containing nanoantennas. Each line was averaged over 4 frames, resulting in a total acquisition time of 2 seconds. This is an improvement in collection time by more than two orders of magnitude compared to conventional point-scanning SMM [53]. Only a central 120-pixel part of the 256-pixel array in the y-direction is displayed containing the antenna array. Horizontal cross-sections through a row of antennas (indicated by arrows) are shown in Fig. 4.11(b), where the $1f$ and $2f$ components have been normalised to the average intensity $\langle T \rangle$ to obtain the relative spatially modulated transmission.

The noise level was calculated by subtracting a 5 point moving average from the original traces, which was taken at a horizontal step size of 50 nm. Resulting noise traces are given by the grey lines in the cross sections of figure 4.11. Average noise levels were found to be 3×10^{-4} and 1×10^{-4} for the 1f and 2f signals respectively. This noise level is higher than that expected from the shot-noise limit, due to some residual technical noise introduced by the laser and imaging system. The signal to noise ratio exceeds 100 for the antennas under study at the 1f frequency, demonstrating the ability of the system to image individual nanostructures.

For comparison, a darkfield image of the same nanoantennas is shown in figure 4.12. The wavelength used for the darkfield image is 691nm, so that there is no difference in

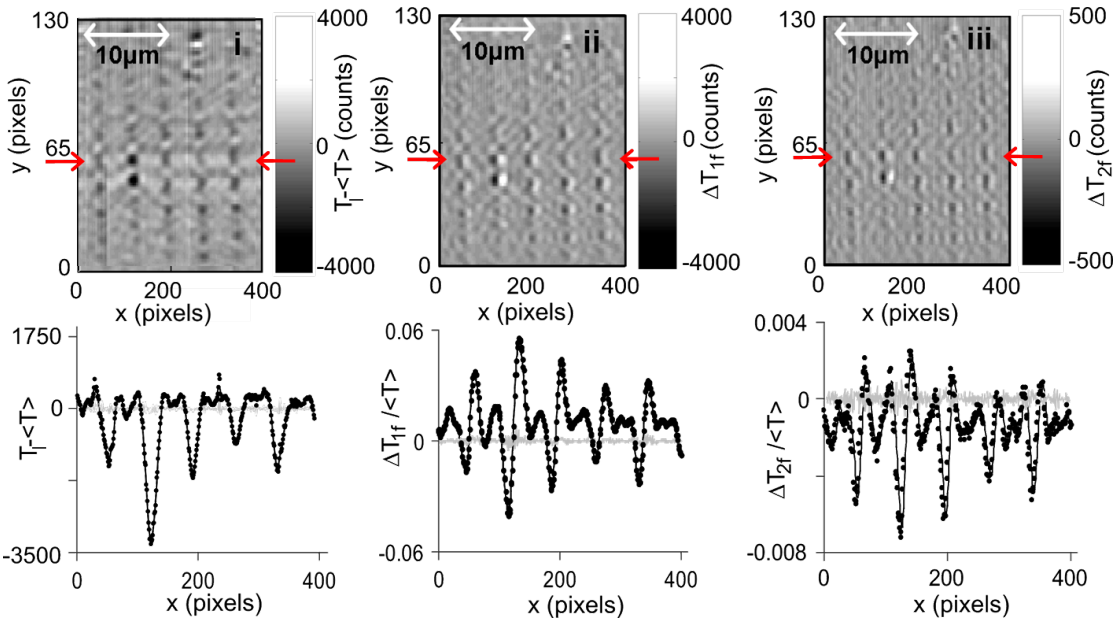

Figure 4.11: Spatial modulation microscopy maps of intensity difference from average (i), first harmonic (ii) and second harmonic components (iii) of the spatial modulation signal. Line graphs (I-III) are cross sections of the maps normalized to the average intensity, with (grey lines) noise background after subtraction of moving average.

the optical properties of the nanoantennas as the images are measured on the same part of the plasmon resonance peak. The darkfield image has a signal to noise ratio of ≈ 125 which is higher than the signal to noise ratio that has been achieved with the SMM fast scanning system. Darkfield microscopy also allows a larger area of the sample to be viewed at once, as no scanning is required (the SMM system is limited by the travel of the stage and the number of pixels in the line camera). However, darkfield microscopy only detects light which has been scattered by the nanoparticles. Darkfield therefore works well for larger nanoparticles, where scattering dominates the optical response, such as the 200nm arm length antennas shown here. For smaller nanoparticles however, absorption becomes more dominant than scattering and therefore it becomes difficult to detect small nanoparticles (<50nm diameter) using darkfield microscopy. Spatial modulation microscopy measures the difference between the incident laser beam power and the transmitted power, so uses both scattered and absorbed light.

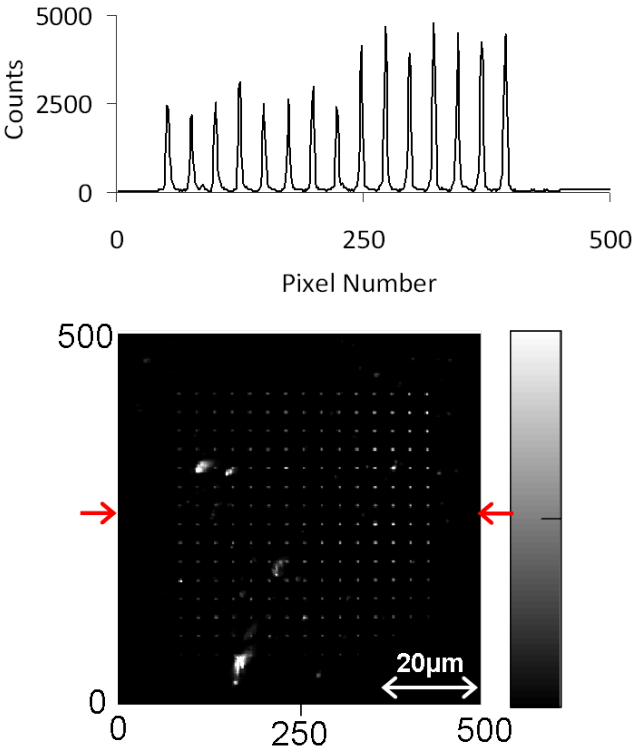

Figure 4.12: A darkfield image of an array of nanoantennas measured at an illumination wavelength of 691nm, along with a cross section through the line of antennas indicated by the red arrows.

4.6 Spatial Modulation Microscopy for Cell Imaging

Next, the potential of the line scanning method for the measurement of biological cells, and in particullar the imaging of gold nanoparticles inside a cellular environment was investigated. The spatial modulation microscopy method was used to image a sample of dendritic cells which were incubated with 5μl of gold nanorod solution for 2hrs. The gold nanorods had an average length of 47nm and average width of 16nm, with an LSPR in water around 690nm. The intensity, 1f and 2f images are shown in figure 4.13 along with a cross section of each image. The 1f and 2f components give the first and second derivatives of the cell, which results in an enhancement of edges and point-like objects. A nanoparticle aggregate that has been engulfed by the cell can be seen using the SMM system, however it is unlikely that single nanoparticles of the size used in this experiment would be able to be detected against the cellular background. The expected SMM signal from individual nanorods is around 10^{-3} [106] which is much smaller than the cellular background signals measured here, which is of order 10^{-2} to 10^{-1}.

In comparison to the resolution achieved with darkfield microscopy in this project, the SMM method is not as effective for cellular imaging as the dark field imaging. In particular, the SMM system is less suited to live cell imaging as the time needed to take

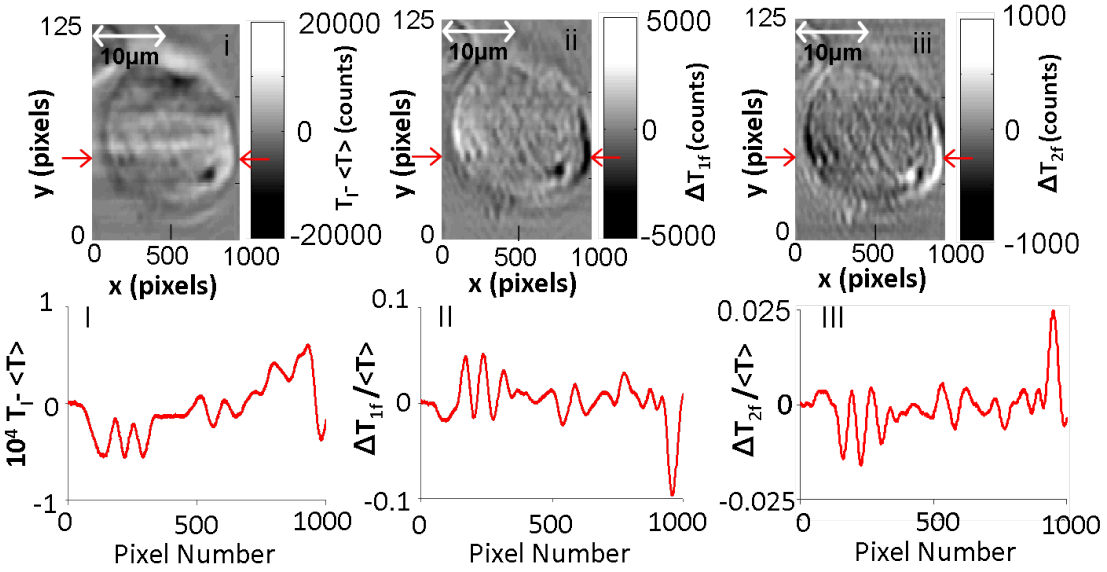

Figure 4.13: i - Intensity, ii - 1f and iii - 2f SMM images of dendritic cells along with a cross section.

an image is approximately 1 sec. For live cell imaging, it is desirable to have as short an exposure time as possible. Darkfield images of cells incubated with nanoparticles can be easily taken in 0.1 sec so darkfield microscopy may be more suited to live cell imaging or tracking movement of nanoparticles in any applications where they may be moving quickly. However, SMM may have other benefits for cellular imaging, such as the access to higher-order spatial derivatives of structures, and the potential for three-dimensional optical sectioning due to the absence of out-of-focus contributions. These aspects go beyond the current investigation and will have to be addressed in future studies.

In the results shown in this chapter, the quality of the line images is limited by the quality of the line focus used to illuminate the sample. The quality of the line focus was limited by the quality of the spot from the diode laser and the cylindrical lens used. The line focus tended to be much brighter in the middle and also contained fringes. However, this is not a fundamental limitation of the system.

4.7 Conclusions

Spatial modulation is a valuable technique for detection and spectroscopy of metallic nanoparticles. In this project, a point scanning version of SMM was first set up which collected image data pixel by pixel and scanned over an area of pixels with a piezo stage. A lock-in detector was used to recover the signal and discard any noise which was not varying at the same frequency as the modulation frequency. The main disadvantage of the point scanning method was that the image aquisition time was extremely long, taking over an hour to image an area on the sample of 20x20 μm. In order to improve the

image aquisition time, a faster, line scanning method was developed which decreases the aquisition time to 1-2 secs per image. The line scanning spatial modulation microscopy technique demonstrated in this chapter enables simultaneous imaging/measurement of multiple nanoparticles, for example an array of nanoantennas. The signal to noise ratio of 100 acheived by using the 1f modulation signal shows that the sensitivity of the system is good enough to easily resolve nanoantennas of 400 nm total length by 100 nm width.

The sensitivity of the SMM signal to small variations in optical density may prove to be a viable alternative to phase-sensitive imaging under conditions where phase information is distorted, e.g. for very thick samples. This application may be further enhanced by the availability of a higher order derivative image, and the absence of out-of-focus glare. Key aspects of SMM are retained by the setup while improving the acquisition time by several orders of magnitude, therefore opening up new applications requiring simultaneous imaging and measurement of multiple nanoparticles e.g. in microfuidic environments.

The advantage of the spatial modulation technique over a technique such as darkfield microscopy which detects only the light which has been scattered back from the particles is that spatial modulation detects the difference in transmitted light caused by scattered and absorbed light, which enables detection of smaller particles that would be difficult to detect using darkfield microscopy due to the rapid decrease of scattering ability with size of plasmonic nanoparticles.

However, the area covered by each image is still relatively small (a larger area could be covered but the time to measure each image would increase). The nanoparticles are also harder to detect and identify on the cellular background. Darkfield microscopy has therefore been found to be preferable to spatial modulation microscopy for the purpose of live cell imaging in this project.

Overall, the fast scanning spatial modulation method is a useful characterisation tool for detection and spectroscopy of metallic nanoparticles, in particular this system is useful for imaging and characterising multiple nanoparticles at once, for example an array of nanoantennas or colloidal nanoparticles that have been deposited on a glass slide.

Chapter 5

Conclusions

5.1 Summary

In this thesis, results have been presented on the development of several new imaging techniques for the detection of nanoparticles in biological cells. There have been three main areas of focus in the project. Firstly the development of nanoparticle spectroscopy using the hyperspectral darkfield system; secondly, detection of nanoparticles in cells using this technique; and thirdly, development of a fast spatial modulation microscopy for capturing images of nanoparticles on a substrate or in cells.

In particular, these systems have been developed for the purpose of detecting nanoparticles present in cells. The reasons for focusing on this aspect of imaging is because metallic nanoparticles are currently being developed for many different biomedical applications so there is a need for ways of detecting their presence inside cells. Current methods for detecting the presence and location of nanoparticles inside cells have many disadvantages. The main methods of detecting the presence of nanoparticles inside cells currently are to use transmission electron microscopy (TEM) to look at thin sections of cells or to label the nanoparticles with a fluorescent tag or to use quantum dots as nanoparticles which can be detected due to emitted light. The disadvantages of (TEM) are that it is time consuming and expensive. The disadvantages of fluorescence are toxicity and photobleaching and the disadvantages of using quantum dots are toxicity and blinking. The toxicity of metallic nanoparticles is still being investigated and is likely to depend on the size of the nanoparticle as well as the material it is made from. However, it is very likely that metal nanoparticles produced from inert metals such as gold are less toxic than quantum dots of similar sizes made from materials that are inherently very toxic such as cadmium compounds. Fluorescent tags are often attached to metallic nanoparticles in order to track them in a cell. This is likely to increase the toxicity compared to metal nanoparticles which have not been labeled with fluorescent dyes. Since metallic nanoparticles have such inherently strong optical properties, they

may be used as detectable labels in their own right, without the need to increase their toxicity by adding fluorescent dyes. There are clearly some applications for which methods such as TEM or the use of quantum dots or fluorescence have advantages over the imaging methods that have been developed in this project. For example, in order to see how nanoparticles interact with a particular organelle within a cell, TEM has a much higher resolution than other microscopy methods, and can clearly resolve the different organelles inside a cell.

There is no single imaging method which is ideal for all applications, rather, an imaging toolkit must be developed, of which darkfield microscopy and spatial modulation microscopy are valuble parts.

The hyperspectral darkfield method was developed from an earlier system that was first developed for measuring extinction spectra of bulk solutions of nanoparticles using an acousto-optic tuneable filter and a supercontinuum light source. The measured spectra were found to be in good agreement with bulk extinction spectra measured with a UV-Vis spectrometer. The method of using the combination of supercontinuum source and AOTF was then further developed into a system for measuring single particle spectra in a darkfield setup. The single particle spectra were measured by collecting a series of images at different wavelengths and then building up spectra of the individual particles from the series of images. Therefore it was possible to measure spectra for each particle in the image simultaneously.

The hyperspectral darkfield imaging system relies on detecting light that has been scattered by the nanoparticles. Since scattering rapidly decreases with particle size this means that this system is most useful for imaging larger nanoparticles such as hollow gold particles which can be detected individually and individual spectra can be measured using the darkfield system. In this project the darkfield microscope has been tuned to detect nanoparticles with an LSPR in the near infrared part of the spectrum. This wavelength range is the most important for biological applications, as transmission of light through biological tissue is highest in the near infrared. An advantage of the hyperspectral darkfield system used in this project in comparison with other available systems is that it does not illuminate the sample with high power white light but with one wavelength at a time at low power (less than 0.1mW was used to illuminate an area of 150μm in diameter). Thus, this system is ideal for imaging biological samples where high power irradiation of the sample may cause damage, for example when imaging live cells.

Spectra of lithographically produced nanoantennas were measured and the transverse and longitudinal LSPR peaks were seen at orthogonal polarisations.

Spectra of individual colloidal gold nanorods were measured and compared with theoretical spectra. The measured spectra were found to be in good agreement with theoretical spectra produced by M. Abb using the finite element method. Spectra of colloidal hollow

gold nanospheres were also measured and correlated with transmission electron microscope images of the same particles and particle clusters. The spectra were also compared to theoretical spectra produced by the finite element method and found to be in good agreement.

The hyperspectral imaging system was also used to measure the spectra of clusters of silver nanocubes on a silicon substrate. Spectra were measured for two different polarisation angles and a polarisation study was also undertaken. The measured spectra and polarisation dependence were directly correlated with SEM images of the same clusters. At this stage, no detailed comparison with theoretical calculations is available, due to the complex geometry of the high-refractive index substrate. Ultimately, these measurements will be useful for understanding ongoing experiments by O. Rabin and co-workers on surface-enhanced Raman scattering by silver nanocubes.

In addition to measuring spectra of single nanoparticles, the hyperspectral imaging system has also been used for imaging nanoparticles in the cellular environment. Since metal nanoparticles scatter light strongly they can be seen in darkfield illumination even on a cellular background as has been demonstrated with a study of dendritic cells that were incubated with different concentrations of colloidal nanorods for different amounts of time. The batch of cells incubated with the highest concentration of nanoparticles for the longest amount of time (40μl of OD 2.5 nanorod solution for 2hrs) was found to show the highest darkfield signal at the LSPR resonance wavelength of the nanorods. The signal was significantly lower off resonance, and for cells not incubated with nanorods, showing that the scattered light was due to the nanorods rather than to another source such as the cell itself. An increase in signal was also seen for cells that were incubated with nanorods for a longer time, suggesting uptake of the nanoparticles by the cells.

In order to gain more information about the exact location of nanoparticles in comparison to cells and therefore see if nanoparticles were inside or outside cells, a system for producing 3D images was developed. Images were taken at a series of different z positions using a piezo stage and then stacked to form a 3D image. Nanoparticles could be localised in the z direction to within 2μm using this method.

The hyperspectral darkfield system was also used to measure spectra of individual bright spots, a few pixels in area on darkfield images of cells, in order to determine whether these individual bright spots were due to light scattered from nanoparticles. Studies of L929 (fibroblast) cells incubated with nanorods and SHSY-5Y (neuroblastoma) cells incubated with hollow gold nanoparticles were performed and in both cases it was possible to distinguish between the darkfield signal due to nanoparticles and that due to light scattered by the cells since the spectra of the light scattered from the nanoparticles showed LSPR peaks not present in the spectra of light scattered from the cell.

Real time darkfield imaging also holds potential as a useful tool for characterising nanoparticles in the cellular environment as it could enable nanoparticle uptake to be

studied in real time. Although a full study of nanoparticle uptake was outside of the scope of this project, real time imaging of live cells incubated with nanoparticles and of nanoaparticles in solution was sucessfully demonstrated.

In addition to darkfield microscopy, a further method for imaging nanoparticles was also investigated in this project in the form of spatial modulation microscopy (SMM). The principle of SMM is that the laser beam incident on a nanoparticles is spatially modulated at a known frequency. Therefore noise which is not at the same frequency as the signal can be discarded giving a high signal to noise ratio. SMM was first set up as a point scanning method where the images were recorded a pixel at a time. A high signal to noise ratio was achieved using this method but the capture time was extremely long, taking over an hour to acquire an image covering an area of 20x20μm on the sample. The point scanning method was used to image lithographic nanoantennas and dendritic cells that had been incubated with gold nanorods.

The SMM image capture time was improved by using a line scanning system that acaquired a line of pixels simultaneously. The image capture time with the line scanning method was decreased by two orders of magnitude to 1 to 2 seconds for a 1500x256 pixel image with a noise level of 10^{-4} for the 1f images. The line scanning method was also used to image an array of lithographic nanoantennas and dendritic cells incubated with gold nanorods. Unlike darkfield, SMM effectively measures light absorbed by the nanoparticle as well as scattered light which enables it to be used to image much smaller nanoparticles.

5.2 Future Work

Both of the imaging systems used in this project have the potential to be developed further. Since the hyperspectral darkfield system is suited to imaging of nanoparticles in live cells, it would be interesting to use this system to study nanoparticle uptake and other biological processes in real time. Fluorescence imaging may be used along with darkfield microscopy to stain particular organelles which would help to see how the nanoparticles are interacting with the cells. A possible study which would be of interest and follows on from the work done in this project on SHSY-5Y cells would be to use the hyperspectral darkfield system to look at axonal transport in neurons, since it is of interest in regards to cytotoxicity to know whether nanoparticles can be transported along neurons if they enter the nervous system.

Another improvement that could be made to the hyperspectral darkfield would be to automate the scanning of the piezo stage to perform fast 3D imaging, this could then potentially be used for 3D imaging of live cells. The focus optimisation for different wavelengths could also be automated when performing the wavelength scan, which would speed up the time required to perform a wavelength scan enabling collection of spectra for

live cell samples in addition to fixed cell samples. A decrease in time taken to perform spectral measurements is of interest since, if spectra could be measured very quickly then changes in the dielectric environment of nanoparticles in cells could be measured, giving information about cellular processes such as whether or not nanoparticles are aggregating in a cell.

Examples of possible future work for the spatial modulation microscopy system would be to achieve superresolution imaging with this technique through the use of image processing techniques. In addition, to implement a system where modulation information is aquired for both the x and y dimensions of each image. Spatial modulation microscopy also has great potential for use in imaging of biological cells, including live cells, particularly now that fast imaging is possible. There is also potential to implement 3D cell imaging with spatial modulation microscopy, which would be of particular interest if superresolution was achieved using this technique. 3D imaging is particularly suited to SMM as the out of focus light in the 1f and 2f images is reduced since the images have effectively been differentiated already, without the need for further image processing.

Both hyperspectral darkfield and spatial modulation microscopy have potential for further developments to further improve their usefulness and applicability, which will enable them to continue to be valuable techniques for nanoparticle characterisation in non biological as well as biological applications.

References

[1] Jain, P et al *Noble Metals on the Nanoscale: Optical and Photothermal Properties and Some Applications in Imaging, Sensing, Biology, and Medicine*; Acc. Chem. Res. **2008** *41* p1578-1596.

[2] Arvizo, R et al *Intrinsic therapeutic applications of noble metal nanoparicles: past, present and future* Chem. Soc. Rev. **2012** *41* p2943-2970.

[3] Dreaden, E. et al *The golden age: gold nanoparticles for biomedicine* Chem. Soc. Rev. **2012** *41* p2740-2779.

[4] Loo, C et al *Gold nanoshell bioconjugates for molecular imaging in living cells*; Opt. Lett. **2005** *30* p1012-1014.

[5] Saha, K. et al *Gold Nanoparticles in Chemical and Biological Sensing*; Chem. Rev. **2012** *112* p2739-2779.

[6] Kennedy, L et al *A New Era for Cancer Treatment: Gold-Nanoparticle-Mediated Thermal Therapies*; Small **2010** *10* p1-15.

[7] Ghosh, P. et al *Gold Nanoparticles in delivery applications* Adv. Drug Deliv. Rev. **2008** *60* p1307-1315.

[8] Erathodiyil, N. et al *Functionalization of Inorganic Nanoparticles for Bioimaging Applications* Acc. Chem. Res. **2011** *44* p925-935.

[9] Alkilany, A. et al *The Gold Standard: Gold Nanoparticle Libraries To Understand the Nano-Bio Interface* Acc. chem. Res. **2012**, *ASAP*.

[10] Villiers, C et al *Analysis of the toxicity of gold nano particles on the immune system: effect on dendritic cell functions* J. Nanopart. Res. **2010** *12* p55-60.

[11] Lewinski, N. et al *Cytotoxicity of Nanoparticles* Small **2008**, *4* p26-49.

[12] Peckys, D. and de Jonge, N. *Visualizing Gold nanoparticle Uptake in Live Cells with Liquid Scanning Transmission Electron Microscopy* Nano Lett. **2011** *11* p1733-1738.

[13] Muskens, O. et al *Single metal nanoparticle absorption spectroscopy and optical characterization* App. Phys. Lett. **2006** *88* p3109-3111.

[14] Nohynek, G. et al *Grey Goo on the Skin? Nanotechnology, Cosmetic and Sunscreen Safety* Crit. Rev. Toxicol. **2007** *37* p251-277.

[15] Atwater, H. and Polman, A. *Plasmonics for improved photovoltaic devices* Nat. Mat. **2010** *9* p205-213.

[16] Catchpole, K. and Polman, A. *Plasmonic Solar Cells* Opt. Express **2008** *16, 26* p21793-21800.

[17] Moshfegh, A. et al *Nanoparticle Catalysts* J. Phys. D: Appl. Phys. **2009** *42*

[18] Soppimath, K. et al *Biodegradable polymeric nanoparticles as drug delivery devices* J. Control. Release **2001**, *70* p1-20.

[19] Michalet, X. et al *Quantum Dots for Live Cells, in Vivo Imaging, and Diagnostics* Science **2005**, textit307, 5709 p538-544.

[20] An-Hui Lu et al *Magnetic Nanoparticles: Synthesis, Protection, Functionalization, and Application* Angew. Chem. Int. Ed. **2007**, *46* p1222-1244.

[21] Xie, J. et al *Surface-Engineered Magnetic Nanoparticle Platforms for Cancer Imaging and Therapy* Acc. Chem. Res. **2011**, *44* p883-392.

[22] Barreto, J et al *Nanomaterials: Applications in Cancer Imaging and Therapy* Adv. Mater **2011**, *23* pH18-H40.

[23] Kumar, R et al *Hollow gold nanoparticles encapsulating horseradish peroxidase*; Biomater. **2005**, *26* p6743-6753.

[24] Huang, X et al *Cancer Cell Imaging and Photothermal Therapy in the Near-Infrared Region by Using Gold Nanorods* J. Am. Chem. Soc. **2006**, *128* p2115-2120.

[25] Schröder, U. and Sabel, B. *Nanoparticles, a drug carrier system to pass the blood-brain barrier, permit central analgesic effects of i.v. dalargin injections* Brain Res. **1996** *710, 1-2* p121-124

[26] Kreuter, J. et al *Passage of peptides through the blood-brain barrier with colloidal polymer particles* Brain Res. **1995**, *674, 1* p171-174.

[27] Bartczak, D et al *Laser-Induced Damage and Recovery of Plasmonically Targeted Human Endothelial Cells* Nano Lett. **2011**, *11, 3* p1358-1363.

[28] Nie, S and Emory, S. *Probing Single Molecules and Single Nanoparticles by Surface-Enhanced Raman Scattering* Science **1997** *275* p1102-1106.

[29] Cialla, D. et al *Surface-enhanced Raman Spectroscopy (SERS): Progress and Trends* **2012** *403* p27-54.

[30] Grubisha, D. et al *Femtomolar Detection of Prostate-Specific Antigen: An Immunoassay Based on Seurface-Enhanced Raman Scattering and Immunogold Labels* Anal. Chem. **2003** *75* p5936-5943.

[31] D.M. Kemeny and S.J. Challacombe *Elisa and Other SOlid Phase Immunoassays: Theoretical and Practical Aspects* John Wiley and Sons **1988**.

[32] Stevens, M et al *Plasmonic ELISA for the ultrasensitive detection of disease biomarkers with the naked eye* Nature Nanotech. **2012**, *7* p821-824.

[33] Sau, T. and Murphy, C. *Seeded High Yield Synthesis of Short Au Nanorods in Aqueous Solution* Langmuir **2004** *20* p6414-6420.

[34] Maier, S *Plasmonics: Fundamentals and Applications*; Springer, New York **2007** p11-12

[35] Barnes, W. and Murray, A *Plasmonic Materials*; Adv. Mater. **2007**, *19*, p3771-3782.

[36] Biswas, A et al *Single metal nanoparticle spectroscopy: optical characterization of individual nanosystems for biomedical applications*; Nanoscale **2010** *2* p1560-1572

[37] Mie, G *Beiträge zur Optik trüber Medien, speziell kolloidaler Metallösungen*; Ann. der Physik, 4th series **1908**, *25* p337-445.

[38] Johnson, P. and Christy, R. *Optical Constants of the Noble Metals*; Phys. Rev. B **1972**, *6,12* p4370-4379.

[39] Knight, M. and Halas, N. *Nanoshells to nanoeggs to nanocups: optical properties of reduced symmetry core-shell nanoparticles beyond the quasistatic limit*; New J. Phys. **2008** *10* p105006.

[40] Loo, C et al *Nanoshell-Enabled Photonics-Based Imaging and Therapy of Cancer*; Technol. Cancer Res. Treat. **2005**, *3* p33-40.

[41] Zijlstra, P. and Orrit, M. *Single metal nanopaticles: optical detection, spectroscopy and applications* Rep. Prog. Phys. **2011** *74* 106401.

[42] Fischer, U. and Pohl, D.*Observation of Single-Particle Plasmons by Near-Field Optical Microscopy* Phys. Rev. Lett. **1989** *62* p458-461.

[43] van Dijk, M. et al *Absorption and scattering microscopy of single metal nanoparticles* Phys. Chem. Chem. Phys. **2006** *8* p3486-3495.

[44] Sonnichsen, C. et al *A molecular ruler based on plasmon coupling of single gold and silver nanoparticles*; Nat. Biotechnol. **2005** *23* p741-745.

[45] Kukura, P. et al *High-speed nanoscopic tracking of the position and orientation of a single virus* Nat. Meth. **2009** *6* p923 - 927.

[46] Jacobsen, V. et al *Interferometric optical detection and tracking of very small gold nanoparticles at a water-glass interface* Opt. Express **2006** *14, 1* p405-414.

[47] Gu, Y. et al *Three-Dimensional Super-Localization and Tracking of Single Gold Nanoparticles in Cells* Anal. Chem. **2012** 84 p4111-4117.

[48] Aaron, J. et al *Dynamic Imaging of Molecular Assemblies in Live Cells Based on Nanoparticle Plasmon Resonance Coupling* Nano Lett. **2009** *9,10.*

[49] Delange, O. *Optical heterodyne detection* Spectrum, IEEE **1968** *5, 10* p77-85.

[50] Hariharan, P. *Basics of Interferometry* Academic Press **2010** p93.

[51] Matsuo, Y. and Sasaki, K. *Time-resolved Laser Scattering Spectroscopy of a Single Metallic Nanoparticle* Jpn. J. Appl. Phys. **2001** *40,1,10* p6143-6147.

[52] Sun, W et al *Wavelength-Dependent Differential Interference Contrast Microscopy: Selectively Imaging Nanoparticle Probes in Live Cells* Anal. Chem. **2009** *81* p9203-9208.

[53] Arbouet, A et al *Direct Measurement of the Single-Metal-CLuster Optical Absorption* Phys. Rev. Lett. **2004** *93* p127401-1-127401-4.

[54] Muskens, O. et al *Optical response of a single noble metal nanoparticle*; J.Opt. A: Pure Appl. Opt. **2006**, *8*, S264-S272.

[55] Gaiduck, A. et al *Room-Temperature Detection of a Single Molecule's Absorption by Photothermal Contrast* Science **2010** *330* p353-356.

[56] Boyer, D. et al *Photothermal Imaging of Nanometer-Sized Metal Particles Among Scatterers* Science **2002** *297* p1160-1163.

[57] Berciad, S. et al *Photothermal Heterodyne Imaging of Individual Nonfluorescent Nanoclusters and Nanocrystals* Phys. Rev. Lett. **2004** *93* p257402-(1-4).

[58] Huang, D. *Optical Coherence Tomography* Massachusetts Institute of Technology PhD Thesis **1993**.

[59] Adler, D. et al *Photothermal Detection of Gold Nanoparticles using Phase-Sensitive Optical Coherence Tomography* Opt. Express **2008** *16,7* p4376-4393.

[60] Jung, Y. et al *Three-Dimensional High-Resolution Imaging of Gold Nanorods Uptake in Sentinel Lymph Nodes* Nano Lett. **2011** *11,7* p2938-2943.

[61] Paranjape, A. et al *Depth Resolved Photothermal OCT Detection of Macrophages in Tissue using Nanorose* Biomed. Opt. Express **2010** *1,1* p2-16.

[62] Zhou, C. et al *Photothermal Optical Coherence Tomography in Ex Vivo Human Breast Tissues Using Gold Nanoshells* Opt. Lett. **2010** *35,5* p700-702.

[63] Li, P.C. et al *In vivo Photoacoustic Molecular Imaging with Simultaneous Multiple Selective Targeting Using Antibody-Conjugated Gold Nanorods* Opt. Express **2008** *16,23* p18605-18615.

[64] Kim, S. et al *In vivo three-dimensional spectroscopic photoacoustic imaging for monitoring nanoparticle delivery* Biomed. Opt. Express **2011** *2,9* p2540-2550.

[65] Boyd, G. et al *Photoinduced luminescence from the noble metals and its enhancement on roughtened surfaces* Phys. Rev. B **1986** *33, 12* p7923-7936.

[66] Hecht, E. and Zajac, A. *Optics* Addison-Wesley Publishing **1974** p502-504.

[67] Lippitz, M et al *Third Harmonic Generation from Single GOld Nanoparticles* Nano Lett. **2005** *5,4* p799-802.

[68] Masia, F et al *Resonant four-wave mixing of gold nanoparticles for three-dimensional cell microscopy* Opt. Lett. **2009** *34, 12* p1816-1818.

[69] Wang, H. et al *In vitro and in vivo two-photon luminescence imaging of single gold nanorods* Proc. Natl. Acad. Sci. **2005** *102, 44* p15752-15756.

[70] Sahoo, Y et al *Aqueous Ferrofluid of Magnetite Nanoparticles: Fluorescence Labeling and Magnetophoretic Control* J. Phys. Chem. B **2005** *109* p3879-3885.

[71] Smith, R et al *Parallel detection of low modulation depth signals: application to picosecond ultrasonics*; Meas. Sci. Technol. **2008**, *19*.

[72] Johnson, N et al *Quad-phase synchronous light detection with 64 X 64 CMOS modulated light camera*; Electron. Lett. **2009**, *45*, p1090-1091.

[73] McFarland, A. and Van Duyne, R. *Single Silver Nanoparticles as Real-Time Optical Sensors with Zeptomole Sensitivity*; Nano Lett. **2003** *3, 8* p1057-1062.

[74] Anker, J et al *Biosensing with plasmonic nanosensors*; Nat. Mater. **2008** *7* p442-453.

[75] Mock, J et al *Shape effects in plasmon resonance of individual colloidal silver nanoparticles*; J. Chem. Phys. **2002** *116* p6756-6759.

[76] Tamaru, H et al *Resonant light scattering from individual Ag nanoparticles and particle pairs*; App. Phys. Lett. **2002** *80* p1826-1828.

[77] Becker, J et al *Gold Nanoparticle Growth Monitored in situ Using a Novel Fast Optical Single-Particle Spectroscopy Method*; Nano Lett. **2007** *7, 6* p1664-1669.

[78] Bingham, J. et al *Localized Surface Plasmon Resonance Imaging: Simultaneous Single Nanoparticle Spectroscopy and Diffusional Dynamics*; J. Phys. Chem. C Lett. **2009** *113* p16839-16842.

[79] Acimovic, S et al *Plasmon Near-Field Coupling in Metal Dimers as a Step toward Single-Molecule Sensing*; ACS Nano **2009** *3, 5* p1231-1237.

[80] Ament, I et al *Single Unlabeled Protein Detection on Individual Plasmonic Nanoparticles*; Nano Lett. **2012** *12* p1092-1095.

[81] Krpetic, Z et al *Inflicting Controlled Nonthermal Damage to Subcellular Structures by Laser-Activated Gold Nanoparticles*; Nano Lett. **2010** *10* p4549-4554.

[82] Zhang, L et al *Single Gold Nanoparticles as Real-Time Optical Probes for the Detection of NADH-dependent Intracellular Metabolic Enzymatic Pathways*; Angew. Chem. **2011** *50* p6789-6792.

[83] Hutter, E et al *Microglial Response to Gold Nanoparticles*; ACS Nano **2010** *4, 5* p2595-2606.

[84] Grabinski, C et al *Effect of Gold Nanorod Surface Chemistry on Cellular Response*; ACS Nano **2011** *5* p2870-2879.

[85] Abb, M et al *All-Optical Control of a Single Plasmonic Nanoantenna-ITO hybrid*; Nano Lett. **2011** 11 p2457-2463.

[86] Wu, G et al *Remotely Triggered Liposome Release by Near-Infrared Light Absorption via Hollow Gold Nanoshells* **2008** *130* p8175-8177.

[87] Schwartsberg, A. et al *Synthesis, Characterization, and Tuneable Optical Properties of Hollow Gold Nanospheres*; J. Phys. Chem. B **2006** *110* p19935-19944.

[88] Brown, L. et al *Heterodimers: Plasmonic Properties of Mismatched Nanoparticle Pairs*; ACS Nano **2010** *4* p819-832.

[89] Lassiter, J.B. et al *Close Encounters between Two Nanoshells*; Nano Lett. **2008** *8* p1212-1218.

[90] Lee, S. et al *Dispersion in the SERS Enhancement with Silver Nanocube Dimers*; ACS Nano **2010** *4* p5763-5772.

[91] Mazzuco, S et al *Ultralocal Modification of Surface Plasmons Properties in Silver Nanocubes*; Nano Lett. **2012** *12* p1288-1294.

[92] Sherry, L et al *Localized Surface Plasmon Resonance Spectrocopy of Single Silver Nanocubes*; Nano Lett. **2005** *5* p2034-2038.

[93] McMahon, J. et al *Correlating the Structure, Optical Spectra and Electrodynamics of Single Silver Nanocubes*; J. Phys. Chem. C **2009** *113* p2731-2735.

[94] Zhang, S. et al *Substrate-Induced Fano Resonances of a Plasmonic Nanocube: A Route to Increased-Sensitivity Localized Surface Plasmon Resonance Sensors Revealed* Nano Lett. **2011** *11* p1657-1663.

[95] Grillet, N. et al *Plasmon Coupling in Silver Nanocube Dimers: Resonance Splitting Induced by Edge Rounding* ACS Nano **2011** *12* p9450-9462.

[96] Chen, H. et al *Observation of the Fano Resonance in Gold Nanorods Supported on High-Dielectric-Constant Substrates* ACS Nano **2011** *5,8* p6754-6763.

[97] Tao, A. et al *Polyhedral Silver Nanocrystals with Distinct Scattering Signatures* Angew. Chem. Int. Ed. **2006** *45* p4597-4601.

[98] Rabin, O. and Lee, S. *SERS Substrates by the Assembly of Silver Nanocubes: High-Throughput and Enhancement Reliability Considerations* Journal of Nanotechnology **2012** *2012* article ID: 870378.

[99] Urban, A. et al *Single-Step Injection of Gold Nanoparticles through Phopholipid Membranes* ACS Nano **2011**, *5, 5* p3585-3590.

[100] Zhao, F. et al *Cellular Uptake, Intracellular Trafficking, and Cytotoxicity of Nanomaterials* Small **2011**, *7* p1322-1337

[101] Zhang, Y et al *Targeted delivery of Tet1 peptide functionalized polymersomes to the rat cochlear nerve* Int. J. Nanomedicine **2012**, *7* p1015-1022.

[102] Jun, Y. et al *Continous imaging of plasmon rulers in live cells reveals early-stage caspase-3 activation at the single-molecule level* Proc. Nat. Acad. Sc. **2009**, *106* p17735-17740.

[103] Huff, T. et al *Controllong the Cellular Uptake of Gold Nanorods* Langmuir **2007**, *23, 4* p1596-1599.

[104] Fairbairn, N. et al *Spatial modulation microscopy for real-time imaging of plasmonic nanoparticles and cells* Opt. Lett. **2012** *37, 15* p3015-3017.

[105] Muskens, O. L. et al *Optical extinction spectrum of a single metal nanoparticle: Quantitative characterization of a particle and of its local environment* Phys. Rev. B **2008** *78* p205410-1 - 205410-9.

[106] Muskens, O. L. et al *Quantitative Absorption Spectrocopy of a Single Gold Nanorod* J. Phys. Chem. **2008** *112* p8917-8921.

[107] Baida, H. et al *Quantitative Determination of the Size Dependence of Surface Plasmon Resonance in Single* $Ag@SiO_2 Nanoparticles Nano.Lett.$ ***20099,*** *10p*3463 − 3469.

[108] Redding, B. et al *Speckle-free laser imaging using random laser illumination*; Nat. Photon. **2012** *6* p355-359.